USDOT Tier 1
University Transportation Center
on Improving Rail Transportation
Infrastructure Sustainability and Durability

Final Report VT-9

DESIGN AND OPERATIONAL ASSESSMENT OF A MOBILE ROBOT FOR UNDERCARRIAGE INSPECTION OF RAILCARS

Mehdi Ahmadian, J. Bernard Jones Chair and Director

and

James M. Kasch, Graduate Research Assistant

Center for Vehicle Systems and Safety
Railway Technologies Laboratory
Virginia Tech
3103 Commerce Street
Blacksburg, VA 24060

September 2024

Grant Number: 69A3551747132

DISCLAIMER

The contents of this report reflect the views of the authors, who are responsible for the facts and the accuracy of the information presented herein. This document is disseminated in the interest of information exchange. The report is funded, partially or entirely, by a grant from the U.S. Department of Transportation's University Transportation Centers Program. However, the U.S. Government assumes no liability for the contents or use thereof.

ABSTRACT

This research assesses the design and track operation of a track crawler robot (TCR) for practical and easy inspection of stationary railcars' undercarriages in an effort to detect any pending failures or assess any security risk of out-of-sight objects. The research leverages against a robot available at the Railway Technologies Laboratory (RTL) of Virginia Tech and offers improvements to the structure, drive system, imaging devices, and operator remote control to improve the speed, track maneuverability, and duty cycle of the robot.

The TCR includes a drive system consisting of two AC motors that operate a track (like tank tracks). It further includes two GoPro® cameras, light system, and onboard power for approximately one hour of maximum power operation. The details of the TCR design are introduced through its operational requirements, which guided its initial design. The specific design configurations are used to derive the applicable parameters essential for track operation of the robot. The TCR's subsystems are evaluated individually to assess their strengths and weaknesses, which are then used to guide the specific tasks in improving the overall system's performance. The details of the required modifications are included for the imaging, lighting, control, frame structure, and mobility subsystems.

For each subsystem, test results are used to engineer workable solutions for overcoming the shortcomings or implementing additional functionality. The redesigned system is further evaluated through testing to assess the improvements due to modifications. Beyond laboratory tests, a final assessment of the system was done on a branch line and mainline track, both with great success.

The recorded images and operational evaluation of the TCR prove it to be a valuable inspection tool for the railroads to inspect out-of-sight undercarriage components of stationary trains in a railyard or siding, to identify any failed or nearly-failed equipment before they develop into a major or out-of-compliance issue. The TCR also promises to be useful for security agencies to easily and efficiently inspect trains entering secured areas to uncover any suspicious devices.

CONTENTS

LIST OF FIGURES

LIST OF TABLES

Chapter 1
Introduction

The $80-billion freight rail industry in the U.S. operates on nearly 140,000 miles of track and supports the U.S. economy by providing more than 167,000 jobs and supplying the most efficient transport of cargo over land [1]. In the 2023 fiscal year, a total of 1,947 train accidents were reported to the Federal Railroad Administration (FRA) in the U.S., of which 1,299 were derailments [2]. These numbers have been reduced substantially from 20 years ago when 2,991 accidents, 2,124 of which were derailments, occurred during the 2003 fiscal year. Innovation has contributed to this downtrend in accidents, and continuing this practice of innovation is crucial for further decreasing the rate of accidents, ensuring that the railroads remain safe, efficient, and competitive in the ever-adapting global market.

The railroads' improved capability to perform condition monitoring on their in-service rolling stock has contributed to the reduction in accidents [3]. Various technological advancements have supplied this improved condition monitoring capability. Wayside train monitoring systems (WTMSs) are detectors deployed trackside that provide condition monitoring data on passing trains; however, the inspection methods employed during stationary inspections remain largely manual with little technological assistance. During these inspections, inspectors are given little time to cover an entire railcar, and many hard-to-see undercarriage components may get overlooked. With stationary inspections required before a train may leave the railyard, the railroads cannot reliably prevent defective equipment from departing, which may cause delays or even a derailment in transit. Additionally, short-line and regional railroads may not have the resources to acquire advanced WTMSs, and a cost-effective inspection solution could greatly increase their condition monitoring capabilities.

The Railway Technologies Laboratory at Virginia Tech (RTL) has been developing a cost-effective, efficient, and mobile device to gather undercarriage inspection data from stationary trains to address this need. The Track Crawler Robot (TCR) is designed to traverse beneath stationary trains as they are parked on revenue service tracks. An imaging system onboard the robot will collect images from the undercarriage, which could be used for either manual or automated defect detection. If implemented correctly, the TCR could maintain the efficiency of stationary inspections while greatly enhancing their effectiveness.

This research focuses on the comprehensive improvements made to the TCR system to equip it for undercarriage inspections. The basic operating procedure of the TCR is to be deployed trackside, climb over the rails into the track bed, turn to align with the direction of the train, traverse beneath the train while gathering clear images of the entire undercarriage, and climb back out of the track bed. At the beginning of this project, the TCR was unable to complete this procedure reliably, and improvements were needed to the imaging, lighting, control, and mobility systems, among others. Each system critical to the completion of this task was assessed, and improvements were made and validated. The results of this research demonstrate that the ability of the TCR to complete undercarriage inspections of entire railcar undercarriages has been greatly improved. The TCR can gather clear images of the entire undercarriage in a single pass. The TCR is simple and easy to control with a single operator. The TCR possesses the mobility to perform each necessary maneuver for unassisted inspection completion. Additionally, the TCR can operate reliably at 2

mph and can cover approximately 2 miles on a single charge at this speed. A few reliability concerns were raised during the completion of rail climbing and turning while trackside, which are recommended for future efforts to fully equip the TCR for unassisted undercarriage inspection. Future studies could use the newly available data to further improve the system, reaching its full potential. The implementation of autonomous control and defect detection are now feasible tasks to undertake in the future and could prepare this technology for success in the market.

To note, portions of this report were taken or modified from a published paper by Kasch and Ahmadian in the open-access journal of Designs [4].

1.1. Motivation

WTMSs are installed trackside and monitor various data signatures of the passing trains, autonomously alerting the railroads of any suspected defects. These systems may monitor the passing trains for the presence of wheel flats, wheel cracks, hot bearings, and low-hanging equipment, among other defects, using advanced sensing systems [3]. Some of these WTMSs now come in the form of advanced vision systems [5]. These systems may image 360° around the railcars or be focused on a specific area, such as the undercarriage. Imaging at a fast rate, the systems can gather clear images spanning the entire area of interest. With the recent advances in computer vision, artificial intelligence (AI), and machine learning (ML), one can employ the mentioned systems to gather a vast amount of video data—often in many terabytes—and use them to autonomously detects defects. Such capabilities are valuable to the railroads as they provide condition monitoring on a much larger scale than is possible by manual methods. It is now possible that a missing component, such as a bolt, could be autonomously detected on a train moving up to 70 mph toward its destination. The railroad's local response team would be notified and equipped to respond quickly, potentially averting a later disaster. The limitations of these systems are their large cost and stationary nature. Estimated at $3 million USD per unit, the cost of a modern 360° inspection portal is out of reach for all but the Class I railroads [6]. Being stationary, the system can efficiently inspect entire trains many times per day as they pass by; however, there is no method for gathering the same quality of data from a train that remains stationary. Realistically, a train may be stopped on a siding with a suspected defect on its undercarriage in an unknown location, and there exists no system to quickly and effectively provide the data necessary to determine the presence and location of a given defect.

As noted, inspection methods for stationary railcars have remained nearly unchanged throughout the past decades. This is likely because it is less economical to manually move a detector alongside a stationary train than to have the train travel past the detector. FRA regulations dictate that each railcar in an assembled train must be inspected before it is cleared to depart the railyard [7]. In these pre-departure inspections, carmen are responsible for inspecting the full length of the train, which at times can be over 2 miles long [8]. To this day, the process remains nearly devoid of any technological assistance. Making this process more difficult, many critical components on a railcar lie on the undercarriage in areas difficult, time-consuming, and hazardous to inspect manually [9]. The time allotted for these inspections was reportedly 3-4 minutes per car as a standard in the past; however, some current reports now state that carmen are given only 60 s. per car (a fact that has come under scrutiny after the widely covered derailment in East Palestine last year) [10]. The railroads run on efficiency, which is clearly the driving force behind the short inspection times;

however, the effectiveness of these inspections should be maximized to ensure the safety of the railways as well as to minimize costs by catching failures early. Realistically, given the current conditions surrounding pre-departure inspections, defects may be overlooked that could have been captured if the carmen had efficient access to information regarding the state of the undercarriage. If a method for gathering WTMS-level inspection data from the undercarriage of stationary railcars was developed, the railroads could be positioned to capture many more undercarriage defects without sacrificing the efficiency of their processes. Furthermore, with the consistent gathering of high-quality undercarriage data, autonomous defect detection models could then be deployed to make full use of the data, alerting the inspectors of areas needing attention beneath the railcar. Inspectors could then focus most of their efforts on the more readily inspected non-undercarriage components. They would only need to manually inspect the undercarriage in areas suspected of containing defects, thus increasing these inspections' effectiveness, efficiency, and safety. The successful implementation of autonomous defect detection during a stationary inspection would fully bring WTMS-level capabilities to this previously manual and difficult task.

1.2. Objectives

This research aims to develop a Track Crawler Robot (TCR) that can move in between railroad tracks and inspect the undercarriage of a stationary train, through gathering high-quality video images that can be viewed in real-time or post-processed to detect damages or discover unintended objects in out-of-sight places. The specific goals are to:

- ensure that all images gathered from the undercarriage maintain adequate clarity and contrast to be usable for defect detection,
- equip the system with image collection span that covers the entire width of a standard railcar undercarriage in a single pass,
- modify the system to be simply and easily controllable by a single operator while maximizing its operating speed,
- enable consistent and reliable maneuvering capability for the unassisted completion of undercarriage inspections while maximizing its reliability, and
- identify and mitigate any unnecessary safety risks inherent to the system.

1.3. Approach

The study relies on engineering analysis, testing, and retesting of the TCR’s maneuverability, imaging, lighting, and power needs to improve its functionality and reliability for its intended use. The research goals were pursued by analyzing the onboard systems in environments closely related to the operating conditions of actual train inspections. The assessments led to the identification of areas needing improvement. Further investigation aided in the deeper understanding of the root cause of a given shortcoming within the TCR. The system in question was then redesigned, modified, and retested to investigate whether the modifications had sufficiently equipped the system for undercarriage inspections.

Depending on the subsystem needing improvement, varying redesign methods were applied. The redesign of mechanical subsystems was first informed by the unique requirements of the subsystem, e.g., a frame member must be relocated to increase the field of view (FOV) of the

imaging system. Secondly, engineering judgment was applied to create and refine concepts. Finally, calculations and simulations were conducted to validate the concepts, including finite element analysis (FEA) and modal analysis. In the case of the lighting system, it was possible to quantify the degree to which the subsystem was inadequate during the initial assessment. This calculation, along with the unique requirements of the system, e.g., the light's beam must be spread across the section of the undercarriage in view, informed the redesign. Lastly, the control system assessment revealed that the present methods were categorically unfit for real-world inspections. These methods include the nature of the control system, and the feedback supplied to the operator. In this case, research was first conducted to inquire how other systems operate in similar conditions, and solutions were pursued based on market-tested methods.

Once the evaluations of each system yielded adequate results, a final round of testing was conducted in the expected operating conditions. The primary portion of the test was an undercarriage inspection of a pair of railcars. A test was also conducted on a portion of revenue service track to evaluate the TCR's ability to maneuver in that environment, as most tests were performed on unmaintained tracks with smaller, which affected the TCR's dynamics. By placing the TCR in its true working environment, the results from each subsystem could confidently be used to evaluate its performance.

1.4. Contributions

The most significant contribution of this research is refining the TCR system to clearly image an entire railcar undercarriage in a single pass. This capability is unique to the TCR. To our best knowledge, no other mobile device can capture the entire undercarriage of a railcar in a single pass while in the railyard and siding environments. This capability was validated while traveling up to speeds of 2 mph and was limited by the TCR's controllability rather than image quality. The study also presents a comprehensive assessment of the TCR's capabilities. The system's control methodology is enhanced by providing the operator with video feedback and integrating a control loop regulating the TCR's speed. The TCR is equipped to consistently perform rail climbing and turning with the rails through the inclusion of an additional undercarriage idler sprocket assembly. The reliability of the TCR is enhanced through the informed redesign of a failure-prone drivetrain subsystem, although concerns remain, which should be addressed in future work. These improvements are all validated through testing, and the results are presented. The results demonstrate a self-propelled railcar undercarriage inspection robot with unique capabilities that have not yet been shown in the literature. This research has brought highly effective, technology-assisted inspections of stationary railcars one step closer to becoming viable in the market.

1.5. Outline

A review of the relevant literature will first be presented. This review will serve to give a detailed background on the relevant topics to the research. The primary topics of the review will be modern train inspections, robotics used for mobile inspections of transportation equipment, and imaging parameters. The first two topics will give a background on the current technology used for inspecting rail equipment and will present a few similar robotic systems that have been developed. The imaging parameters section will provide background information about the operation of cameras, which will be important to understand when discussing image quality later in this paper.

A detailed overview of the TCR's original state will follow. This section will introduce the device and its specific operating requirements, which helped inform its initial design, as well as the testing conducted later in this paper. The parameters of the original TCR will be presented, and their values will be derived when applicable. Lastly, the known design drawbacks and potential areas of interest for redesign and modification will be presented, defining the scope of the work to be completed.

Following this will be a short section detailing the work that Giovanni Mantovani completed before the start of this project. This work was conducted to improve the vibrational response of the imaging system and is included here for completeness.

The process of improving each applicable system will then be presented in separate sections. These sections will follow the pattern of assessing the original design, identifying the existing shortcomings, and detailing the process of redesigning, modifying, and preliminarily validating each improvement.

The final testing and results will be presented following these sections. The testing methods will first be described in terms of each system being investigated. Then, a comprehensive assessment of the TCR's performance during these tests will follow. The effects of the improvements and the system’s current capabilities will be presented. Any remaining drawbacks and comparisons to other relevant systems will also be described.

Lastly, the conclusions of this work will be presented. The work completed will be summarized. The most significant findings of this research will be listed and presented in detail. The final section of this paper will include recommendations for future steps.

Chapter 2
Literature Review and Background

This chapter will provide a detailed overview of the relevant topics to this research. It will present the state of train inspections in the US today, specifically targeting the technological assistance used and its effects. Similar robotic inspection systems used in the transportation industry will be presented. Systems that aim to complete similar tasks to the TCR will be covered in greater detail to define the gap in the literature that the TCR aims to fill. Basic imaging parameters will then be covered, emphasizing the specific parameters most important to the successful performance of the TCR's onboard imaging system.

1.6. Modern Train Inspections

In modern times, trains are inspected by an array of autonomous detectors, each designed to identify a specific set of malfunctions within the train. Most of these detectors are installed next to the rails and inspect the trains as they pass by. Implementing the systems in this way is economical, as the detector may remain stationary while inspecting the entire length of the train. Such systems are referred to as wayside train monitoring systems (WTMSs). WTMSs have been in use since the 1930s and 1940s when hot-box detectors and dragging equipment detectors were first developed; both continue to be widely used today [11–13]. As technology has become more advanced through the years, so have the capabilities of these systems. State-of-the-art WTMSs are now capable of detecting many more types of defects. Studies have now shown methods for utilizing strain gauge, accelerometer, acoustic, and thermal imaging data for the detection of wheel flats [14], wheel-rail impact forces [15,16], unbalanced loads [17], lateral and vertical wheel-rail contact forces [18], and defective bearings [19], among others. The development and implementation of these systems give railroads the information they need to maintain their equipment more efficiently and safely.
Most relevant to this study are the WTMSs that utilize vision systems to monitor the rolling stock and detect defects. Some of these systems use an inspection pit to create thermal and visible-spectrum images of the railcar undercarriage, which are then analyzed offline for potential defects using image processing algorithms [20–22]. However, the inspection pits used by these systems are only typical in maintenance facilities. These systems may be used on railcars that already possess a suspected defect but are not feasible on the revenue service track. Additionally, thermal imaging is most useful on in-motion railcars. A defect may cause heat build-up during operation, and a certain heat signature may be useful to aide in identifying it. This heat build-up is not present when a stationary inspection is conducted, making this specific defect detection method undesirable for the project's needs.

Wayside imaging systems have also been shown to be able to identify and locate critical components on rolling stock, such as wheels, journal bearing bolts, suspension springs, and others, using convolutional neural networks (CNNs) and other image processing models [23,24]. These systems may use the resulting data to identify missing or defective forms of railcar components. To successfully implement such a system, a large dataset of annotated images is required to train and test the CNNs. Although not strictly related to the work conducted in this research, it can be imagined that similar methods could be used to autonomously identify defects if the TCR system is developed to a sufficient extent.

Figure 0-1: A train passes through an advanced inspection portal. Credit: Sofi Gratas/GPB News [6]

Expanding on these technologies, more recently, inspection portals have been installed on Class I revenue service track,
Figure *0-1*. These systems capture images 360° around railcars at speeds up to 70 mph [5,9]. High-speed cameras and lighting systems are used to capture more than 1,000 clear images per rail car. These inspection portals use AI models to process the images for potential defects using the latest technology and report high detection rates of defects with low rates of false positives. Suspected defects are transferred to a team of subject matter experts. This team inspects the images to determine whether a defect exists and if immediate action must be taken in response. These systems help railroads gather advanced condition monitoring data from their rolling stock, and as the AI models inevitably improve, the data gathered by the portals will only become more valuable. However, these inspection portals are limited to in-motion inspections. By definition, a train must be cleared in a stationary inspection before it can pass through and be inspected by one of these systems. Additionally, these portals are out of reach for all but the Class I railroads, with unit costs reportedly nearing $3 million [6]. Other commercial visual inspection WTMSs are designed solely to inspect the railcar undercarriages. One of these systems is designed to compare undercarriage images of railcars to template images in order to detect foreign objects [25]. This system is primarily designed for usage within the security industry, where detecting and identifying foreign objects is of great safety concern. Other systems, however, gather similar data to the above-described inspection portals using systems that solely inspect the railcar undercarriage [26,27]. The system developed by TrackVue is equipped with an array of sensors to detect defects in the undercarriages of in-motion rolling stock. This system includes line-scan cameras as well as laser, acoustic, and thermal sensors. LED lighting is integrated into the system to aid in imaging. Using the gathered data, the system can identify a wide range of defects, including structural defects, missing or broken components, low-hanging components, wheel profile defects, and worn brake pads, among others. The system timestamps the analytics from the system and uses details about the passing train to determine a defect's location. This system shows the capabilities of a dedicated undercarriage inspection device. Although data from a few of its sensors are only feasible on in-motion trains, the imaging data is especially useful for providing railroads with a historical record

of the condition of their rolling stock. Providing such a system on a mobile platform could prove extremely beneficial.

Figure 0-2: Carman straining to inspect beneath a railcar. Image reproduced under fair use [28]

Regarding inspections conducted on stationary trains, not much research has been conducted. The pre-departure inspection of railcars remains a manual process, and viewing the undercarriage is difficult and time-consuming.

Figure *0-2*. A study by Edwards et al. [29] investigates the ability to use machine vision technology to automatically detect defects on safety equipment inspected during pre-departure inspections. The paper primarily discusses the identification of overly deformed ladder rungs on the sides of railcars using machine vision models. Although this capability is useful, ladders remain unobscured and should not present any complications for inspectors. Additionally, the paper states that the final result of the research should be a wayside inspection system, which cannot be used during pre-departure inspections. The device described by this research does not appear to be best suited for aiding carmen in effectively completing pre-departure inspections. Schlake et al. [30] conducted an analysis indicating that the railroad industry could save $35 million annually if WTMS data were used to target inspection efforts during intermediate stationary inspections. This study focused on using en route WTMS data for defect detection to aid in targeting a later stationary inspection. The proposed method is that of computer-search human decision. In this configuration, the automated WTMSs are responsible for identifying potential defect locations. The inspectors will then only inspect these locations using their expertise to make a final decision on the presence and severity of any defects. If implemented effectively, this inspection methodology could save time and increase the number of defects captured. Although highly efficient, there is an inherent risk when removing the human from the search process. WTMSs may overlook certain defects that qualified inspectors would identify, allowing defective equipment to continue without any manual inspection. However, in the case of pre-departure inspections of railcar undercarriages, the inspectors are responsible for both search and decision without having the necessary time or resources to conduct either. A mobile platform gathering advanced condition monitoring data from the railcar undercarriages could target defects that inspectors would not have the time or ability to identify during a pre-departure inspection. Therefore, a computer-search human decision inspection methodology for the undercarriage exclusively during stationary inspections may prove to reduce risk while increasing efficiency.

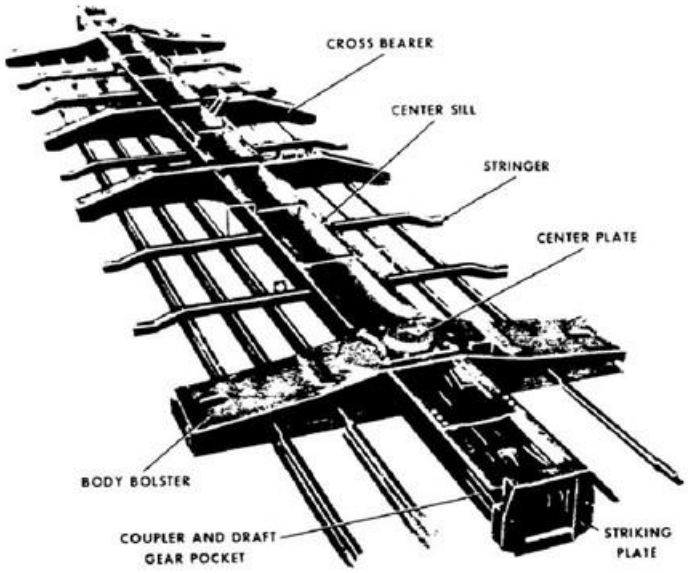

Figure 0-3: Labeled railcar underframe. Image reproduced under fair use [31]

During pre-departure inspections, inspectors are responsible for many undercarriage components. Structurally, they must inspect the center sills, side sills, body bolsters, center plates, and draft gear assemblies,
Figure *0-3*. Together, these undercarriage frame members ensure the railcar's strength and must be inspected to ensure cracks, bends, or buckling defects have not developed. The center sill is the primary structural member of the railcar and lies on its center line. The center sill transmits the buff (compressive) and draft (tensile) forces. Defects within this frame member could cause catastrophic failures, including derailments. As the train travels, slack can occur between railcars. This slack can quickly be taken out, resulting in large draft forces, or railcars can quickly come together, causing large buff forces. To manage these harsh forces, draft gears were developed. These allow the distance between railcars to change and use friction plates to absorb energy throughout their travel. Correctly operating draft assemblies are crucial to the safe operation of trains, as their malfunction may lead to derailments [32].

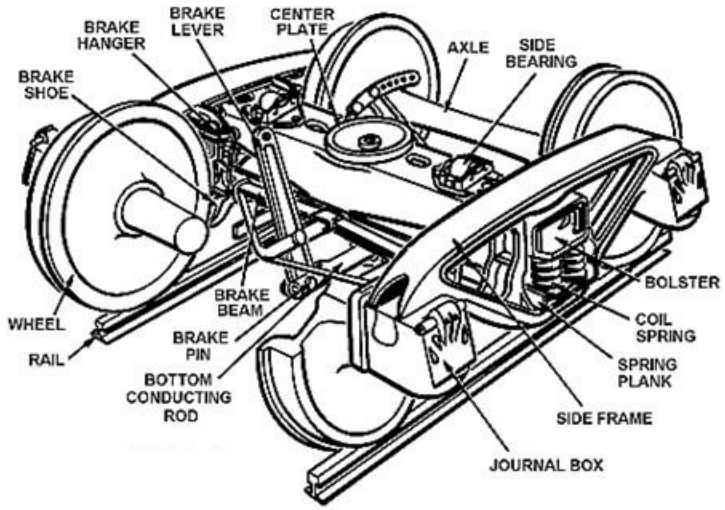

Figure 0-4: Labeled bogie assembly. Public domain [33]

Inspectors are also required to inspect several bogie components, which are partially or fully within the undercarriage. The bogies are sets of four rail wheels that may rotate independently of the railcar's heading. The undercarriage center plates connect the railcars' structure to the bogies. Typically, a railcar is supported by two bogies. The components in need of inspection within this assembly include the side frames, bolsters, wheels, and side bearings, Figure 0-4. Additionally, the brake assemblies remain primarily within the undercarriage in hard-to-see areas. With all the crucial components located beneath the undercarriage that require inspection, it is easily understandable that areas may get overlooked simply due to time constraints. Simply inspecting the length of the center sill for defects would most likely require more time than allotted for the entire inspection, given the difficulties of placing oneself in a position to view it. Defects within many of these components could prove to become catastrophic if allowed to depart from the railyard, and the railroads currently cannot effectively ensure their identification.

1.7. Robotics Used for Train Equipment Inspection

Mobile inspection platforms have been developed and are used within the transportation industry. Some of these devices are used for the inspection of road vehicles. Schoenherr and Smuda [34] detail an undercarriage robot for the inspection of incoming vehicles at a military base. The device is designed to detect suspicious materials while keeping the operator out of harm's way. The device operates autonomously using a 3D laser rangefinder to construct a model of the undercarriage. It compares this model to a template of the vehicle's make and model before traversing to areas where the scans differ and providing inspectors with video footage of these locations. Commercial products, such as the HADES inspection robots developed by Techmatics NZ, provide similar capabilities, autonomously traversing beneath vehicles while providing operators with live imagery data from video, line scan, or thermal imaging cameras [35]. The latter device shows the effectivity of computer-search human decision in a commercial product.

Mobile inspection platforms have been developed and are used today in the railway industry. Many of these mobile platforms are designed to inspect the railways while in motion. Railway inspection robots can monitor rail and track health and identify missing components [36]. Today, railway inspection robots are proven systems and are commercially available [37,38]. Most of these robots traverse on the rails, eliminating the possibility of modifying these platforms for any form of rolling stock inspection. Daniyan et al. [39] detail the design and simulation of a rail inspection robot that traverses using a set of tracks; however, the construction and testing of the robot have not been actualized to the knowledge of the authors. Although market-proven technologies, railway inspection robots will not provide aid in developing a mobile railcar undercarriage inspection device.

Figure 0-5: The ANYmal conducting an inspection on the side of a railcar. Image reproduced under fair use [40]

A few mobile train inspection robots currently exist or are in development. The ANYmal, an autonomous quadruped robot, has been used in partnership with Stadler Rail for the inspection of stationary rolling stock at service locations. Figure 0-5 [40]. The ANYmal platform was not designed for this explicit purpose; however, it is a versatile platform that can be used in a wide variety of operating conditions. The ANYmal can traverse beside the train, gathering data from the side of the car and wheelsets. It can also inspect the undercarriage of the train using a recessed inspection pit or inspect the inside of the cabin using its unique mobility capabilities; however, this system does not currently appear to be able to traverse beneath rolling stock in revenue service conditions due to a lack of clearance.

Kiselev and Korkina [41] present the design of a tracked mobile robot to inspect the sides of railcars in a maintenance facility using various sensors, including video cameras, ultrasonic sensors, and eddy current detectors. This design is limited to the maintenance facility environment and does not appear able to inspect the undercarriage. Additionally, to the knowledge of the authors, the design's construction has not been actualized.

A few studies explore the possibilities of using autonomous robots for undercarriage inspection [42,43]. Imaging and 3D point cloud data are gathered from these robots for defect detection. However, nearly all these systems are only functional in the inspection pit environment, eliminating them from consideration for use in railyards and sidings. Being used within the inspection pit environment is helpful to autonomously detect defects; however, railcars will only arrive at these facilities if a defect is already known or for regular maintenance. Additionally, equipping a mobile platform to transition from the inspection pit to revenue service track is not straightforward. Most devices are too tall to operate beneath a train on the tracks and would need fundamental design changes to attain the necessary clearance. Additionally, the mobility and reliability requirements are much more strenuous when operating beneath a train in the track bed. Traveling over the ballast and ties can cause large forces, and pre-departure inspections must be conducted as efficiently as possible, demanding high speeds, which these devices are not equipped for.

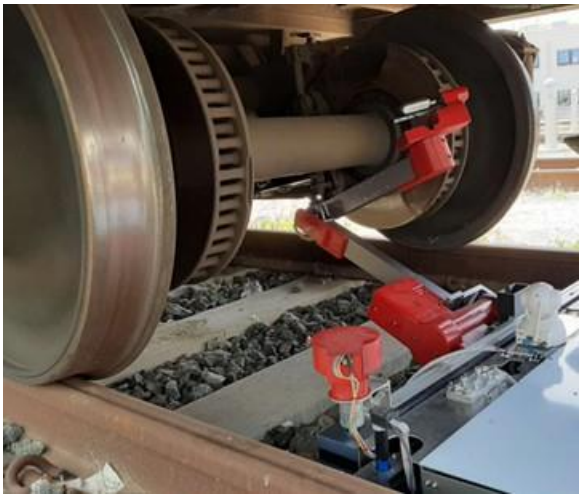

Figure 0-6: The robot developed by Chiaradia et al. [44] inspecting an undercarriage on revenue service tracks. Image reproduced under fair use

Chiaradia et al. [44] present the development of an undercarriage inspection robot that traverses using wheels that run on the rail web and foot, Figure 0-6. The study based in Italy shows the robot can be installed between the rails of revenue service track and can travel beneath rolling stock without interference. An operator remotely controls an articulated arm carrying a depth camera to investigate specific components during the inspection. This system, however, cannot capture the entire undercarriage in a single pass and currently requires manual control of the arm to reach each component of interest, which may become time-consuming and monotonous for the operator. This method of inspection is best suited for closely inspecting certain areas of interest. The articulated arm is capable of imaging many different angles around a given component, which could be especially helpful when investigating a suspected defect. However, a more efficient method is required for a pre-departure inspection where the entire train must be covered. As it uses the rail web for a running surface, it can also not be used in tracks where rail joints are present. Lastly, its need to be manually installed between the tracks requires time that the carmen could use towards the inspection.

Lastly, a commercial robot developed in Serbia is designed to inspect the undercarriages of railcars. The ATUVIS robot [45] is a low-profile robotic platform that traverses the track bed using a set of 4 wheels. A singular camera is mounted to an assembly that can move it perpendicularly to the direction of motion. This device allows detailed imaging of the railcar from rail to rail; however, it cannot image the entire undercarriage at once. Like the robot developed by Chiaradia et al. [44], this device may be better suited for the inspection of areas suspected of having defects due to its current inability to inspect the entire undercarriage continuously. The device uses cognitive positioning, machine recognition, and artificial intelligence to autonomously conduct inspections. It appears that ATUVIS is controlled autonomously; however, it is unclear whether the camera's motion and detection of defects are also conducted autonomously. ATUVIS would need to be manually placed within the rails before beginning the inspection, as it is unable to climb into and out of the track bed.

Although advanced mobile inspection systems have been developed for inspecting railcar undercarriages, the two most comparable systems do not meet the efficiency requirements of a whole-train inspection. Both the robot developed by Chiaradia et al. [44] and ATUVIS would require installation between the rails. Additionally, neither device is capable of continuously inspecting the entire undercarriage in a single pass. Rather, both devices are well suited for inspecting areas of interest, not conducting efficient full-length train undercarriage inspections. The resulting gap in the literature is where this study aims to focus.

1.8. Imaging Parameters

A key prerequisite for the successful completion of this project is the ability to gather high-quality images of railcar undercarriages that may be used for defect detection efforts. High-quality images are those that gather all reasonably available information from a given scene. In contrast, low-quality images are those that fail to gather information from a scene, most likely due to inadequate image contrast or clarity. Additionally, as the imaging data for this project is taken in video form, stability and frame rate become factors for proper data collection. If any of these factors are unsatisfactory, information will be lost that could otherwise be utilized. This section will define these factors and explore the conditions that affect them.

Contrast is the measure of intensity variation across an image. When contrast is high, objects will be clearly delineated from one another and easily identifiable. When contrast is low, edges become difficult to detect, and objects may appear to run together. Low contrast leads to information loss as intensity data is compressed into a narrow band of pixel values. Proper contrast is fundamental to object detection via manual or automated methods. An image's contrast depends heavily on its exposure. Exposure refers to the amount of light captured as the image is taken. Adjustments to exposure represent an actual or apparent increase or decrease in the amount of light incident to the sensor. A properly exposed image will capture details across the image, including in the dimmest and brightest regions. An over-exposed image will allow too much light into the sensor, causing pixel intensity saturation in the brighter areas of the image. Information from those areas is lost and cannot be recovered in post-processing. An under-exposed image will do the same for the dimmer areas of the image. Therefore, although the exposure appears to only alter the brightness of an image, it has a distinct impact on its contrast. At times, proper exposure is not possible, given a camera's dynamic range and the scene's lighting conditions. A camera's dynamic range is the

maximum intensity difference that can be captured in a single image before saturation occurs [46]. Therefore, if a scene's lighting naturally exceeds the camera's dynamic range, proper exposure becomes impossible. Saturation will either occur at the bottom (pure black) or top (pure white) of the sensor's range, and information will not be recorded from those regions. In this case, the exposure must be set such that the maximum amount of useful information is gathered.

A pixel intensity histogram is a helpful tool for investigating image exposure quality. An image, when converted to grayscale, can be defined as an array of pixels with varying intensities from 0 (black) to N (white), with N being the maximum value registered by the sensor (255 for 8-bit). Plotting the histogram of pixel intensities then creates a visual and statistical representation of the brightness and contrast, revealing potential issues. The mean value from the histogram represents the overall brightness of the image, and the standard deviation represents the contrast. A large spike close to 0 or N reveals the presence of clipping in the data. This spike represents a portion of the image defined only by a single intensity value. The contrast in this region is zero, indicating that any information in this region is lost. Clipping is a clear sign of over or under-exposure in the image.

A high global contrast does not always mean a large amount of information gathered. Figure 0-7 shows an image with its corresponding pixel intensity histogram to illustrate this point. The histogram demonstrates that the image's global contrast is high. However, this high contrast is due to the presence of two low-contrast regions located at opposite ends of the sensor's range. After inspection of the image and its histogram, both regions clearly exhibit signs of clipping, and the detail within the foreground and background regions is lacking. It is important to understand that the histogram statistically defines the image, as a whole. Simply observing an image's histogram is not sufficient for making decisive claims about the quality of an image's contrast and will only supplement the holistic analysis of the image quality.

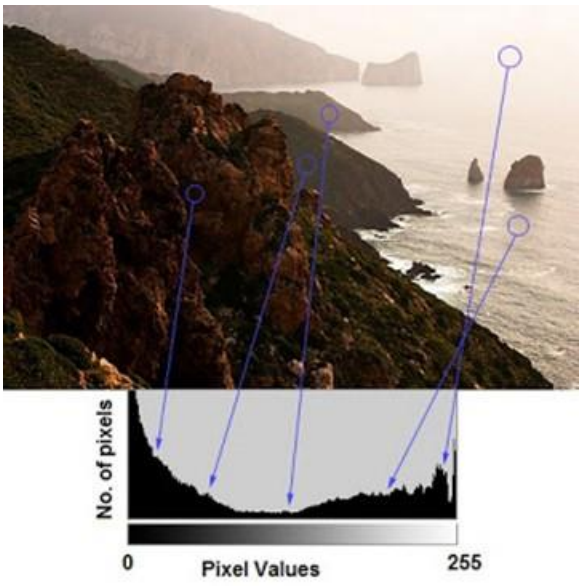

Figure 0-7: An image with its corresponding pixel intensity histogram showing high global contrast with low local contrast. Image reproduced under fair use [47]

Parameters that affect exposure include the light level of the scene being imaged and the "exposure triangle" of camera parameters, which consists of aperture, shutter speed, and ISO. Aperture refers to the lens opening regulating the amount of light allowed into the image sensor [48]. In most traditional lenses, the aperture acts like the iris in an eye and can expand or contract to alter the amount of light allowed through the lens. This action has the added effect of altering the depth of field. A large aperture will create a thinner depth of field where the foreground and background will be out of focus. A small aperture has the opposite effect, creating a thicker depth of field. However, the GoPros® used for this project utilize a fisheye lens with a fixed aperture. This lens was chosen for its wide field of view and excellent depth of field, which is beneficial for action recording [49]. Any objects beyond a certain distance from the lens (approximately 1 ft.) will be in focus. Depth of field is then eliminated as a clarity concern in most cases. However, the fixed aperture does not allow for adjustment, leaving shutter speed and ISO as the two adjustable camera parameters for setting exposure. An additional function of the GoPro® is its ability to digitally alter the field of view. The fisheye lens provides a very wide field of view but distorts the image near the edge of the frame. The SuperView digital lens utilizes this entire sensor. However, the Linear digital lens reduces the field of view to allow for digital correction of the distortion. For this project, the Linear digital lens was primarily used so that objects will take on the same shape no matter their location within the frame, which could aid in defect detection.

Shutter speed defines the amount of time that the image sensor is exposed during the capturing of an image [50]. As the shutter speed slows, the sensor is exposed to the scene for a greater length of time, and more light is allowed, increasing the image's exposure. Shutter speed also greatly influences the clarity of moving objects within the image. Any motion occurring during the exposure of the image sensor will be captured as motion blur. Therefore, a high shutter speed is usually required to clearly image moving objects. Lastly, ISO can be used to alter the exposure of images. ISO refers to the standardized sensitivity of image sensors and is named for the International Organization for Standardization, which created the standard [51]. A higher ISO setting will result in a more sensitive image sensor and a more exposed image. Higher ISO settings can be used to compensate for low-lighting conditions when the aperture and shutter speed cannot be altered. However, increasing the sensitivity also increases the propensity of noise within the image, degrading its clarity. The GoPro® is capable of ISOs from 100 – 6400. Lastly, image resolution will affect the clarity of the image directly. For this project, the resolution was maintained at 1080p to balance image clarity and file size, but the GoPro® does allow for resolutions up to 4K if it is deemed necessary.

Recording in video format requires adequate frame rate and stability. As the inspections should be performed at a constant speed, the frame rate essentially serves to define the spatial resolution of the data. The faster the frame rate is, the smaller the spatial gap will be between images. Additionally, the frame rate serves to define the range of shutter speeds available. The minimum shutter speed allowable is equivalent to the frame rate, and the GoPro® limits the maximum shutter speed to 16 times the frame rate, up to 1/3840 sec. for 240 fps. Lastly, video stability should be maintained. Excessive jolts between frames could create difficulty when attempting to track objects manually or automatically. Two video stabilization functions exist for the GoPro®, and they could be utilized if vibrations from the track bed cause excessive motion between frames. These functions work by only using a portion of the image sensor for a single frame and

automatically rotating and translating which portion of the sensor is used to damp out sudden movements.

Chapter 3
Track Crawler Robot Design and Operational Requirement

This chapter introduces the specific operational requirements of the Track Crawler Robot (TCR) and highlight the unique challenges that arise from its intended purpose. The specific design parameters of the TCR are then presented in detail. Finally, the known drawbacks of the system and additional areas needing further investigation are introduced.

1.9. Operational Requirements and Resulting Challenges

The operating conditions required by this project introduce several key challenges. The TCR should be capable of conducting unassisted inspections of entire railcar undercarriages. Therefore, once deployed, the TCR should require no intervention besides control inputs from a single operator to complete the inspection. Images gathered from the inspection should capture all pertinent data and be fit for manual or automated defect detection. As noted, the railroads desire the pre-departure inspections to be conducted in as little time as possible while remaining effective. Therefore, the speed of the TCR should be maximized. A major factor limiting the maximum speed of inspections is the track bed. The track bed defines the space between the rails and is where the TCR will traverse beneath the train to conduct its inspection. The track bed comprises wooden ties and ballast, creating a varying and rough surface to traverse, Figure 0-1a. These conditions will introduce substantial disturbances into the system during operation. These disturbances could knock the TCR off course and deliver significant shock loading into components, limiting the TCR's maximum controllable and reliable speed. Additionally, substantial vibrations could result, which will likely heighten the effect of motion blur at a given operating speed. High shutter speed imaging can reduce the effects of motion blur, as detailed in the Imaging Parameters section; however, reducing the time of exposure to combat blur will proportionally reduce the amount of light incident to the image sensor for a given frame. To attain an image with adequate exposure under these conditions, significantly more light is needed than when using standard imaging parameters. Simply using shutter speed to attain better image quality could introduce lighting concerns that would need to be addressed.

(a)

(b)

Figure 0-1: (a) The TCR operating on the track bed beneath a railcar; (b) A hopper railcar illustrating the low height of the gates above the track bed.

To capture the full railcar undercarriage in the gathered images, a wide field of view (FOV) is required. Success in this aspect is defined by the capability to image the lowest expected component across the width between the rails. Components are expected to be as low as 16 in. above the track bed in the case of hopper railcar gates, Figure 0-1b [52,53]. In addition, the standard U.S. rail gauge width is 56.5 in. This distance spans the area between the rails, which is most difficult for inspectors to view, and contains many critical components. To ensure the system can capture all possible component locations from at least one point of view, it should be capable of imaging components at the minimum height of 16 in. across the entire gauge width. This required FOV is very wide, spanning over 140° laterally from the existing camera mounting location, 6 in. above the track bed. Wide-angle lenses tend to induce image distortion at the edges of their frames. This effect will cause identical objects to be captured as distinct shapes simply due to their location within the frame. This effect could be detrimental to defect detection efforts as the consistency of the imaging should be maximized. Defect detection models may struggle to identify a distorted object; therefore, it is desired to achieve this FOV requirement with minimal image distortion.

Control within the track bed is another operational concern. As noted, the TCR will be subject to disturbances as it is operating. Disturbances could make constant speed operation difficult as the power needed to maintain a constant speed may change quickly and significantly. Often, the ballast will settle at a level lower than the level of a tie. This creates an edge that a traversing vehicle will run into as it transitions from the ballast to the tie. Disturbances, such as collisions with these edges, could cause the TCR to be jolted off-course, requiring timely steering inputs to correct. At the same time, the TCR will pass partially or fully out of view when it traverses beneath the bogies or other low-lying components. The TCR can only be viewed from the side while beneath the rolling stock. This viewing angle can make determining the TCR's heading and position within the rails difficult. To steer and avoid collisions effectively, the operator needs constant and clear feedback. Line-of-sight feedback for the operator may not be adequate for these purposes.

Lastly, the track bed environment poses mobility and reliability challenges to the TCR. The TCR is rigidly supported by idler sprockets and has no suspension; therefore, the rough environment of the track bed could impose significant shock loads into the frame and damage components. The reliability of the system in these conditions should be assessed. Additionally, maneuvers such as rail climbing and turning while in the track bed are necessary for unassisted operation. Rail climbing requires sufficient undercarriage clearance of the TCR, ample torque from the drivetrain, and sufficient traction from the track bed conditions. Slippage of the ballast under this high-torque maneuver could cause the TCR to become unable to climb out of the track bed. This would require the carmen to take the time to extract the TCR manually, which would reduce the efficiency of the inspection. The TCR utilizes tracks for locomotion. Turning with tracks is conducted via skid steer. Skid steer occurs when the tracks travel at differing speeds, causing the vehicle to turn, and requires portions of the tracks to slide perpendicularly to their plane of rotation. Tracks generate high tractive forces, causing them to slide and requiring a significant amount of force. This principle makes steering within the track bed also susceptible to challenges from insufficient torque or traction. Ideally, the system will be capable of neutral or pivot steer. Neutral steer occurs when the

tracks travel in opposite directions at equal speeds. Neutral steer causes the vehicle to turn in place, allowing it to have a turning radius of zero. Pivot steer occurs when one track is stationary, and the other track generates the force for the turn, pivoting around the stationary track. Either of these turning configurations could allow consistent and quick maneuverability within the rails, but both are difficult to attain for the reasons previously mentioned. If sufficient torque is available for these maneuvers, traction could be a limiting factor. The loose ballast between the ties could be dislodged during high-torque maneuvers. Slippage could cause drastic loss of traction making steering difficult or impossible.

1.10. Design Rationale

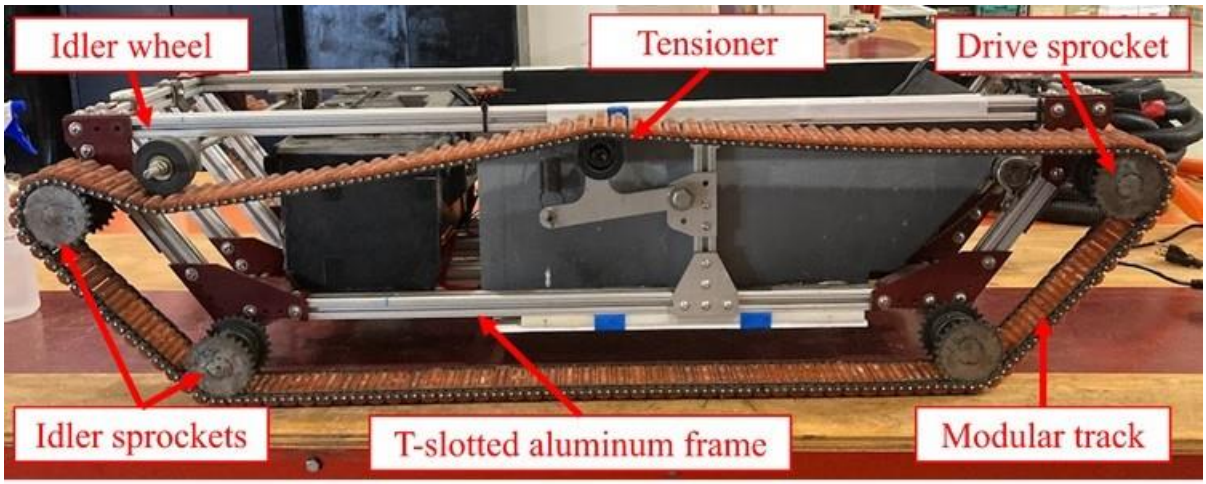

Figure 0-2: Original design of the TCR, side view

The TCR,

Figure *0-2*, was originally designed to fulfill several key specifications necessary for success. Its height was limited to 13 in. to ensure clearance beneath all standard freight railcars. As noted, the lowest components are expected at a height of 16 in., leaving a 3 in. clearance. This clearance can help prevent collisions in the case where the TCR is jolted slightly upwards when rolling over the edge of a tie or if components are placed slightly lower than expected. Its width was designed to be within 30 in. to allow ample clearance between the standard U.S. rail gauge width of 56.5 in. The length of the TCR was similarly constrained to be within 48 in. to allow clearance for operating perpendicular to the rail direction, such as when climbing in and out of the track bed and when turning. A continuous track system was chosen for locomotion due to its simplicity, durability, and excellent traction. The TCR's weight was limited to 100 lbs. to allow for deployment by a team of two, typical for pre-departure inspections. Material costs for the original design were limited to $3000 USD, placing this technology in the price range of both Class I and short-line customers. The specific design details that resulted from these technological limitations are presented in the following chapter.

1.11. Initial Design

Molzon and Ahmadian initially presented the TCR in a conference paper [56]. This paper may be reviewed to gain an in-depth understanding of the original TCR. The primary subsystems of the TCR are the frame, drivetrain, control, electrics, lighting, and imaging.

Figure *0-3* shows the major components of these subsystems and their relationships with one another. Table 0-1 lists the key parameters of the original TCR for reference. Applicable parameters will be derived and calculated later in this section.

Table 0-1: Parameters of the existing Track Crawler Robot design

Motor torque (each)	25 in-lb
Max. motor current (each)	80 A
Gear ratio	3.939
Axle material	1566 steel
Axle diameter	0.625 in.
Motor chain size	ANSI #25
Track chain size	ANSI #35
Battery pack	6S2P LiFePO4
Battery nominal voltage	19.2 V
Battery capacity	16 Ah
Battery max. continuous discharge	240 A
Main circuit breaker rating	100 A
Lighting system	4x 450 lumen (lm) light bars: 1,800 lm total
Lighting power bank	12 V, 6000 mAh lithium
Imaging system	2x GoPro® Hero8 Black

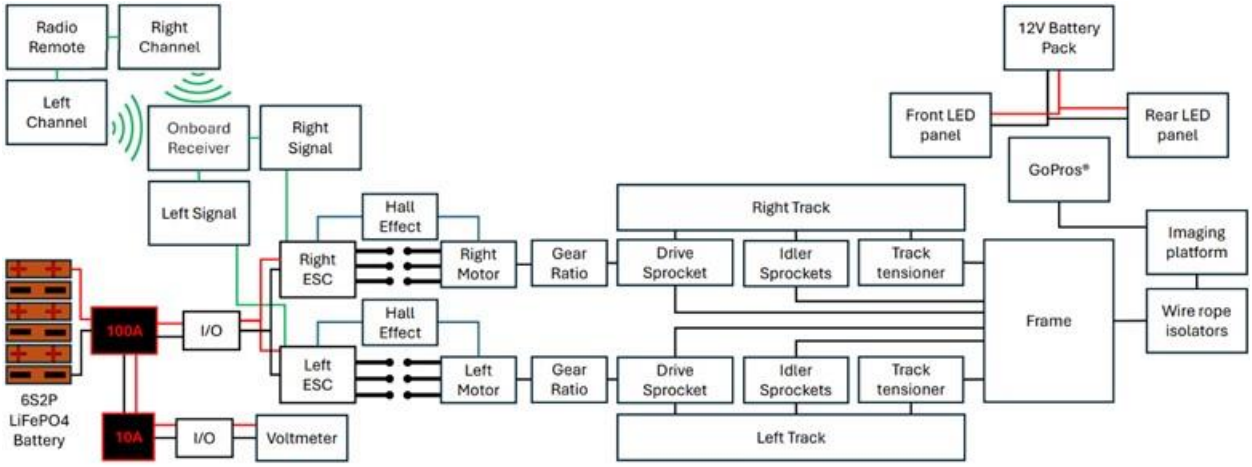

Figure 0-3: Box diagram showing the major components of the TCR and their relations

The TCR is a continuous track robot with a frame constructed of 1 in. x 1 in. aluminum extrusion. This material was chosen for its strength, lightweight, and modular nature, allowing for simple installation and relocation of components. Specialty nuts and bolts clamp onto t-slots located on

each side of the extrusion for the mounting of brackets and various components. Table 0-2 presents the overall dimensions of the TCR and the dimensions of the frame. The overall dimensions meet or exceed the requirements put forward in the previous section, thereby ensuring the TCR can pass under low-lying components and operate between the rails. The frame assumes a trapezoidal shape from the side, as seen in
Figure *0-2*. Two rectangles of frame members oriented horizontally form the top and bottom levels of the trapezoid. Frame members descend at a 55° angle to connect the two levels. The individual frame members are joined together using steel and aluminum brackets. The track system is mounted to the exterior of the frame, and the remaining subsystems are stored in the enclosed space created by the frame.

Table 0-2: Primary dimensions of the TCR

	Length (in.)	Width (in.)	Height (in.)
Overall Dimensions	48	$22\,^{1}/_{4}$	$12\,^{1}/_{2}$
Frame Dimensions	$46\,^{5}/_{8}$	$14\,^{3}/_{4}$	$9\,^{3}/_{4}$

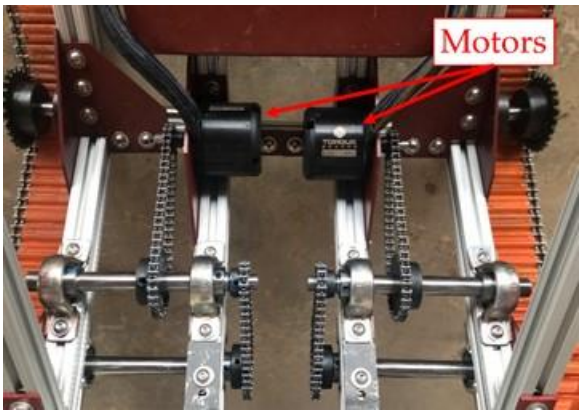

Figure 0-4: The motor and drivetrain components mounted at the rear of the TCR's frame

Two electric skateboard motors drive the TCR (

Figure *0-4***)**. 6355 190KV motors were chosen. 6355 references the motor's diameter of 63 mm and its length of 55 mm. The KV value defines the motor's maximum speed in rpm per volt applied. These motors rotate at 190 rpm per volt when there is no load. Each motor's torque is 25 in-lb and has a maximum continuous current of 80 A. The manufacturer supplied these values [54]. The motors provide power to their respective drive axles at the TCR's left and right upper rear corners through a set of ANSI #25 chains and sprockets. The motor sprocket has 11 teeth and

drives a 26-tooth sprocket. An intermediate axle connects this sprocket with a 15-tooth sprocket, which drives a 25-tooth sprocket on the drive axle,

Figure *0-4*. Gear ratio is the reduction in rotational speed between the driving and driven sprockets [55]. This ratio is also equivalent to the increase in torque at the driven sprocket. Equation (3-1) derives the gear ratio.

$$Gear\ Ratio = \frac{Driven}{Driving} = \frac{26}{11} * \frac{25}{15} = 3.939 \tag{3-1}$$

Using this value, the maximum torque available at the drive axle can be calculated as

$$T_{driven} = T_{motor} * Gear\ Ratio = 25\ in\text{-}lb * 3.939 = 98.5\ in\text{-}lb \tag{3-2}$$

The maximum working load of ANSI #25 chain is 140 lbs. [56]. The maximum tensile load within the system can be calculated using the torque at the drive sprocket and the radius at which the force is acting. The pitch diameter is the most effective measurement for this value and is 1.995 in. for the drive sprocket [57].

$$F_{max} = \frac{T}{D/2} = \frac{98.5\ in\text{-}lb}{(1.995\ in)/2} = 98.7\ lb \tag{3-3}$$

Equation (3-3) calculates the maximum force on the ANSI #25 chain to be 98.7 lb, less than the maximum working load. At the output of each drive axle, a pair of 25-tooth ANSI #35 sprockets drive a 3 in. wide modular, chain-driven track with a rubberlike surface molded between two chain links. The sprockets have a pitch diameter of 2.992 in. [57]. The maximum force within these chains can be found similarly to Equation (3-3); however, the force value is halved to account for the presence of two sprockets at each axle. Equation (3-4) shows that the maximum force on each chain of the track will be 32.9 lb, much less than its workload of 480 lb [56]

$$F_{max} = (\frac{T}{D/2})/2 = \frac{T}{D} = \frac{98.5\ in\text{-}lb}{2.992\ in} = 32.9\ lb \tag{3-4}$$

Therefore, both the ANSI #25 and #35 systems are adequate for the operating conditions of the TCR.

The drive sprockets are located at the rear upper corners of the robot. The remaining sprocket assemblies are idlers,
Figure *0-2*. These assemblies consist of two sprockets welded to an axle for engagement with the chain links of the tracks. The axle is then supported by two ball bearings in thin-walled steel housings bolted to the frame rails, such as the drive axles shown in

Figure *0-4*, thereby supporting the tracks while allowing them to spin freely. The lower idler sprocket assemblies serve as the primary points of contact between the TCR and the ground. An idler roller and tensioner are installed along the upper portion of the track to regulate track tension, Figure *0-2*.

The battery is comprised of LiFePO4 cells in a 6-in-series, 2-in-parallel (6S2P) configuration. Each cell is 3.2 V and has a capacity of 8 Ah. Additionally, each cell is rated for 120 A of continuous discharge. The manufacturer provided these specifications [58]. In a battery pack, the total voltage is the voltage of a cell multiplied by the number of cells in series. The capacity and maximum current of the pack are the respective parameters for the cells multiplied by the number of cells in parallel.

$$V_{pack} = V_{cell} * \#series = 3.2\ V * 6 = 19.2\ V \quad (3\text{-}5)$$

$$C_{pack} = C_{cell} * \#parallel = 8\ Ah * 2 = 16\ Ah \quad (3\text{-}6)$$

$$I_{max,pack} = I_{max,cell} * \#parallel = 120\ A * 2 = 240\ A \quad (3\text{-}7)$$

Equations (3-[5-7]) show that the battery pack supplies 19.2 V with a capacity of 16 Ah and a maximum continuous current of 240 A. A 100 A circuit breaker was included in the system to prevent short circuits. The circuit breaker was placed such that all current from the battery must pass through it, Figure *0-3*.

Based on the battery's nominal voltage and the previously defined parameters, the TCR's maximum speed can be calculated as 8.2 mph, Eq. (3-8), much higher than currently possible for track bed operations. Equation (3-8) estimates the maximum motor speed using the battery pack voltage and the motor's KV value and then converts that speed to the TCR's land speed using the gear ratio and drive sprocket pitch diameter.

$$V_{max} = 19.2\ V * 190\frac{RPM}{V} * \frac{1}{3.939} * \frac{\pi 2.992\ in}{rev} * \frac{1\ mi}{63360\ in} * \frac{60\ min}{hr} = 8.2\ mph \quad (3\text{-}8)$$

The motors are controlled using a 6-channel radio remote. Distinct control signals are necessary for maneuvers like turning when the tracks must turn at separate speeds; therefore, the left and right control signals are transmitted independently on two channels. The throttle can be controlled manually using the vertical position of the remote's joystick. Alternatively, a constant value can be set and applied using a switch on the remote. The throttle signal is duplicated and transmitted on both channels. The steering signal is manually controlled using the side-to-side position of the joystick. The steering signal (positive when to the right) is added to the left control signal and subtracted from the right. This operation creates a steering signal that remains centered around the desired throttle value. The control signals are received by a compatible receiver onboard the TCR. The receiver contains six 3-pin output ports to conduct the signal from each channel. 3-pin connectors are used to transport this signal from the receiver to the 3-pin input ports on the

respective electronic speed controllers (ESCs). Two ESCs independently control their respective motors,

Figure *0-3*. The ESCs receive the control signal and regulate the voltage applied to each motor accordingly. The ESCs supply power to the motors through a set of 3 bullet connectors. The ESCs regulate the motor current by utilizing a feedback loop. Hall effect sensors feed rotational speed data back from the motors to the ESCs, which could be used for feedback control of the motor speed. The ESCs operate using the open-source VESC Project software that allows for customization of control parameters, such as maximum continuous current, control method, and throttle curve shaping. Originally, the ESCs were configured to translate the control signal directly to a motor current; therefore, the operator was responsible for altering the control signal to maintain a constant speed. Since the ESCs regulate the voltage applied to the motors, an internal feedback loop was being used to maintain a desired motor current. The ESCs are rated for a 50 A continuous current and a 240 A instantaneous current [59].

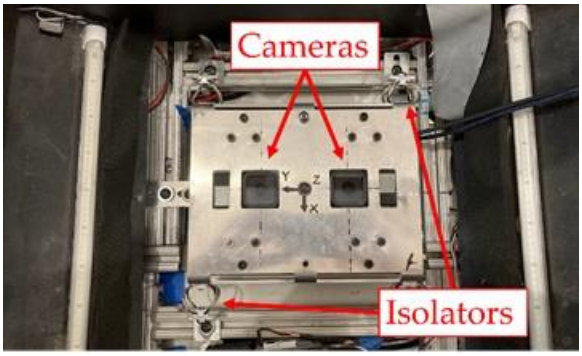

Figure 0-5: The imaging platform with two vertically mounted cameras supported by wire rope isolators. Two of the four light strips are in view on either side of the platform.

GoPro® Hero8 Blacks are used for image acquisition. Two are mounted vertically to a platform supported at each corner by a wire rope isolator to damp out vibrations from the frame to minimize motion blur, Figure 0-5. These isolators were added in the interim between the published paper and the start of this project. A description of their installation and effects has been included in the following chapter to complete this document. A separate power bank powers 4 light strips mounted forward and rear of the imaging platform, Figure 0-5. Each LED bar is rated at 450 lumens (lm), leading to a total initial brightness of 1,800 lm. Two LEDs are mounted forward of the imaging platform, and two are mounted to the rear. The power bank operates at 12 V, has a 6000 mAh capacity, and is rated for 3 A. The light bars were tested in a system with a power meter, which found that 25 W were needed to power the system.

$$I = \frac{P}{V} = \frac{25\ W}{12\ V} = 2.08\ A \tag{3-9}$$

Equation (3-9) shows that the lighting system draws around 2 A, which is within the power bank's working range.

The electrical components were stored in a latching box modified to fit between the TCR's frame rails, Figure 0-6. This box stored the battery and provided the plug to connect it to the entire system. The 100 A circuit breaker governing the entire circuit was placed directly downstream of the battery. The box also stored an anti-spark switch which was used for powering the ESCS on and off using a button mounted to the top of the box. A switch mounted to the side was wired to power a voltmeter on the top of the box, which could be used to monitor the battery's life. A 10 A circuit breaker was placed in series with this voltmeter. Lastly, the power bank used for the LED system was mounted into the box using velcro straps. Wiring from the output of the anti-spark switch and the LED power bank was routed out of ports on the sides of the box to the ESCs and LED bars.

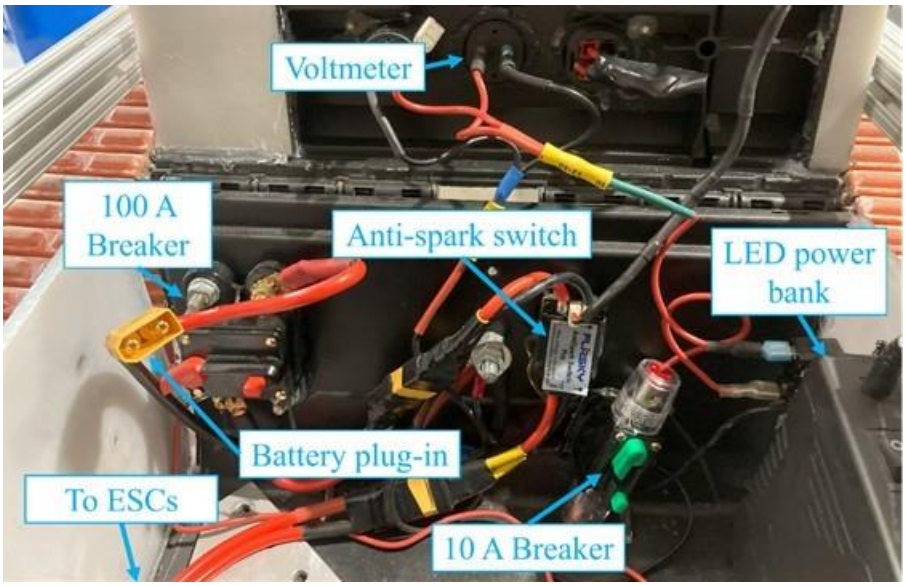

Figure 0-6: Original state of the electrical box

1.12. Known Design Drawbacks and Points of Interest

Several design drawbacks were initially uncovered in the paper by Molzon and Ahmadian [60]. Other areas need investigation to determine if their performance is adequate given the unique operational challenges. Each of these areas will be the subject of an intensive assessment to determine current capabilities and shortcomings. Redesign and modification of each system will be performed, and testing and validation will be presented to present the final capabilities of each system and highlight any remaining shortcomings. Molzon and Ahmadian discovered that at speeds greater than 1.6 mph, motion blur begins to obscure the contents of the images. The TCR will most likely need to operate above this speed to maximize the efficiency of the inspection as required by the railroads, which will only increase the presence of blur. Additionally, the tests in the paper were performed on asphalt. Asphalt is a relatively smooth surface and will most likely not introduce vibrations into the system on the order experienced during track bed operations. Vibrations in the system will exaggerate the relative motion between the cameras and the imaging target, increasing the presence of motion blur. The paper also detailed the system's reliance on

natural light. The system was without any supplemental lighting system at the time. Without an appropriate lighting system, the TCR will only have sufficient lighting to conduct inspections during the day, if at all, making it dependent on ambient conditions when a robust solution is required. As detailed earlier, a lighting system was installed before the beginning of this project; however, it needed to be investigated. In addition to these known drawbacks, other systems needed to be assessed and redesigned to meet the requirements of this project. These include the FOV, control system, mobility, reliability, and overall safety of the device. Additionally, previous work was completed to minimize the vibrations transmitted into the cameras during operation which will be covered as well. The following chapters will cover each of the above-mentioned systems in depth.

Chapter 4
Vibration Reductions to Improve Image Quality

This chapter provides the efforts dedicated to improving the image quality of the onboard video system through reducing vibrations at the camera mounting location. In earlier efforts, the vibrations causing camera shakes had been identified as one of the main contributors to diminishing the quality of the video images. The poor video quality appears as blurred images that can be used effectively by an inspector or an automated image processing system to definitively highlight a defect. As we will be discussed next, significant research was performed to improve image quality by reducing vibrations at the cameras.

1.13. Dampers for the Vibrational Isolation of the Imaging Platform

Giovanni Mantovani conducted improvements to the TCR's imaging system platform to reduce camera shakes during operation. The improvements were completed after the publication of the first paper about the TCR and before the start of this project. This work and its results are included here for the completeness of the document.

It was previously hypothesized that the vibrations within the TCR were a large contributor to the motion blur observed in the previously published results. Vibrations possess the potential to cause motion at rates much higher than the operating speed of the TCR. If the amplitude of this motion was large enough to be visually noticeable, motion blur may result in the captured imagery. It was, therefore, desired to improve the vibratory response of the TCR's imaging system. Initially, the cameras were rigidly mounted to the frame of the TCR. Any vibrations excited within the frame of the TCR could be directly transmitted to the cameras. Improving the vibrational dynamics of the entire TCR while operating within the track bed is a large undertaking; however, the dynamics between the imaging system and the TCR may be simply improved. A system for damping the high-frequency vibrations within the TCR from being transmitted into the imaging system could be implemented by mounting the imaging system using dampers.

Wire-rope isolators were chosen as the interface between the chassis and the imaging system. Wire-rope isolators act as both springs and dampers with a nonlinear stiffness. When oriented in the "roll" configuration, as installed on the TCR, the isolators increase in stiffness as the deflection increases. An aluminum plate was cut using a water jet and then bent to serve as the imaging platform. Two vertically oriented GoPros® were mounted to the imaging platform using 3D-printed mounts. 4 wire-rope isolators were used to mount the imaging platform to the TCR, one at each corner. The imaging system was now isolated from the chassis to some degree; however, the effectiveness of the system required investigation.

1.14. Test Bed Construction

The testing of the vibrational system and others later in the project would require operating the TCR in the track bed environment or one similar. Due to the logistical challenges of coordinating track time with a railroad operator and transporting the TCR for testing, it was determined that constructing an approximate replica of the track bed, referred to as the "Test Bed," would be desirable for performing these tests and optimizing the TCR for real-world inspections. An in-

house replica of a track bed would allow for rapid, iterative testing to take place before final validation could be conducted at an actual set of tracks. The Test Bed was constructed out of two independent sections, each built on a foundation of a ¾-in. thick, 44-in. x 96-in. sheet of plywood. Two wooden planks, 2-in. x 12-in., were affixed vertically along the long outside edges of the plywood sheets. 2-in. x 4-in. planks spanned the shorter outside edges of the plywood sheets, and others spanned laterally at two equally spaced locations along the length. 2-in. x 7-in. planks, stacked two-high and bolted onto the intermediate planks, simulated the ties. Gravel filled the resulting enclosure to approximately 1 in. below the top of the ties, approximating the ballast and leaving a typical gap between the two as seen on the tracks, which can induce significant shocks and vibrations into the TCR. Aligning the resulting sections created one 16-foot-long track. Lastly, two ramps were constructed using ¾-in. plywood with composite board mounted at the leading edges to create a smooth transition from the ground, allowing the TCR to reach testing speeds before reaching the Test Bed. The completed Test Bed, Figure 0-1, provided a controlled environment for evaluating the TCR's performance under simulated track bed conditions, allowing efficient assessment and optimization of its design and operation. The resulting width of the Test Bed was 41 in. which is considerably less than the gauge width of 56.5 in., presenting a more difficult control scenario than will be experienced during a real-world inspection.

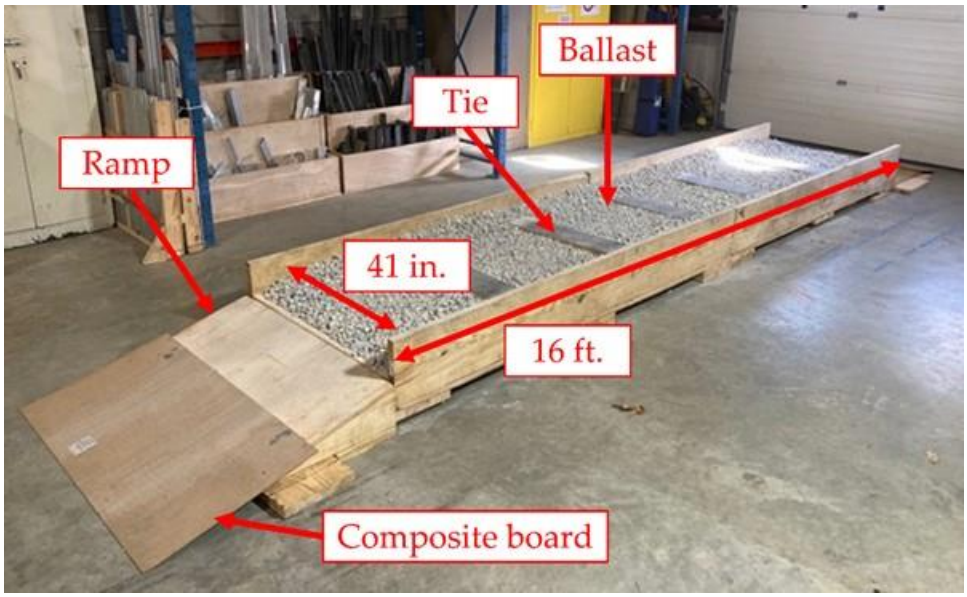

Figure 0-1: Finalized Test Bed with dimensions and components labeled.

1.15. Vibrational Testing and Results

A test was conducted to evaluate the effects of the vibrationally isolated imaging platform. The test aimed to measure the vibrations experienced by the frame and the imaging platform while traversing the Test Bed to assess the effectivity of the vibrational isolators. The test was conducted at 4.25 mph to assess the system at a speed higher than would be expected during an onsite inspection. It was thought at the time that 3 mph would be the maximum operating speed of the TCR. The process of deciding the maximum operating speed of the TCR is discussed in detail in later chapters. To gather acceleration data, two accelerometers were mounted to the TCR. One was

mounted to the frame beneath the imaging platform, and the other was mounted to the center of the imaging platform. The chosen accelerometers had a sensitivity of 135 mV/G. Vibrational data was gathered using a Dewesoft DEWE-43A [61]. 6 of the 8 channels were used to record the XYZ acceleration data from the chassis and imaging platform-mounted accelerometers. A 1 kHz simultaneous sampling rate was used for all data recording. The DEWE-43A is designed with an integrated anti-aliasing filter. The TCR was aligned with the Test Bed and placed with a short run-up before the test began. A step input commanding a 4.25 mph speed was then applied. The operator visually monitored the course of the TCR throughout the test and applied steering inputs as needed to avoid contact with the sides of the Test Bed.

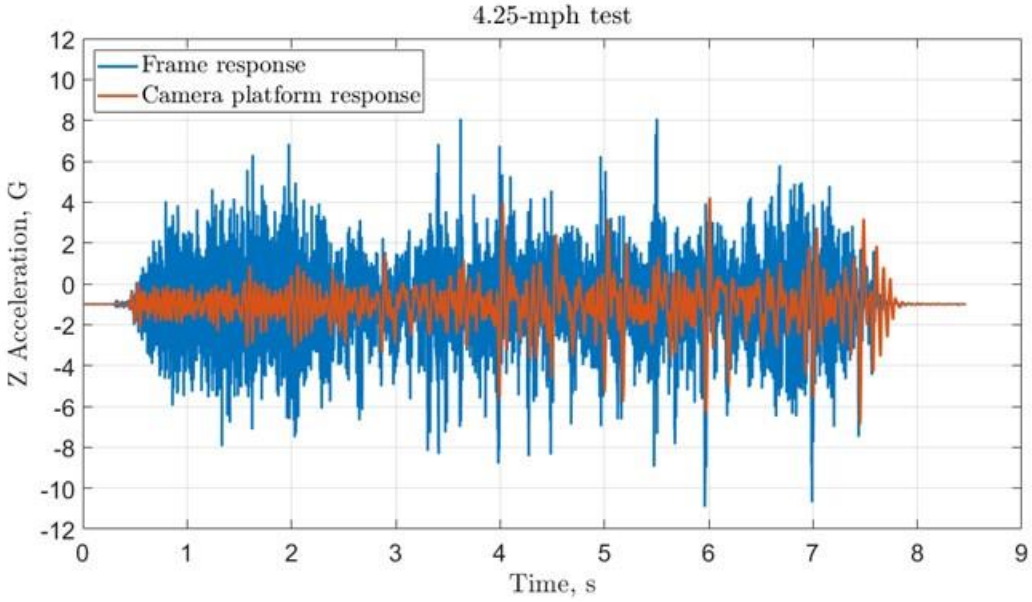

Figure 0-2: Acceleration in the z-direction throughout the vibrational test at 4.25 mph

The time-domain data from the vibrational test at 4.25 mph, Figure 0-2, demonstrates that the frame and camera platform undergo distinct vibrations during TCR's movement, particularly on rough surfaces. Many large spikes in acceleration occur within the frame that are not transmitted or transmitted with a reduced amplitude to the camera platform. This behavior is advantageous as a sudden shock in motion to the imaging system creates motion blur.

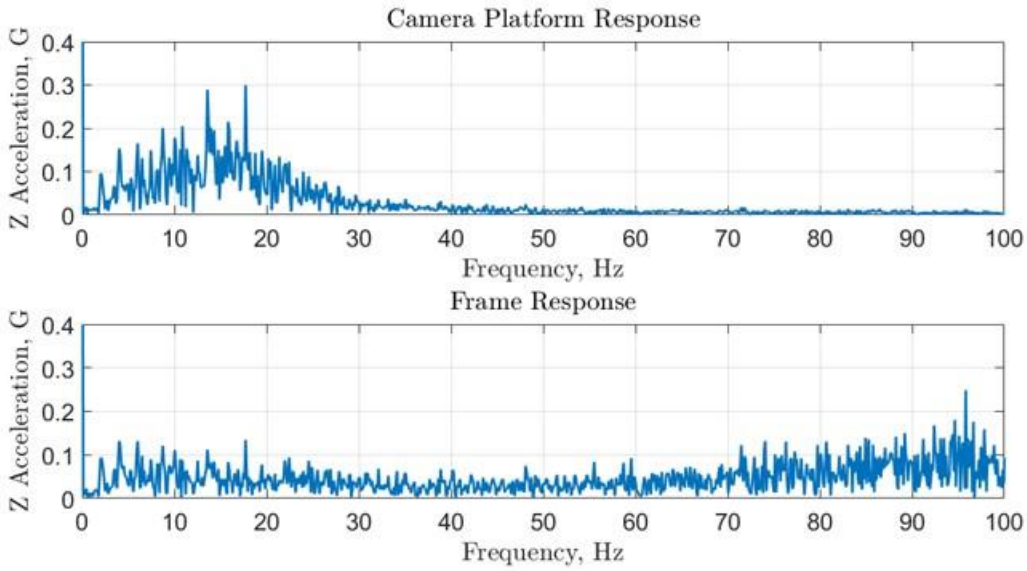

Figure 0-3: Frequency domain acceleration in the z-direction during the 4.25 mph vibrational test

When viewing the z-direction acceleration in the frequency domain,

Figure *0-3*, the effect of the isolators is clear. The camera platform exhibits a range where the vibrations from the frame are amplified. This range occurs between approximately 5-25 Hz. After this range, however, the system effectively damps out the vibrations from the frame. The data clearly shows that high-frequency vibrations are not transmitted into the system, which the time-domain data supports. Large spikes are seen in the frame vibrational data which are not transmitted into the cameras. The inclusion of the vibrational isolators alone did not remove the presence of motion blur in the images, as will be discussed in the following chapter. The system mainly serves to damp out the imaging system's vibrations at higher frequencies. The damping comes at the expense of low-frequency amplification; however, this behavior did not impede the system's ability to capture clear images, as will be shown in the following chapter.

Chapter 5
Imaging System Adjustments

The imaging system's ability to gather clear images of the railcar undercarriages is a key element of success for the project. Factors such as eliminating vibration transmission to the cameras that was discussed in the last chapter and managing the camera settings that will be discussed in this chapter are essential the image quality. Of equal importance is lighting, which will be discussed in the next chapter. It is known vibrations, slow shutter speed, and inadequate lighting can lead to poor images that compromise the ability to conduct undercarriage inspections. This chapter will mainly concentrate on how to best adjust the camera settings to maximize their image quality and overall performance.

1.16. Assessment of the Initial Design

TCR tests prior to the start of this research had indicated that at speeds greater than 1.6 mph over asphalt, the images become blurred. In this study, a series of tests were conducted to investigate the conditions that cause motion blur. The tests consisted of operating the TCR at constant speeds beneath a poster approximately 2 ft. above the ground and evaluating the images for any blur or dark spots. The poster was placed relatively low to the ground to maximize the relative motion between the poster and the camera during imaging, which would increase any blurring and light distortion effects. The testing parameters are shown in Table 0-1. The shutter speed was set to the Auto setting for these tests. This setting allowed the camera to alter the shutter speed throughout the test to maintain an acceptable level of exposure in each frame.

Table 0-1: Testing parameters for initial imaging tests beneath a poster

Speeds (mph)	Test surface	Resolution	Frame rate (fps)	Shutter speed	ISO range	Poster height (in.)
1.6	Concrete	1080p	120	Auto	100-1600	23.75

The test results are shown in

Figure *0-1*. As a note, the lighting system was not powered for this test, so no conclusions can be drawn from the image's lighting. The slowest test at 1.6 mph is shown. Even at this speed, the poster is significantly obscured by blur. These results suggest that the imaging system's rejection of motion blur will need to be significantly improved. Speeds greater than 1.6 mph are desired for undercarriage inspections to maximize efficiency, and much higher vibrations are expected in the rough track bed environment, which will only increase the relative motion between the imaging target and the camera lens, increasing blur.

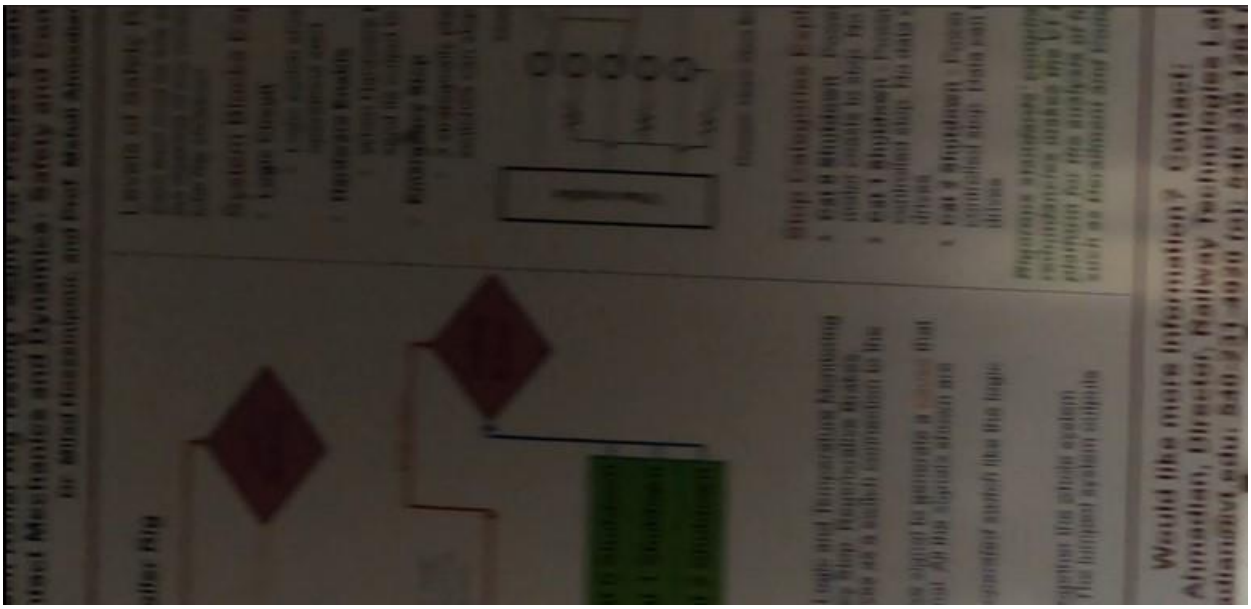

Figure 0-1: Poster test results at 1.6 mph using the Auto shutter speed

The imaging system's ability to maintain proper exposure when interfering light conditions exist was evaluated. Interfering light refers to high-intensity regions of an image not relevant to the area of interest. This effect can occur when portions of the sky or the sun are visible in an image of the undercarriage. Even if artificially lit, the undercarriage will be significantly dimmer than directly sunlit regions. If these regions are sufficiently bright, the camera will reduce the ISO to maintain a balanced exposure. However, due to the camera's dynamic range, this adjustment could cause dimmer regions to be captured with insufficient contrast for defect detection. To test the legitimacy of this concern, a test was conducted to compare the imaging system’s ability to capture the undercarriage of a tractor-trailer when completely beneath the tractor-trailer and when partially exposed to a clear daytime sky. Imaging parameters for this test are shown in Table 0-2.

Table 0-2: Light interference testing parameters

Resolution	Frame rate (fps)	Shutter speed (sec.)	ISO range	Target height (in.)	Lighting conditions
1080p	120	1/1920	100-1600	48	Clear sky, daytime, indirect sunlight

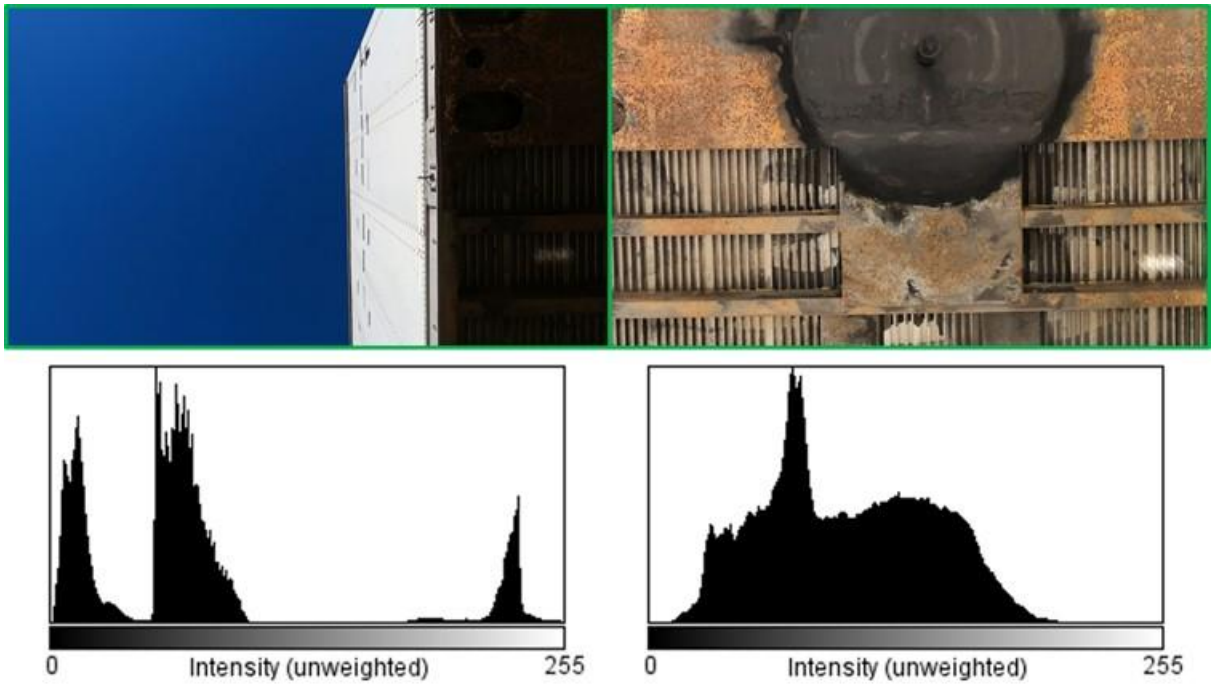

(a) **(b)**

Figure 0-2: Light interference test results with pixel intensity histograms: (a) Partially exposed to the sky; (b) Completely beneath the trailer

The light interference test results, shown in Figure 0-2, show that bright light sources from regions unimportant to the overall imagery can reduce the quality of pertinent regions. The partially exposed image, Figure 0-2a, is well exposed to capture the sky and side of the trailer, but the undercarriage is underexposed. Its histogram is divided into 3 distinct groupings. The brightest grouping represents the white side of the trailer; the middle region represents the sky, which is not as bright but distinctly brighter than the undercarriage. The undercarriage is defined by the dimmest grouping. In general, the image has excellent contrast and avoids clipping; however, for the purposes of this project, the information gained is poor. Ideally, the undercarriage should be exposed similarly to the fully covered image, Figure 0-2b, which, from its histogram, exhibits far superior contrast. In this case, unimportant regions such as the sky and trailer would be overexposed and may exhibit clipping; however, this could be done without reducing the quality of the image for defect detection. Methods should be investigated to ensure proper exposure of the area of interest despite bright interferences.

Lastly, an assessment was conducted to evaluate the stability of the video during operation in track bed conditions. Even if each frame is captured clearly, if the video itself has significant jolts and rotations throughout, object tracking from frame to frame may become difficult, whether manual or automated. To investigate, tests were conducted on the Test Bed while imaging a piece of rectangular aluminum tubing stretching parallel to the direction of motion at a constant height. Tests were conducted at 1, 2, and 3 mph. An image of a known-sized grid was taken at the height of the aluminum tubing, to define the scale for the motion of the tubing within the image. The effective translation and rotation of the image could then be computed based on the change in the

location of the tubing within the frame. The location of the tubing was found by gathering the pixel location of its 4 corners. The y-coordinate of each corner was gathered where it intersected with the edge of the frame. The two left values and two right values were averaged to compute the y-location of the tubing at the left and right edges of the frame in pixels. The centroid was found by averaging these two values. The rotation was then found using Equation (5-1).

$$\theta = arctan\left(\frac{y_L - y_R}{1920\ px}\right) \tag{5-1}$$

This equation uses the difference in height between the two sides and the known width of the frame as 1920 pixels to calculate the angle of the tubing and, therefore, the effective angle of the image. To note, the height is measured from the top of the frame; therefore, subtracting the right height from the left leads to a positive angle in the counterclockwise direction. The centroid location and rotation of the tubing were computed every 6 in. of the test. The distance was estimated using the commanded speed throughout the test and the time elapsed during the video. Speed was commanded using the feedback control system, which will be presented in a later chapter. The average values for both displacement and rotation were found and subtracted from each to create a zero-mean representation of the image's motion rotationally and laterally throughout the test.

From the 3-mph video stability test,

Figure *0-3*, it could be seen that the image moved laterally over a range of about 2 in. Additionally, the image rotated up to 5° in either direction during the test. Neither of these metrics appears to show severe video instability; however, methods could be pursued, such as utilizing the built-in video stabilization functions to mitigate these effects and improve defect detection capabilities.

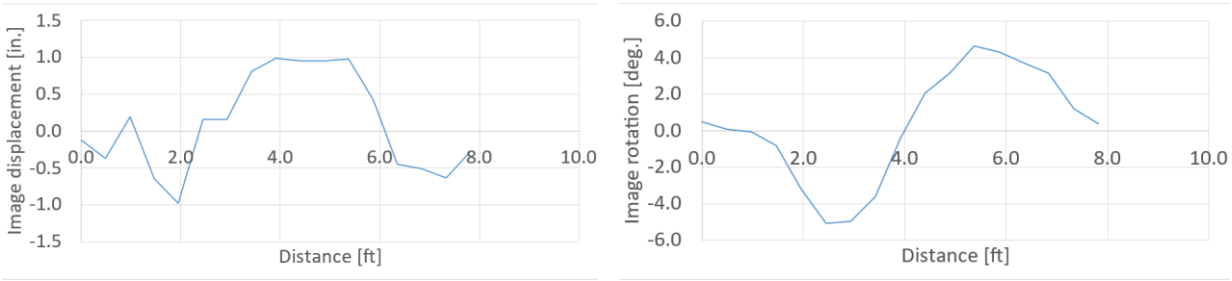

(a) **(b)**

Figure 0-3: Video stability control test 3 mph: (a) Effective image displacement; (b) Effective image rotation

The imaging assessment determined that reducing motion blur was critical to the project's success. Additionally, making the imaging system robust against interfering light and reducing the random motion of the video during testing were tasks that could further improve its effectiveness.

1.17. Reduction in Motion Blur using Shutter Speed

As mentioned in the background section on imaging parameters, shutter speed greatly affects the presence of motion blur. Higher shutter speeds result in an image that captures a shorter period,

thereby reducing the distance objects travel during exposure and, by extension, reducing motion blur. To investigate this effect, tests were conducted with the two quickest shutter speeds available at 120 fps, 1/960 sec. and 1/1920 sec., Table 0-3. These tests were conducted at a higher speed than the previous tests with the Auto shutter speed and on asphalt, which introduced more vibrations into the system than the smooth concrete. A realistic track bed speed for the TCR could be 3 mph; therefore, these tests were conducted at 6.5 mph, over double that hypothetical speed, to approximate the inclusion of increased vibrations due to the track bed environment. Additionally, the tests conducted in the previous paper were conducted over asphalt at a maximum speed of 6.5 mph; therefore, these results would also be an effective comparison to those.

Table 0-3: Testing parameters for high shutter speed poster tests

Speeds (mph)	Test surface	Resolution	Frame rate (fps)	Shutter speed (sec.)	ISO range	Poster height (in.)
6.5	Asphalt	1080p	120	1/960 & 1/1920	100-1600	23.75

The test results,

Figure *0-4*, show that high shutter speeds effectively reduce motion blur. In particular, the 1/1920 sec. test demonstrates excellent clarity, while small amounts of blur are still visible in the 1/960 sec. test. The lighting system was powered for both tests, and a distinct reduction in brightness can be viewed in the 1/920 sec. test. This is expected since the quicker shutter speed allows less light to reach the sensor. Based on these results, a shutter speed of 1/1920 sec. was used for future testing, which, as mentioned, particularly affects the lighting requirements of the system. A 1/1920 sec. shutter speed presents the most difficult lighting conditions that have been tested while also maximizing the rejection of motion blur. Equipping the system to image successfully in these conditions would maximize the chance of success in real-world inspections. If possible, the shutter speed could still be decreased if motion blur remains at an acceptable level, and the light available for each image would increase, improving image quality.

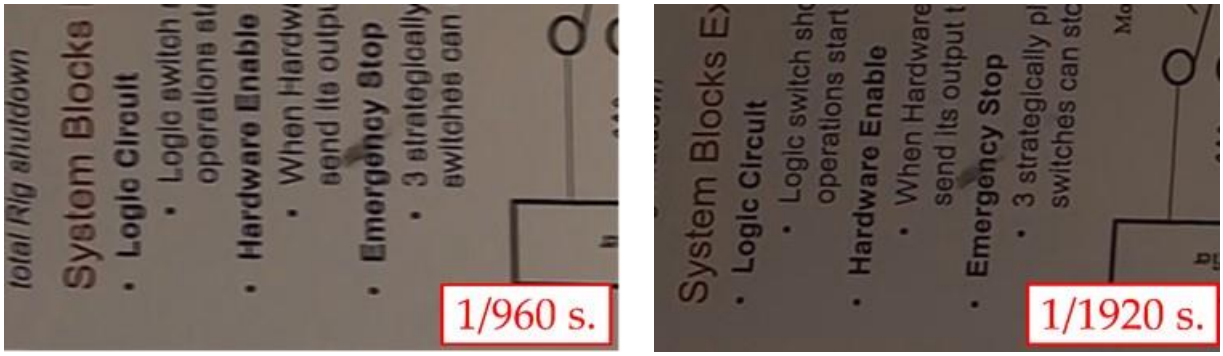

Figure 0-4: Imaging assessment results at 6.5 mph with the shutter speeds displayed

1.18. Ambient Light Interference Rejection using ISO

As shown in the initial assessment, bright regions unimportant to defect detection may cause the camera to adjust its sensitivity to the detriment of the areas requiring inspection. The camera can adjust its sensitivity within a range that the user may define. Therefore, it was desired to test whether defining a certain minimum sensitivity would allow the camera to sufficiently image an undercarriage while rejecting brighter light sources. To answer this hypothesis, a series of tests were conducted. The TCR was driven at a constant speed from out in the open to beneath a tractor-trailer while imaging using the onboard cameras. The first test was conducted with the full ISO range of 100-6400 selected, and a modified test was conducted where the ISO was limited to 1600-6400. This modification ensured that the camera was always imaging with at least an ISO 1600 sensitivity. The tests were conducted on a clear bright day where the sky was much brighter than the trailer's undercarriage. Once under the trailer for a sufficient length of time, the imaging will reach a steady state where the cameras have fully adjusted to the lighting change. These images will be investigated for overall image quality. They will also be compared to images gathered just as the TCR begins to pass beneath the trailer. This transient period will show how the imaging system handles imaging the undercarriage when the much brighter sky is directly in frame. These tests were conducted using an improved lighting system that will be detailed in a later chapter.

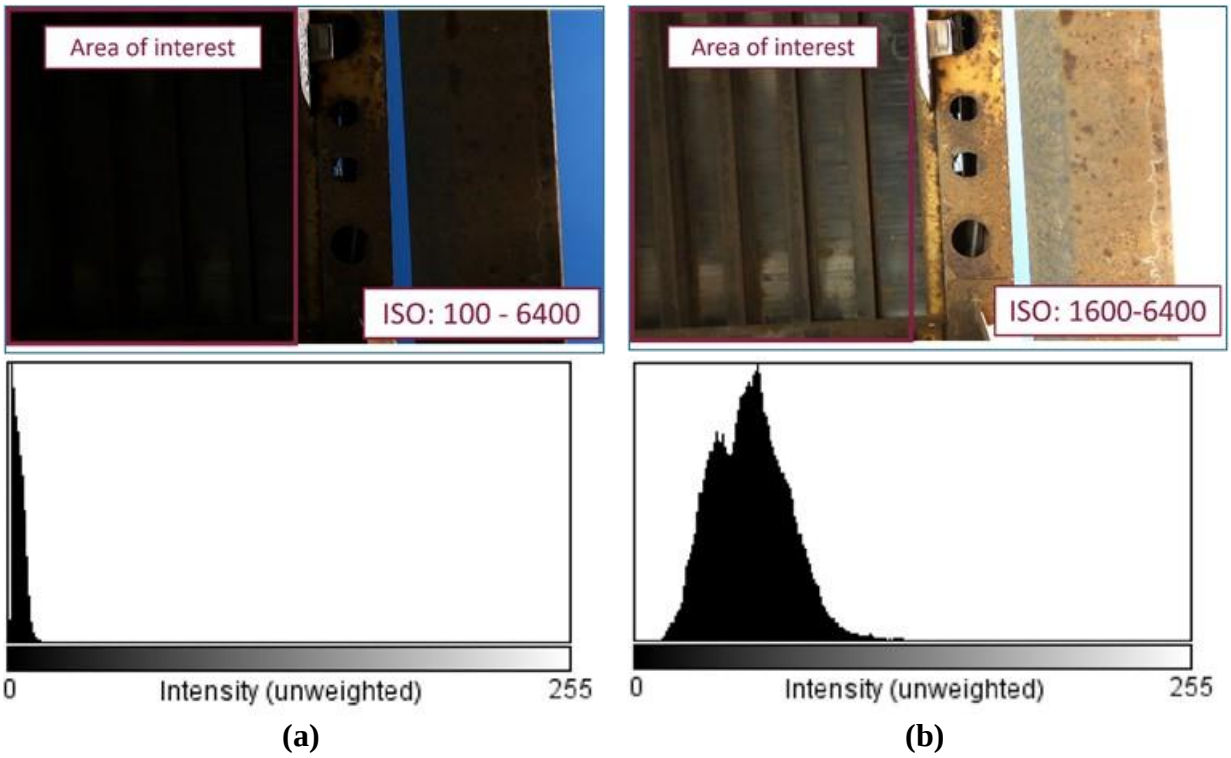

Figure 0-5: Comparison of transient images where undercarriage and sky are both visible: (a) Full ISO range test with pixel intensity histogram; (b) 1600 – 6400 ISO test with pixel intensity histogram

From the test results, Figure 0-5, it can be clearly seen that increasing the minimum sensitivity of the system allows for the rejection of ambient light interference. As a result, the camera is unable to lower its sensitivity past a certain threshold, and the undercarriage remains well-lit throughout the transient portion of the test. Pixel intensity histograms were gathered from the outlined areas

of interest. These histograms clearly show the effects of this change. The full ISO test exhibits nearly absolute clipping on the lower end of the sensor's range. Nearly no information is discernable from this image. Conversely, the reduced range image has eliminated clipping and occupies a much wider range of the sensor. Specifically, the reduced ISO range increased the standard deviation by over 6.5 times. The increase in contrast to the area of interest comes at the cost of saturation at the upper end of the sensor. The sky is completely saturated in the reduced ISO range test; however, this region is unimportant to defect detection, and the loss of information here is inconsequential.

If the minimum sensitivity is raised too high, the undercarriage images will become overexposed as the camera is held to a very high sensitivity.

Figure *0-6* shows that the change in ISO range does not drastically affect the steady-state imaging of the camera. In fact, the reduced ISO range image appears a bit brighter. This is most likely due to the sensitivity being held to a higher ISO value as it is limited to being above 1600. However, digitally raising the brightness using the ISO can result in increased noise within the image, which is detrimental to defect detection efforts and should be monitored. Lastly, this method requires determining the minimum ISO value to be chosen. This value should be chosen by incrementally increasing the minimum ISO value until the area of importance becomes overexposed. After reaching this point, reduce the minimum ISO value to the next lowest value. This method ensures that the minimum ISO value will not cause overexposure in the areas of interest and will filter out light sources brighter than this threshold. This ISO value may be different depending on different variables, such as ambient lighting, but can quickly be determined. Based upon these results, determining and setting the minimum ISO was included into the standard operational procedure of the TCR before inspections.

(a) **(b)**

Figure 0-6: Steady state comparison between (a) 100 – 6400 ISO range and (b) 1600 – 6400 ISO range

1.19. Smoothing of Video using Video Stabilization

As shown earlier, during normal operation, the video can shift laterally over a range of 2 in. and rotate by 5° in either direction. These characteristics are not critical to the image collection, as each frame of the video may still be clear and informative despite the rough nature of the video. However, constant shifts and rotations in the video may create difficulties when attempting to track

objects throughout frames, whether manually or via an automated model. These motions may also be frustrating to an operator when reviewing the footage.

To attempt to remedy these effects, tests were conducted to evaluate the effectiveness of the built-in video stabilization programs within the GoPro®. GoPro® Hero8 Blacks contain Standard and Boost video stabilization programs. The Linear digital lens only uses a portion of the imaging sensor as discussed. Both the Standard and Boost stabilization programs further crop the video. Video stabilization is performed by automatically translating and rotating the portion of the imaging sensor used to capture the frame to counteract sharp motions within the video. Cropping the video decreases the area of the imaging sensor used in each frame and allows for more freedom when shifting this portion around for stabilization purposes. Tests were first conducted to image a known-sized grid poster from a constant height under all 3 settings. This test was performed to quantify the decreases in FOV inherent to each stabilization. These tests determined that the Standard stabilization reduced the FOV by 17%, and the Boost stabilization reduced it by 45%, a drastic reduction. Tests were then conducted similarly to the control tests. These tests were conducted at 1, 2, and 3 mph over the Test Bed. The same parallel aluminum tubing was installed at a constant height above the Test Bed. This location and orientation of this tubing were again used to determine the lateral motion and rotation of the image throughout the test. Since the FOV changed with each setting, the scale was distinct as well. The images of the known-sized grid were used to define the scale for each setting.

Figure *0-7* shows the 3-mph video stabilization tests, as they induced the most motion and rotation.

Figure *0-7*a shows a reduction in lateral displacements of the image with both video stabilization programs. Additionally, video stabilization methods nearly eliminate the rotation of the image. Both results are as expected. The side-to-side motion reduction using video stabilization is limited to small motions. Large movements cannot be damped out by the video stabilization. This is because the utilized portion of the sensor may only be translated to the edge of the sensor. Upon hitting the edge, the system has no choice but to show the motion of the camera.

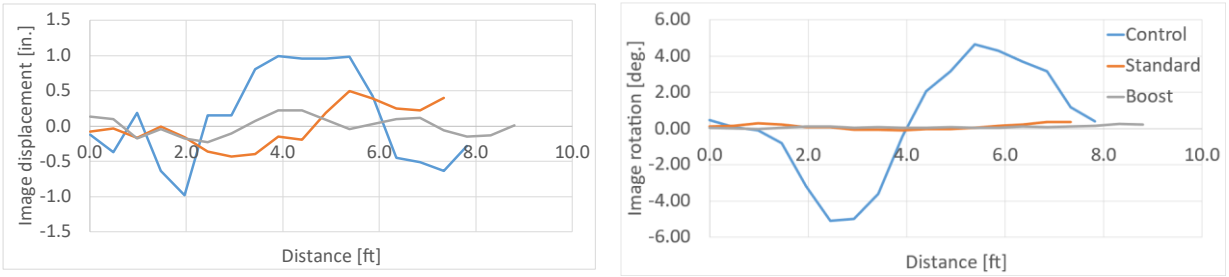

(a) **(b)**

Figure 0-7: Video stabilization 3-mph test results: (a) Image displacement comparison for each test; (b) Image rotation comparison for each test

Therefore, when the TCR shifts a considerable distance laterally, the video stabilization program is unable to make it appear as though no motion occurred. Both settings, however, are extremely robust against image rotations. The presence of rotation is nearly eliminated in both cases. This may be because there is no limit to the ability of the system to rotate the utilized imaging sensor portion in response to the movement of the camera. In both tests, there does not appear to be a considerable advantage when using the Boost setting over the Standard. However, both settings do quantifiably improve the overall quality of the video. The resulting video will be smoother with nearly no rotations, as were seen previously, which may make object tracking and viewability easier. As the Boost setting reduced the FOV considerably, it was ruled out as an option. The Standard setting, however, did reduce the FOV by 17% and was shown to improve the video quality. This setting was chosen to be used during inspections for its benefits.

Chapter 6
Field of View Improvements

As stated earlier, the system must be capable of imaging the entire undercarriage of the railcars to be effective. Every undercarriage component between the rails should be visible from at least one view using the imaging system of the TCR. Without this capability, certain defects that could be visibly identified will be impossible to detect simply by existing outside of the FOV of the system. This section will present the assessment of the initial FOV of the system, subsequent modifications to improve the FOV, and testing with results to demonstrate an ability to image the entire undercarriage.

1.20. Assessment of Initial Design

The existing design's FOV was evaluated by gathering images of a poster with a 1-in. square grid taken at a height of 15 in. The minimum expected component height for hopper railcar gates is about 16 in; however, the TCR should slightly exceed this threshold to image any unforeseen low-lying components and retain a full FOV when not fully centered within the rails. Therefore, the minimum height requirement was defined as 15 in. The photos from this test could be measured using the grid to find the lateral and longitudinal FOV of the current system when imaging the closest components expected. This lateral FOV could then be compared to the required value of 56.5 in. (the standard U.S. gauge width) to investigate the current system's ability to image the entire width of a typical railcar undercarriage.

Figure 0-1 demonstrates that just over 17 in. could be imaged at the minimum height. Therefore, the system was only capable of imaging 30% of the 56.5 in. wide railcar undercarriage at the minimum height.

Figure 0-1: This field of view (FOV) evaluation image shows an ability to image only 17 in. wide at a minimum height of 15 in.

As mentioned in the **Error! Reference source not found.** section, imaging was primarily conducted using the Linear digital lens to correct for image distortion, at the expense of a portion

of the camera's FOV. The SuperView digital lens maximizes the FOV while introducing significant distortions. Similar testing revealed that the SuperView digital lens was still far from adequate for imaging the required lateral FOV using a single camera, Figure 0-2. Additionally, the results showed that the required FOV would be obscured by the current location of frame members and the tracks. Therefore, modifications to the frame, track, and camera configurations were necessary to supply the TCR with the capability to image a railcar's full undercarriage.

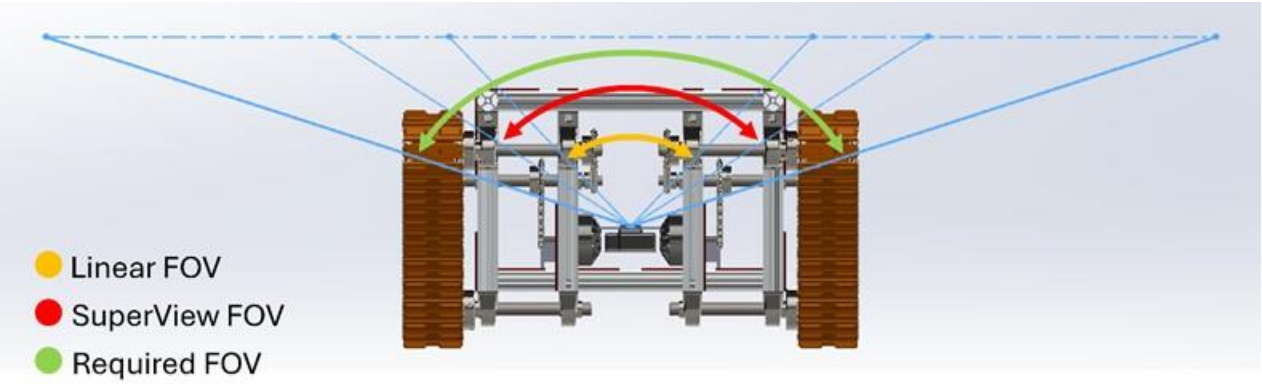

Figure 0-2: Diagram showing the FOV possible with a single camera using the Linear and SuperView digital lenses compared to the required FOV

1.21. Frame Redesign

Portions of the frame needed to be relocated to remove their obstruction from the required FOV while maintaining strength and functionality. 3D modeling was used to identify a potential array of camera angles that could span the undercarriage. This model could then be used to identify the components which interfere with the FOV of the system. The FOV of each camera was physically modeled using the SuperView digital lens, which, as noted, maximizes the FOV of the camera but introduces image distortion around the edges. Using this digital lens in the model ensured that, if needed, the SuperView lens could be used to expand the FOV of the imaging system without obstruction from components.

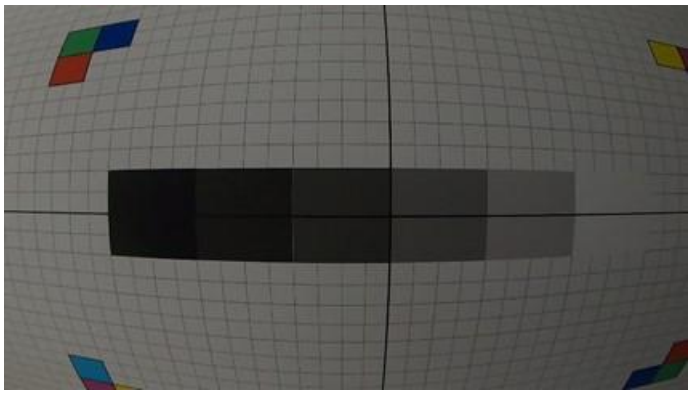

(a)

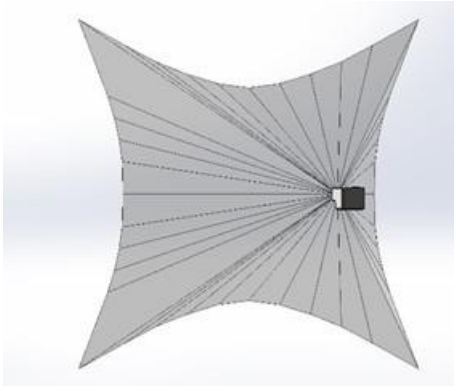

(b)

Figure 0-3: (a) Image of a 1-in. square grid taken from 11.5 in. away using the SuperView lens; (b) Resulting 3D model of the SuperView FOV with a GoPro®

The model was based on an image of a 1-in. square grid taken at a known distance, Figure 0-3a. An imaging processing software was then used to locate the center of the image. Values of the height and width of the image were then measured at regular intervals from the center of the image using the grid lines for reference. Given the effects of the fisheye lens, the height and width increased when moving away from the center of the image, as did image distortion. These measurements were then plotted, creating a 2D cross-section of the camera's FOV. A point was placed at the location of the camera lens relative to the 2D cross-section. Connecting the 2D cross-section to the point representing the lens created a 3D solid encompassing the FOV of a camera using the SuperView digital lens. Finally, a model of a GoPro® was aligned with the FOV model to physically map the FOV relative to the location and orientation of a camera, Figure 0-3b. A sample array of camera angles on the imaging platform was created along with the modeled FOVs, Figure *0-4*a. Cutting the FOV models at a height of 15 in. and a width of 56.5 in. revealed that the resulting FOV from this sample configuration was able to image an entire undercarriage,

Figure *0-4*b. The FOV extends out to the gauge width without exceeding the minimum height of 15 in. and, in fact, well exceeds this mark. When only extrapolated out to the width of the frame, the resulting FOV then highlighted where intersections occurred with the frame members,

Figure *0-4*a. This model was used to verify that any proposed frame redesigns did not interfere with this sample configuration, which, with its FOV, could span an entire railcar undercarriage.

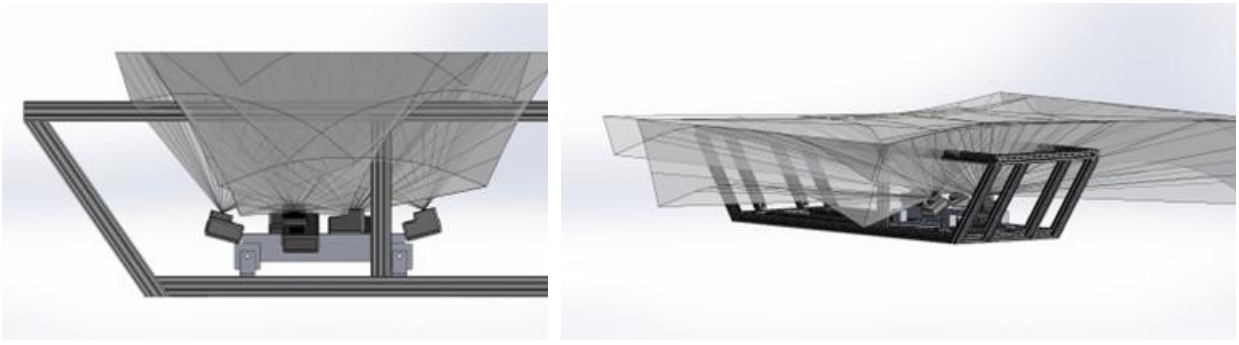

(a) **(b)**

Figure 0-4: Original TCR frame modeled with sample camera setup: (a) Camera FOVs cut to the width of the TCR to highlight the areas of intersection, (b) Camera FOVs extrapolated out to a 56.5 in. width and 15 in. height

Based on these findings, two concepts were drafted, which relocated frame members outside the required area,

Figure *0-5*. The first one, Concept A, shown in

Figure *0-5*b, consists of angled frame members bracketing the newly cleared area with a horizontal frame member between the two. Concept B, shown in

Figure *0-5*c, consists of frame members stretching vertically downward at the edge of the cleared area, with a similar frame member stretching across the resulting gap.

Figure 0-5: Side view of the TCR frame: (a) Original design; (b) Concept A, angled frame member redesign; (c) Concept B, vertical frame member redesign.

A relative FEA analysis was conducted in SolidWorks Simulation between the concepts and the original design to aid in choosing between the two. The XZ-plane cross-section of each, Figure *0-5*, was subjected to a load meant to simulate an impact with a tie. The load was 135 lbs. applied at 60° from the ground plane. The load was transmitted through the bottom surface of the leading, angled frame member to approximate the load traveling into the frame from the leading sprocket assembly colliding with a tie. The lower horizontal frame member was constrained by fixing the cross-section of each end of the beam in space but allowing for rotation to allow flexure under loading. Roller/bearing constraints supported the lateral faces of the top horizontal beams. These fixtures were chosen to constrain the frame within the XZ-plane. The study sought to quantify each concept's relative strength in this plane. Collisions with the edges of ties will transmit forces primarily within this plane and will be the largest shock loads experienced by the frame. Therefore, it was hypothesized that a frame section exhibiting strength within this plane at or above the level of the current frame section,

Figure *0-5*a, would possess adequate strength. The frame was modeled as 6061 aluminum. The framing is 6105 aluminum; however, the two alloys have similar yielding and tensile strengths [62]. The performance of the parts was quantified using a factor of safety (FOS). FOS defines the ratio from the simulated condition within a part to its hypothesized failure criterion, i.e., when the FOS is 2, the condition within the part used to predict failure is at half the intensity of where failure can be expected. In this case, the Von Mises Failure Criterion was used. Von Mises predicts failure when distortion energy per unit volume within the part exceeds a certain threshold. Equation (6-1) defines this criterion in terms of the principal stresses within the part and the tensile yield stress

of the material [63]. SolidWorks calculated the Von Mises stress under the conditions detailed above and compared them to the tensile yield stress, leading to a FOS plot of the entire frame section

$$(\sigma_1^2 + \sigma_2^2 + \sigma_3^2) - \sigma_1\sigma_2 - \sigma_2\sigma_3 - \sigma_1\sigma_3 = \sigma_y^2 \quad (6\text{-}1)$$

Figure 0-6a shows the FOS results for the original frame design. The pink line shows the beam fixed in place but allowed to flex. The pink arrows at the left corner represent the application of the forces, and the green arrows show the location of the roller/bearing fixtures on the top beam. Blue is used to represent any area with a FOS above 5. Red is used to represent a FOS at or below 1, and a gradient is used for the values in between. Three comparable locations of each concept dropped below a FOS of 5: inside the leading corner (Location 1), within the bottommost beam (Location 2), and at the corner of the leading vertical support (Location 3), Figure 0-6. Location 3 varies between the two concepts as each concept's leading vertical support is distinct, Figure 0-6b-c; however, a stress concentration exists at the corner of each. The lowest FOSs for each location have been tabulated in Table 0-1.

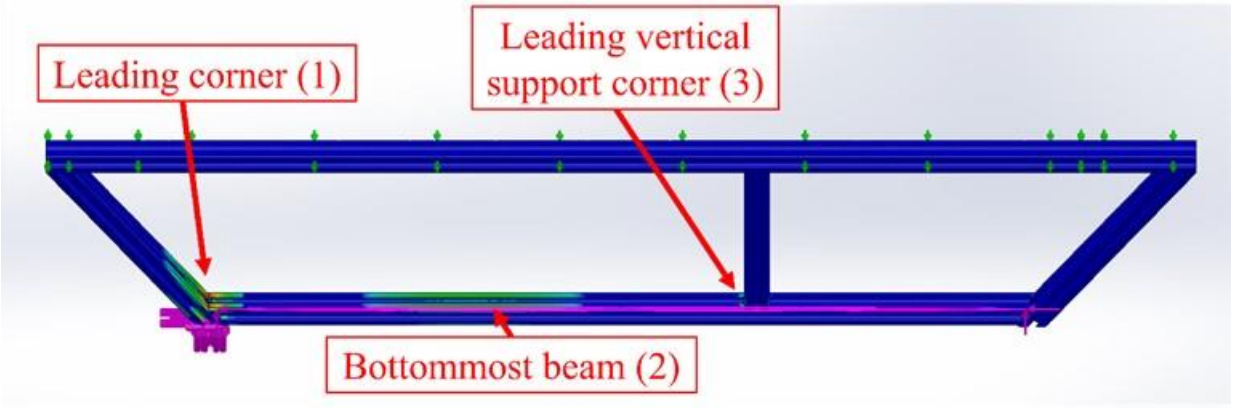

(a)

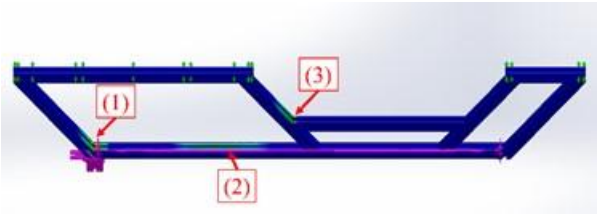

(b)

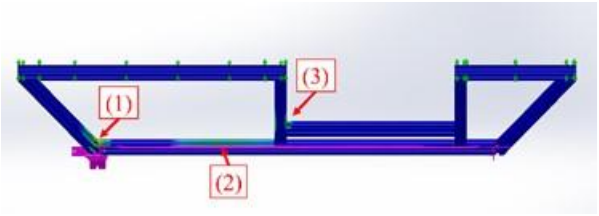

(c)

Figure 0-6: The FEA results for the three frame concepts: (a) Original frame cross-section; (b) Concept A cross-section; (c) Concept B cross-section

Concepts A and B both outperform the original frame's minimum FOS of 1.11, with Concept B marginally outperforming Concept A. However, at the two other locations, Concept A outperforms Concept B. From these results, it was determined that either frame cross-section would be adequately strong for inclusion into the frame. Engineering judgment helped determine that Concept A's angled frame members would more effectively transmit forces than the vertical frame

members of Concept B. Additionally, Concept A saved a slight amount of weight compared to Concept B. Together, these facts led to the conclusion that Concept A should be chosen as the new frame cross-section.

Table 0-1: Factor of safety comparison between each frame concept.

	Location 1	**Location 2**	**Location 3**
Original	1.11	3.28	2.60
Concept A	1.16	3.47	2.03
Concept B	1.21	3.37	1.71

A modal analysis was then conducted using ANSYS to evaluate how the inclusion of Concept A affected the modal response of the frame, with the results shown in Figure 0-7. The lowest meaningful mode for the original and redesigned frame was torsion about the x-axis, Figure 0-7a. The original frame was excited into this mode at 74 Hz. The redesigned frame exhibited a similar mode shape at its lowest meaningful mode. However, the redesigned frame was excited into this mode at a decreased frequency of 67 Hz, indicating a decreased stiffness. This result was expected due to the lack of a continuous top frame member and was undesirable. It was desired to increase the natural frequency of the modes to demonstrate an increase in the frame's overall stiffness. Therefore, a set of transverse frame members was included in the model, spanning the width of the frame between both angled frame members, bracketing the FOV window, Figure 0-7c, and the modal analysis was conducted again. After this inclusion, the lowest mode frequency was raised to 80 Hz. The mode shape appears to be similar to the original torsional mode but is slightly altered. The redesigned frame had now been shown to be as strong and stiff as the original design and was finalized.

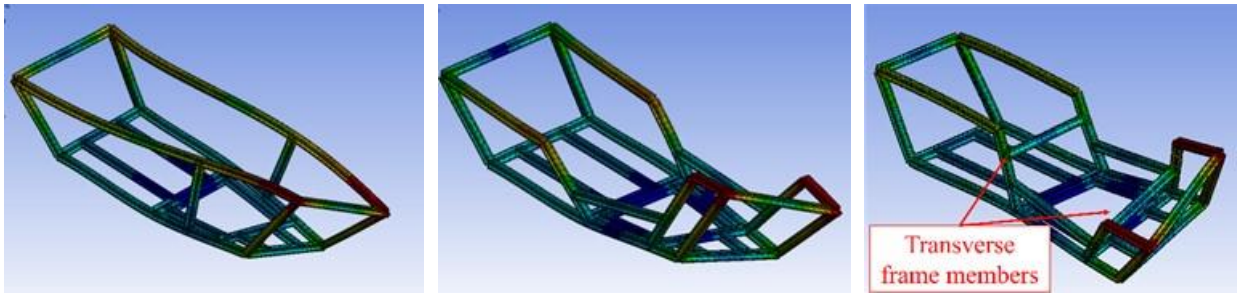

(a) **(b)** **(c)**

Figure 0-7: Lowest frequency mode shape for each frame iteration: (a) Original frame, 74 Hz; (b) Redesigned frame, 67 Hz; (c) Redesigned frame with transverse frame members added, 80 Hz.

1.22. Track Routing Redesign

To route the track below the window created by the redesigned frame, the tensioner and idler wheel assemblies were relocated, Figure 0-8. The tensioner was relocated to the front-angled frame member with its spring fixed to the bottom of the frame, thereby preserving the system's

functionality while modifying it to keep the track as low as possible. The idler wheel was mounted to the rear-angled frame member at a level ensuring that the track remained out of the FOV across the entire width of the window.

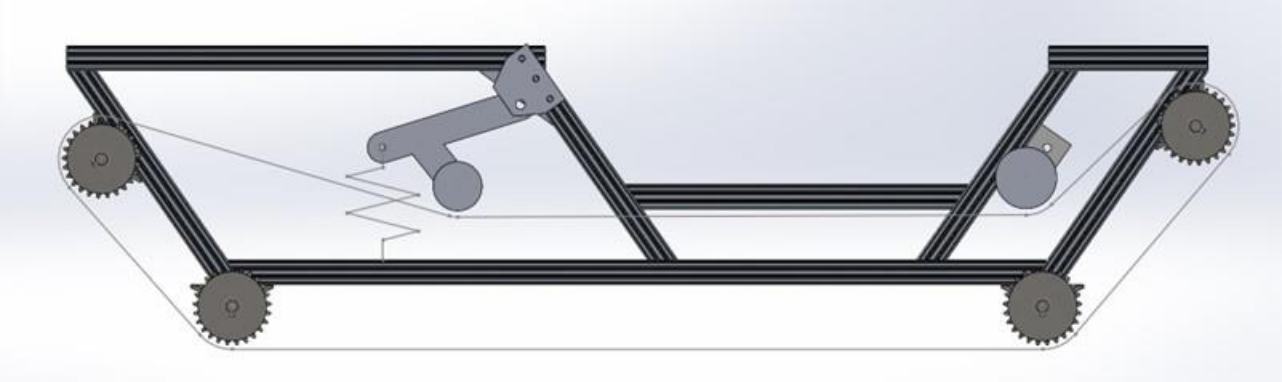

Figure 0-8: Relocated positions of the tensioner and idler wheel assemblies to route the track around the frame window

The changes were initially validated by a 3D model, Figure 0-8. The track's length and thickness were measured. It was then modeled as a belt passing over the sprockets and rollers. The rollers' diameters were directly measured, and the pitch diameter of the ANSI #35 sprockets was used. This model predicted that the relocated components would restrict the track to being located beneath the level of the horizontal frame member, thereby ensuring it remained outside of the required FOV. The design was then finalized.

1.23. Frame and Track Modifications

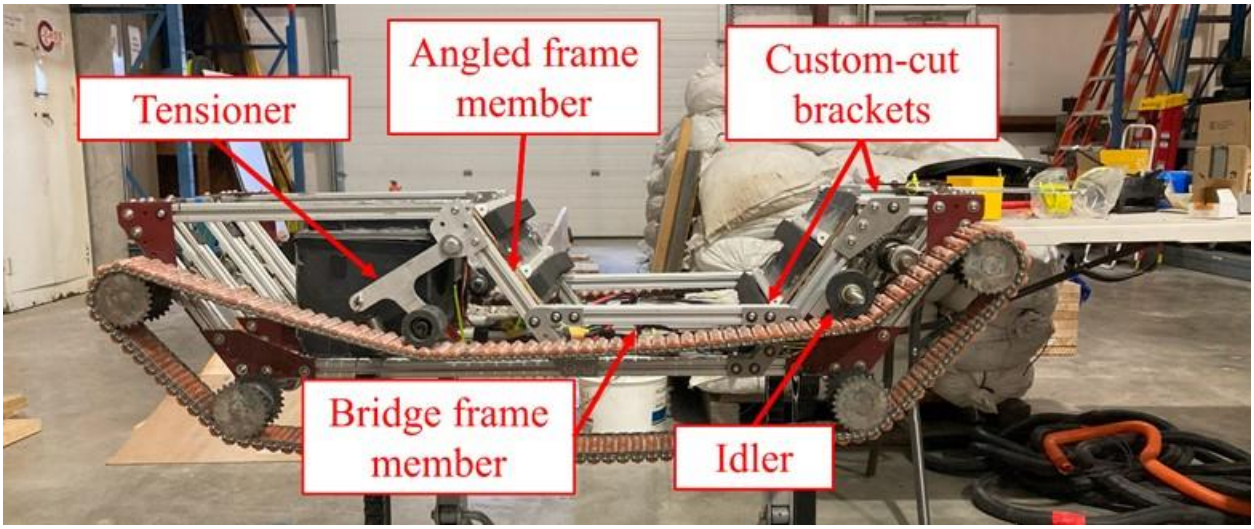

Figure 0-9: Completed frame and track modifications

The angled frame members were cut to modify the frame according to the redesign. First, a section of aluminum tubing was clamped to the outside of the frame at the desired 55° angle. T-slotted

aluminum frame members were then placed on this tubing, which served to align the frame member relative to the TCR. Lines were then marked where the frame member reached the top and bottom sections of the frame. A miter saw was used to cut along these lines to create frame members that perfectly slid between the top and bottom frame members as desired. The bridge frame member was cut on the miter saw. Its length was taken from the 3D model and manually marked and cut. The topmost frame members were cut into two pieces to create the desired gap. Custom aluminum brackets were designed and fabricated on a water jet to secure the angled frame members to the top and bottom of the existing frame. The new frame members were installed using these custom brackets, Figure 0-9. The tensioner and idler assemblies were relocated to route the track beneath the imaging window created by this redesign. Figure 0-9 validates the ability of the relocated tensioner and idler assemblies to constrain the track beneath the level of the imaging window. To note, a bracket was not placed on the exterior of the frame where the leading angled frame member met the topmost frame member as it would interfere with the tensioner bracket. Transverse frame members were cut to length and installed between the angled frame members using standard brackets, as shown during the modal analysis. The light strip panels were installed onto the surface of the transverse frame members to locate them in a similar position to before, Figure 0-10a. Lastly, one vertically oriented camera was removed and replaced by two additional cameras, angled toward the left and right sides, Figure 0-10b. This configuration provided a basic setup for evaluating the imaging system's FOV, although many other camera configurations are possible.

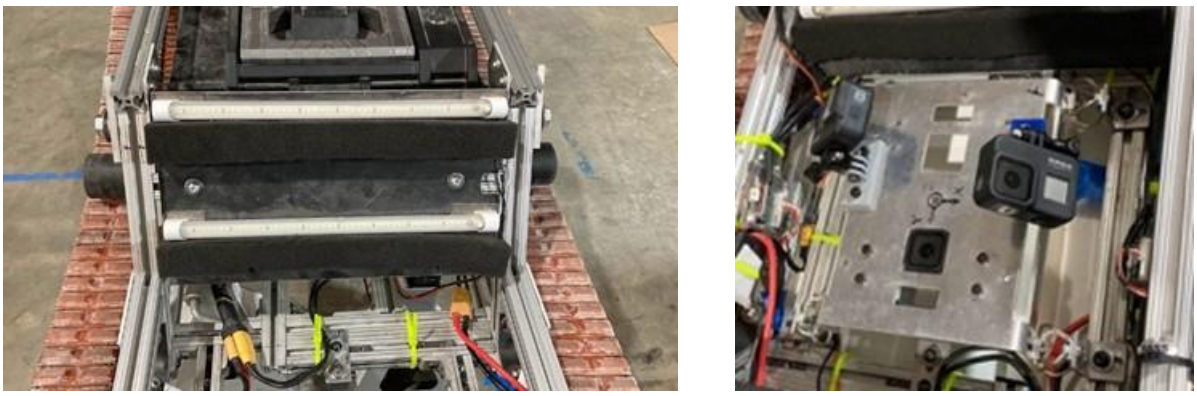

(a) **(b)**

Figure 0-10: (a) LED strip panel shown mounted to the transverse frame member; (b) Redesigned camera configuration, taking advantage of the newly available FOV

1.24. Initial Field of View Validation

To evaluate the ability of the TCR to image the full FOV, a similar test to the initial assessment was conducted. The TCR was placed beneath a poster with a 1-in. square grid, and images were gathered to evaluate the span of the system's FOV. Of note, the width of this poster is 60 in., exceeding the overall width required for full FOV imaging, 56.5 in. Therefore, if the side-view camera angles could image the edges of the poster when mounted at a 15 in. height while also overlapping with the FOV of the vertical camera, it would validate that the modified system was capable of imaging an entire railcar undercarriage. The TCR was centered beneath the poster, and videos were recorded from all 3 cameras. The FOVs of the resulting images were then analyzed.

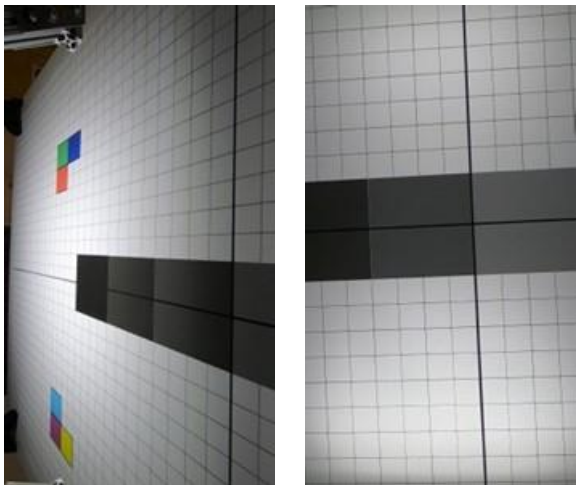

(a) **(b)**

Figure 0-11: FOV validation results show the ability to image from the center to the far edge of the 60 in. poster: (a) Left view; (b) Vertical view.

The images indicate that the TCR is capable of imaging a full rolling stock undercarriage in a single pass. Figure 0-11 shows that the left camera angle can image to the far edge of the 60-in. wide poster mounted at 15 in. while also overlapping with the FOV of the vertically oriented camera. Note that these images were taken with the aid of an improved lighting system that will be presented in the following chapter. This result demonstrates that the FOV now spans the entire 56.5 in. width at 15 in, and the TCR's FOV has been increased from just 30% of the required to 100% while still using the Linear digital lens. Therefore, without any image distortion, the TCR will be able to provide an image of the entire railcar undercarriage from at least one point of view throughout an inspection. This capability is crucial to the development of the TCR. If the system inherently contained blind spots, defect detection in those areas becomes impossible, reducing this platform's effectiveness and the likelihood of its adoption into the industry. Ensuring that each visible component on the undercarriage may be viewed from at least one angle makes defect detection possible across the entire undercarriage. In actuality, the effectiveness of this FOV will only be fully validated when shown to be adequate in the actual working environment beneath railcars, as will be presented in a later section.

Chapter 7
Lighting System Improvements

As detailed previously, the original paper by Molzon and Ahmadian [60] demonstrated the TCR's dependence on ambient lighting conditions. Since this paper's publication and before the current project's start, a lighting system comprised of 4 small light strips was added, totaling 1,800 lm. This lighting system must be assessed to investigate its ability to provide enough light for the imaging system to gather properly exposed images from the entire railcar undercarriage. If found unsuitable, further work must be done to improve the system's capabilities until adequate.

1.25. Assessment of Initial Design

A stationary test was performed to evaluate the original lighting system's performance in relation to the camera's shutter speed. During the test, a stationary target lit by the original lighting system was imaged across a range of shutter speeds. The tests were conducted after sunset to eliminate any substantial ambient lighting and present the most difficult but possible lighting conditions for undercarriage inspections. The tests were conducted at every shutter speed available when shooting at 120 fps with the GoPro® (1/120 – 1/1920 sec.). The tests were performed beneath a tractor-trailer with an undercarriage approximately 4 ft. off the ground. This imaging target was chosen as it approximates the maximum height of undercarriage railcar components, presenting the most difficult lighting condition based on distance. The images were converted to grayscale to highlight the brightness and contrast of each. Results from this test, Figure 0-1, showed that decreases in shutter speed did, in fact, increase image brightness, and adequate contrast was not observed until shutter speeds were at or below 1/480 sec, a setting which allows 4 times more light to the sensor than the desired 1/1920 sec. shutter speed. The lighting continues to improve up to the 1/120 sec. test where it is at excellent levels. The pixel intensity histograms in Figure 0-2 help illustrate the distinct effects of shutter speed and exposure on image contrast. From 1/120 sec. up to 1/480 sec., distinct intensity peaks can be seen in the histogram data, with resolution decreasing as shutter speed increases. The 1/960 sec. and 1/1920 sec. results, however, have a nearly singular intensity peak condensed within a small area of the sensor's range. Although no clipping occurs, inadequate exposure causes significant amounts of contrast information to be lost by becoming overly condensed. From visual inspection and analysis of the pixel intensity histograms, the 1/480 sec. case serves as an example of the minimum acceptable exposure. Achieving this exposure at 1/1920 sec. requires 4 times the light. This exposure level is the first to present adequate contrast, but further increasing exposure continues to improve contrast.

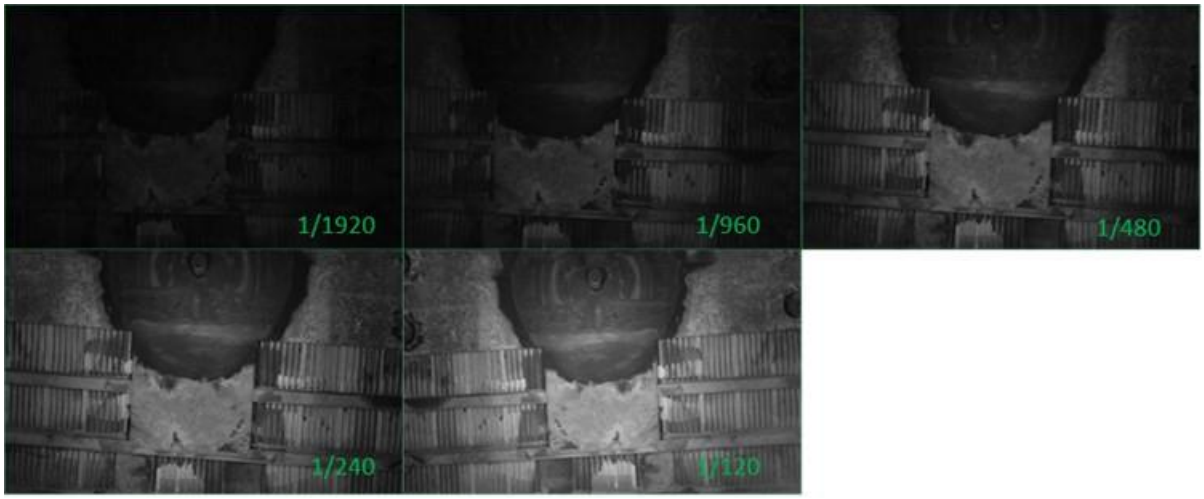

Figure 0-1: Exposure vs. shutter speed image results with shutter speeds shown (sec.)

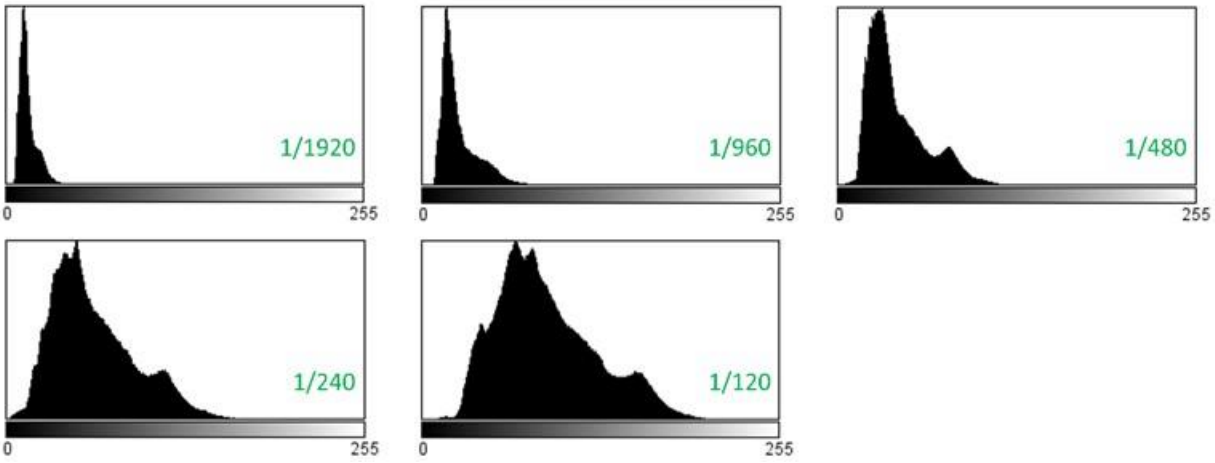

Figure 0-2: Exposure vs. shutter speed pixel intensity histograms with shutter speeds shown (sec.)

Beyond simply investigating the intensity of the original lighting system in the worst-case scenario lighting conditions, the ability of the lighting system to illuminate out to the edge of the required FOV should also be investigated. Therefore, tests were conducted while imaging a 60 in. wide poster at the height of 15 in. The 3-camera configuration presented previously was utilized to capture the full FOV.

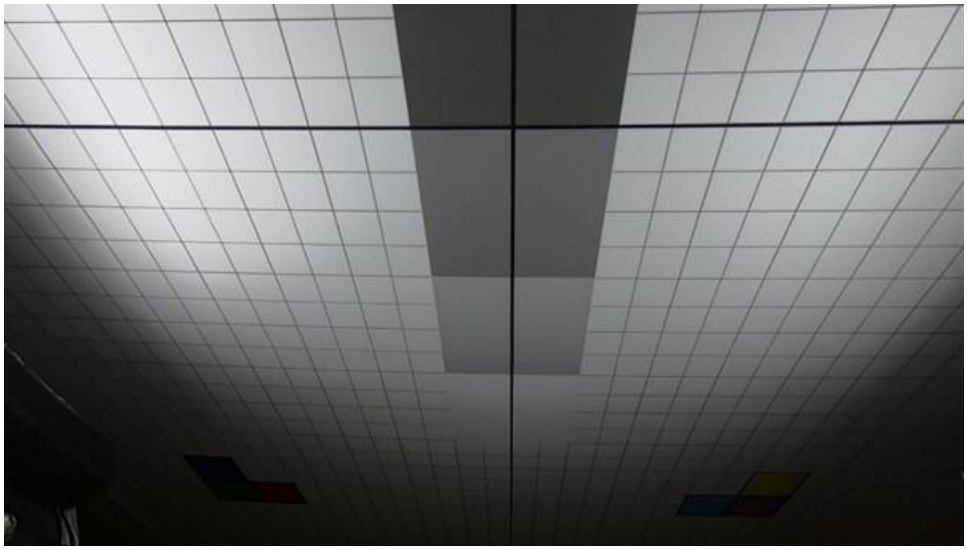

Figure 0-3: Side camera view showing the inability of the original lighting system to illuminate the outer regions of the FOV

From this test's results, Figure 0-3, it was clear that the original lighting system was unable to adequately illuminate the outer regions of the required FOV. Therefore, not only would the overall intensity of the light need to be increased, but its spread would also need to be increased.

1.26. Redesign of Lighting System

As noted, adequate contrast and brightness were not observed in the imaging test until the shutter speed had been decreased by a factor of 4 from the target value. Additionally, the brightness drastically decreased when moving away from the center of the image. The original four LED light strips output a total of 1,800 lm; therefore, the overhead lighting should be capable of at least 7,200 lm and likely more to supply adequate light across the entire FOV, where the original lighting focuses most of its light on the overhead area.

Table 0-1: Improved lighting system parameters

Intensity (per bar)	5,200 lm
Power (total)	120 W
Light bar voltage	12 V
Voltage converter efficiency	< 90%
Estimated current draw	6.9 A

A set of two LED light bars were purchased to evaluate their ability to meet the criteria for the system, Table 0-1. These lightbars were chosen due to their high outputs, low-profile design, and floodlight lenses to spread the beam across a wide area. Together with the original system, these light bars brought the total intensity of the system from 1,800 lm to 12,200 lm, nearly 7 times the original intensity. They were wired into the main circuit of the TCR using a buck converter as the power was too great for the power bank used by the original lighting system. A buck converter outputs a constant voltage given a range of input voltages. The purchased converter outputs the 12

V needed for the LEDs given 9-36 V at up to 240 W. The light bars were initially mounted on the outside of the frame just below the imaging window to provide lighting to the overhead and lateral regions of the FOV, Figure 0-4.

Figure 0-4: Initial configuration of the additional light bars.

1.27. Initial Analysis of Lighting System

The analysis of the improved lighting system began with an identical test to before. The TCR was placed beneath a poster mounted at a height of 15 in. to evaluate the ability to illuminate the full FOV. An image from the right-facing camera during this test, Figure 0-5, shows that although very bright, the light's beam is not being spread nearly as widely as needed. The image suggested that, although floodlights, the light bars may be behaving as spotlights due to the extremely short distance from the light bar to the level of low-lying components.

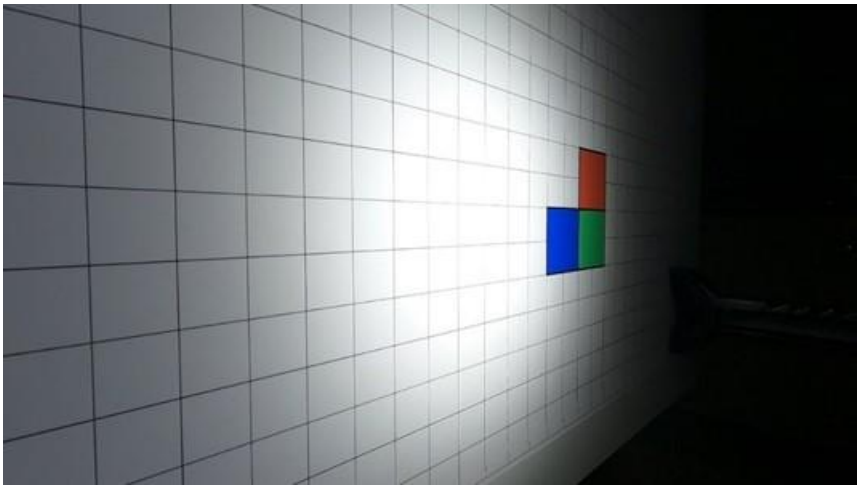

Figure 0-5: Right camera view from the initial test of the improved lighting system

The floodlight lens was not directing its light widely enough for the needs of the project. Behavior closer to that of a Lambertian emitter would be needed. A Lambertian emitter is defined as a light source that provides equal irradiance per unit solid angle, i.e., is equally bright from all angles [64]. While the floodlight lens helps direct the beam into a wide cone, diffusion would be necessary for approaching the behavior of a Lambertian emitter. Light diffusion is the random scattering of light as it interacts with a medium [65]. Mediums causing diffusion will not transmit a clear image due to this random scattering but will rather transmit the light widely and uniformly. As a result, diffusive light also serves to reduce harsh shadows and sharp glares caused by more direct light. Lastly, diffusive mediums will decrease the intensity of the light to some degree, making tuning the diffusion level important for a balance of light uniformity and intensity. To evaluate the effectivity of diffusion for this project, a series of tests were conducted to test the overall performance of the lighting system when using various diffusive coverings over the added light bars, Table 0-2. It was desired to determine which method best illuminated the full FOV while maintaining an acceptable level of intensity.

Table 0-2: Tested diffusive coverings

Control	None
Covering 1	2 layers of wax paper
Covering 2	Frosted plexiglass
Covering 3	Frosted plexiglass and 2 layers of wax paper

To complete this test, a pickup truck undercarriage was used to approximate the railcar undercarriage. Imaging the poster was useful for discovering the spotlight behavior of the added light sources; however, an imaging target more closely related to railcar undercarriages is desirable for evaluating the lighting system's performance. The pickup truck was driven onto 1 ft. blocks over an indoor concrete floor to simulate the approximate height and width of typical rolling stock undercarriage components, Figure 0-6a.

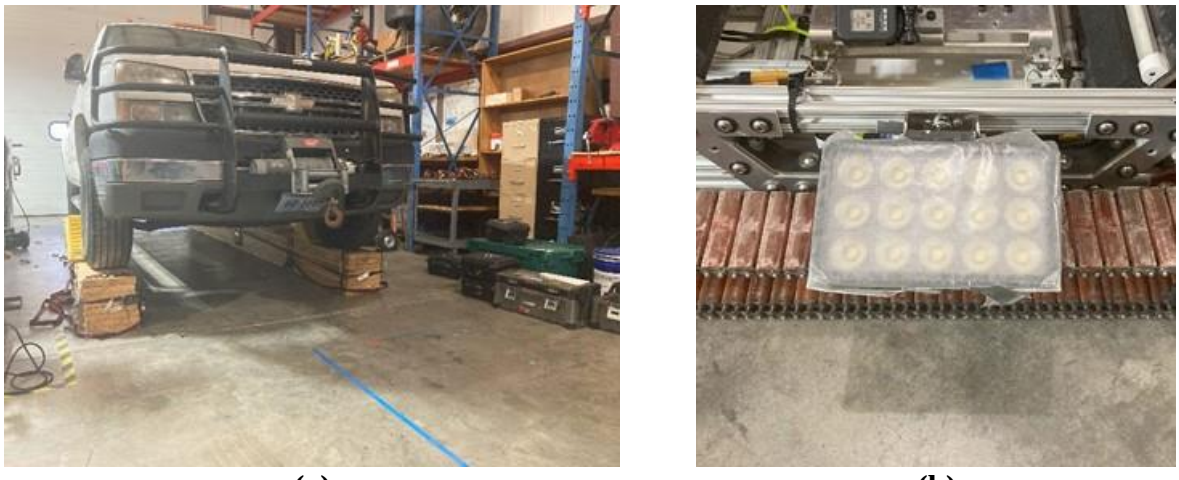

(a) **(b)**

Figure 0-6: Under-truck testing setup: (a) Pickup truck placed on 15 in. high blocks; (b) A sample diffusive covering, two layers of wax paper.

Imaging data was taken from all three cameras while the TCR traveled at 2.5 mph. Again, a 1/1920 sec. shutter speed was utilized as it presented the most difficult conditions for achieving proper exposure. Before each test, the TCR was aligned parallel and centered relative to the truck and located with a short run-up to allow it to reach testing speed before traveling beneath the undercarriage. The throttle was applied as a step input, and an operator manually applied steering inputs throughout the test to maintain the TCR's course. The diffusive coverings were placed over the light bars, as shown in Figure 0-6b. The resulting images were analyzed for lighting effects such as dim areas and glare to draw conclusions about the effect of each diffusive covering.

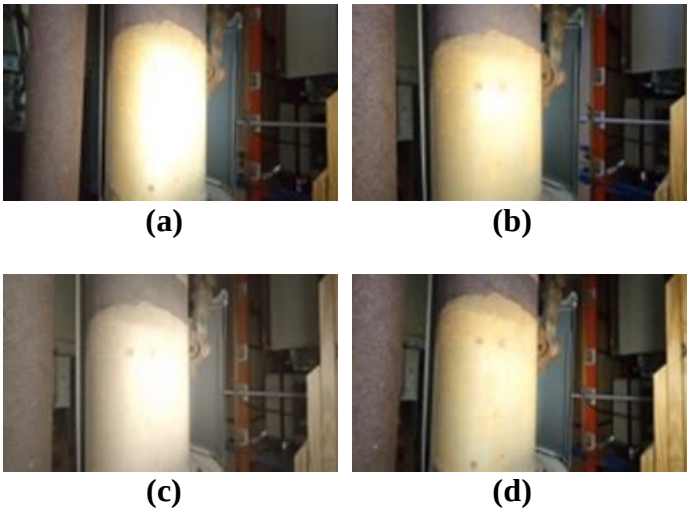

(a) **(b)**

(c) **(d)**

Figure 0-7: Comparison of diffusion methods on glare reduction from muffler: (a) No diffusers; (b) Wax paper; (c) Frosted plexiglass *; (d) Frosted plexiglass and wax paper
*Different color settings used from other tests

(c) **(d)**

Figure *0-7* directly compares imagery using various diffusion methods. Firstly, images of a muffler pipe were analyzed due to its propensity to reflect light, causing saturation. Adequate diffusion will be identified by a reduction in pixel saturation while retaining adequate lighting across the image. From the control image using undiffused light,

(c) **(d)**

Figure *0-7*a, it can be seen that a large portion of the muffler is represented by saturated pixels, eliminating any information that could be gathered from this region. The cases using wax paper,

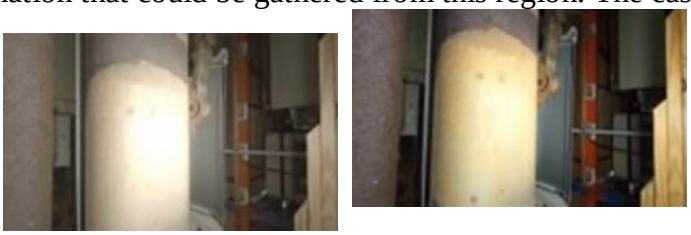

(c) **(d)**

Figure *0-7*b, and frosted plexiglass,

(c) **(d)**

Figure *0-7*c, can both be observed to limit the spread of the saturated region; however, the combination of frosted plexiglass with wax paper reduces pixel saturation most effectively,

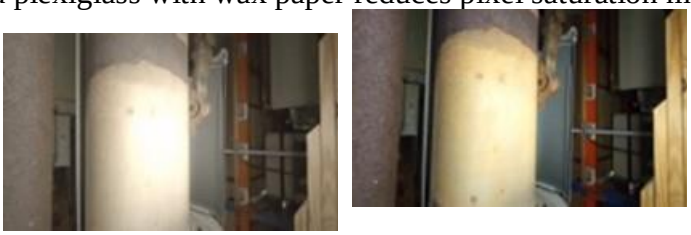

(c) **(d)**

Figure *0-7*d. As diffusion increases, the light illuminating the muffler is less direct, decreasing the reflection's intensity. Additionally, the intensity of the light remains adequate for imaging, although other images should be investigated to validate this point. The combination of frosted plexiglass and wax paper was chosen. Areas of glare are still possible in this configuration; however, the effect is mostly limited to close-up, reflective objects.

Figure 0-8 presents a general image quality comparison between undiffused and diffused lighting when imaging to the side. Images are shown from a side-view camera as the undiffused lighting appeared unable to adequately illuminate the outer lateral regions of the FOV. From visual inspection, both images appear to be adequately lit, which shows the effectivity of the increased intensity of the improved lighting system. However, a few key differences exist between the two sets of images. The left side of the image is toward the center of the truck, where the light bars are located. The right side of the images with the wheels is the outer lateral region. The suspension members appear adequately lit in both cases; however, the tire and the components within the rim are poorly lit in the undiffused case, Figure 0-8a. The diffused case, however, more uniformly illuminates the undercarriage, increasing the detail that can be seen in the outer lateral region, Figure 0-8b. The pixel intensity histograms show that the diffused case leads to a much flatter distribution of intensities than the undiffused case. The undiffused case, Figure 0-8a, has a large spike at the maximum intensity due to the glare from the metallic plate, and the rate of occurrence for intensities across the rest of the sensor's range does not approach this value, except at a single intensity spike on the lower end of the sensor's range. Therefore, although the histogram possesses a high standard deviation of 75, but the contrast content between the two extremes is lacking. For the diffused case, the mode is also located at the maximum intensity as saturation still occurs from the metallic plate, Figure 0-8b. However, the mode occurrence has been decreased by nearly a factor of 3 from the undiffused case (54,000 to 19,000), indicating a large improvement in the imaging of reflective surfaces. The rate of occurrence for intensities across the sensor's range is much closer to that of the mode, indicating more contrast information within the image.

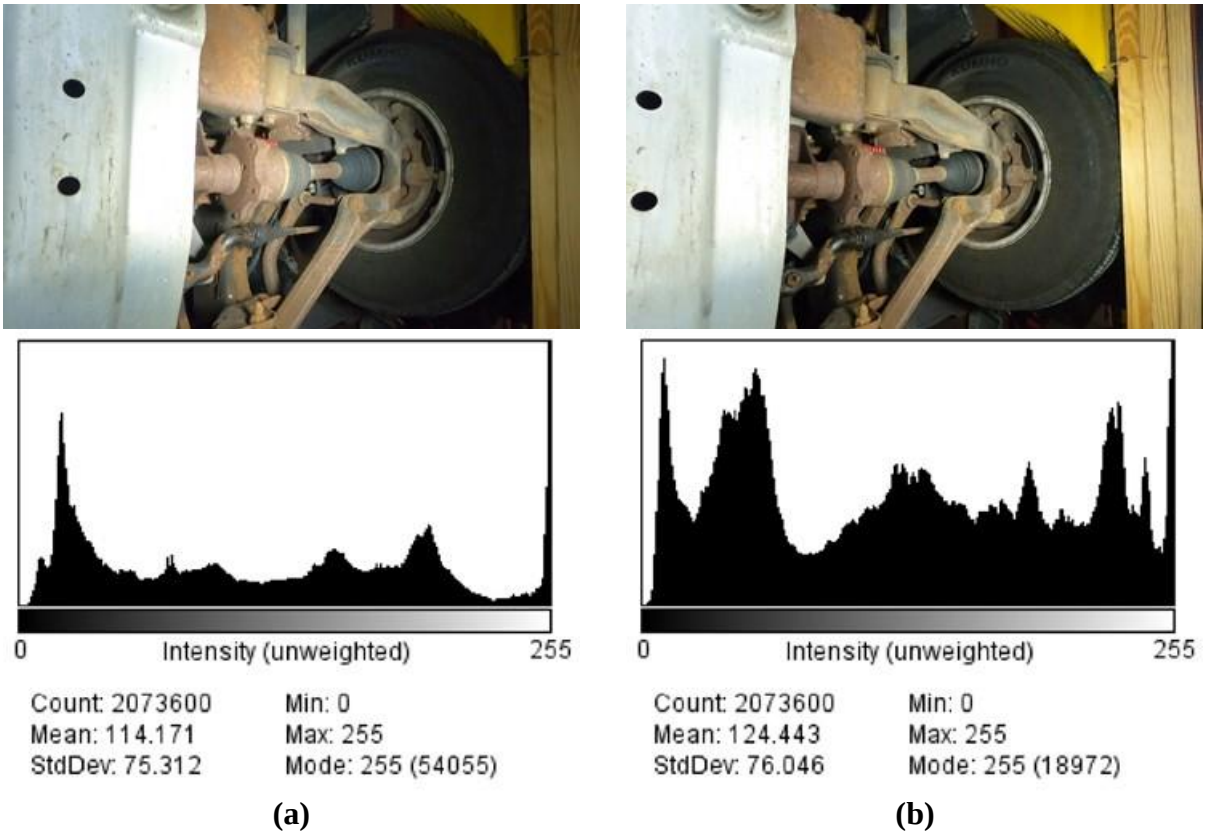

(a) **(b)**

Figure 0-8: Comparison between undiffused and diffused lighting for side-view imagery beneath the truck: (a) Undiffused light image with histogram; (b) Image taken with plexiglass and wax paper diffusion shown with histogram

When observing the lighting of the drive shaft, it is more adequately lit in the undiffused case than in the diffused case. This may be explained by the fact that the drive shaft is located within the span of the light bar's beam and is not highly reflective. These conditions allow it to be imaged adequately under high-intensity, direct light. The diffusion, however, directs more light away from this area and, in general, decreases the intensity of the light to some degree. This effect decreases its lighting quality; however, the diffused light still appears adequate for imaging it. It was determined that this effect was a necessary tradeoff for the benefits of diffused lighting. Lastly, a bit of graininess can be viewed on the surface of the tire in the diffused case. This is likely caused by a high ISO value from the camera increasing the sensor sensitivity and introducing noise. Therefore, it can be determined that when imaging at 1/1920 sec. with this lighting configuration, the system is close to having inadequate light and requires a high sensitivity to reach proper exposure. If the shutter speed may be decreased without introducing significant motion blur, the lighting condition would be improved limiting the effect of noise; however, this cannot be investigated until imaging tests are conducted on rolling stock while traversing the track bed as will be presented in a later section.

The images of the pickup truck's undercarriage using the chosen set of diffusive coverings indicate the ability to light and image a wide FOV at close range. The width between the tires is similar to the rail gauge, and the wheels are mounted at a height of 1 ft., lower than the required 15 in. height. Therefore, these results show the ability to illuminate a greater FOV than required. Lastly, Figure 0-9 demonstrates the improvement from the original lighting system, Figure 0-9a, to the improved lighting system, Figure 0-9b, when capturing images of the overhead undercarriage. The original lighting system focuses most of its light on the directly overhead region of the undercarriage; however, even this region is inadequately lit during the pickup truck test. Figure 0-9b, however, demonstrates an ability to excellently illuminate the overhead undercarriage using the improved lighting system. The close-up metal bar is adequately lit without oversaturation, and the components in the background remain well-lit.

(a)

(b)

Figure 0-9: Vertical image of the pickup truck undercarriage comparing (a) the original lighting systems and (b) the improved lighting system with diffusive coverings

1.28. Positioning Analysis

It was then desired to relocate the light bars so that they would be shielded by the TCR frame in case of collisions. The original location, Figure 0-4, located portions of the light bars beyond the edges of the tracks where they could be directly impacted. To mitigate the risk of direct impact, the light bars were relocated inboard and mounted onto the front transverse frame member. The front LED panel of the original lighting system was removed in order to mount the light bars in this location; however, these LEDs were later mounted to the rear panel to retain the same level of lighting. In this configuration, the light bars could be rotated such that they pointed vertically or towards the outside of the TCR, and it was desired to determine if sufficient light quality could be retained in a certain orientation. Tests were conducted beneath an outdoor tractor-trailer, evaluating the effect of 3 distinct rotations of the light bars. The first configuration, Figure 0-10a, oriented the light bars to illuminate vertically. The second orientation, Figure 0-10b, angled the light bars at a midpoint between vertical and lateral to illuminate both regions. Lastly, the third orientation, Figure 0-10c, configured the light bars in a mostly lateral direction. Videos were recorded from all 3 onboard cameras and used to compare the image quality given the distinct lighting configurations. The shutter speed was again set to 1/1920 sec., and the ISO value was fixed at 3200 for each test. Fixing the ISO and shutter speed values fully defined the exposure of the cameras. Therefore, the pixel intensity histograms resulting from these images could be directly compared in terms of brightness to assess the amount of light captured by each camera. Additionally, the tests were completed consecutively on a clear day leading to similar ambient lighting conditions between the three tests. The TCR was aligned to be centered and parallel to the trailer before each test. A short run-up was included for each test to allow the TCR to reach testing speeds before traversing beneath the trailer. A step input was applied to command the testing speed, and manual steering inputs were applied by the operator to account for any deviations from the desired course.

(a) **(b)** **(c)**

Figure 0-10: Light bar configurations for the positioning analysis: (a) vertically oriented; (b) balanced between vertical and lateral; (c) laterally oriented

Three imaging targets were extracted from the data and used to analyze the performance of each system. Images of the axle and wheel were used for both the left and right camera views, Figure 0-11a & c. This imaging target tested the lighting system's ability to illuminate objects in the far lateral region. Images of the overhead frame rails were used to evaluate the vertical camera view, Figure 0-11b. The trailer frame rails are approximately 4 ft. from the ground, which is approximately the maximum height components may be on a railcar undercarriage. This imaging target evaluates the lighting configuration's ability to project light vertically. The configuration which adequately balances lighting between these two cases would be the most beneficial for this project.

(a) **(b)** **(c)**

Figure 0-11: Images used for positioning analysis. Images are shown from the balanced lighting configuration. (a) left view of axle and tire, (b) vertical view of frame rails, (c) right view of axle and tire

After gathering the appropriate images from each test, the overall brightness of each image was gathered by creating the pixel intensity histogram and calculating its mean. The effective illumination of each lighting configuration could then be plotted in terms of lateral and vertical brightness.

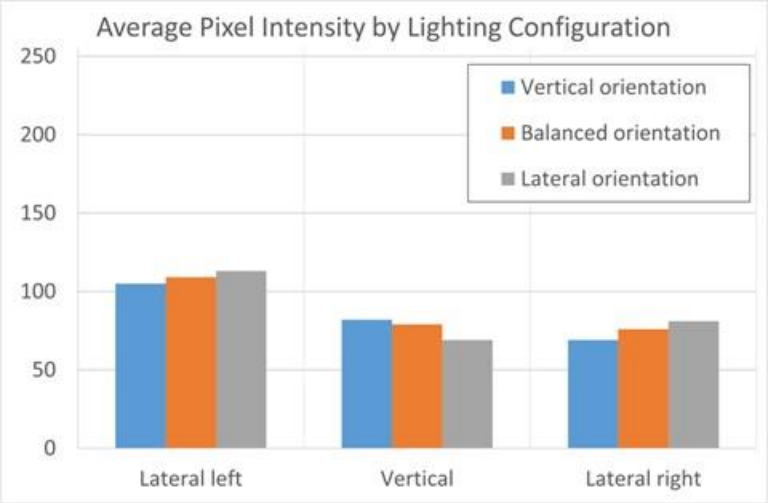

Figure 0-12: Average pixel intensity of each lighting configuration based on camera view

Figure 0-12 shows the average brightness of each camera view for the 3 tested lighting configurations. As described in the **Error! Reference source not found.** section, the brightness is quantified by a value between 0-255, where 0 represents a completely black pixel, and 255 is a fully saturated white pixel. The left camera view is significantly brighter than the other two views. This finding is supported by the images in Figure 0-11. The axle in the left view reflects the lighting strongly, creating saturation and raising the image's overall brightness. Although saturation is undesired, the purpose of this analysis is to compare the amount of light gathered from each camera view based on the lighting configuration; therefore, these images may still be used for this evaluation. The results for each case agree with what may be expected. For both lateral views, the lateral configuration results in the highest brightness, followed by the balanced orientation and, finally, the vertical orientation. The exact opposite is the case for the vertical camera view. The analysis highlights the importance of the light bar orientation to the quality of illumination in a certain area. These results determined that the balanced orientation should be chosen as it is the most likely to perform well at illuminating both the vertical and lateral regions of a railcar undercarriage. However, the performance of this lighting configuration must be evaluated in an inspection of an actual railcar to be fully validated. This evaluation will be presented in a later chapter.

Chapter 8
Operational Control Improvements

As stated earlier, some aspects of the control system for the original TCR need to be improved. The two areas in need of improvement are the speed control and orientation control. The track bed environment consists of rough and varied terrain. As such, the resistance to forward motion can vary significantly. The TCR should be equipped with systems that allow for steady forward motion regardless of the terrain to allow for ease of operation. Additionally, as noted, the operator must steer the TCR to keep it in between the rails and relatively centered. The operator must have adequate visual feedback to apply appropriate steering input to maintain the desired path underneath the railcars.

1.29. Assessment of Initial Design

The issue of inadequate speed control was discovered during preliminary testing within the Test Bed. The preliminary tests involved operating the TCR across the Test Bed to evaluate its dynamics, reliability, and, eventually, image quality. However, it was soon discovered that a step input would not be an acceptable control input as before. Previous tests on concrete and asphalt had utilized a step input without any issues. This step input was communicated to the ESCs, which then mapped the amplitude of the input directly to a motor current. During the initial Test Bed tests, the TCR would become stalled against particularly rough sections or would careen across the Test Bed at unreasonable speeds. In further testing, the control input was applied manually. The operator varied the throttle to account for varying resistances throughout the test to achieve a fixed speed. This method of control requires absolute concentration from the operator and results in a testing speed that varies greatly. From these tests, it was concluded that a method for controlling the speed of the TCR at a constant value with minimal operator interference was needed.

The issue of inadequate feedback for course correction was discovered during the testing under the tractor-trailer. As the TCR passed between the set of wheels at the rear of the trailer, it was completely hidden from sight from the side. The operator had no way of determining the travel path and had to readjust their position to regain a line of sight to the TCR and guide it on its course. The bogies of a railcar similarly obscure the line of sight to the TCR. Additionally, the TCR will be operating in the track bed environment where the terrain is much more likely to push the TCR off course, requiring timely corrections. It was, therefore, determined that a system for providing feedback to the operator was needed. This system would be responsible for conveying information about the location and orientation of the TCR between the rails in such a manner that the operator can quickly and appropriately respond.

1.30. Introduction of PID Control

Under feedback control of the motor current, the Test Bed was causing large speed fluctuations and power stalls during testing as the resistance to forward motion varied greatly. To maintain a constant speed in these conditions, feedback control was necessary. Feedback control occurs when the output of the system is used to modify the applied actuation to achieve a desired result defined by the control input. In this case, by modifying the control method used by the ESCs, the control

input from the radio remote could be mapped to a desired speed rather than a constant current. The utilized motors include integrated Hall effect sensors, which measure the motor speed. The Hall effect sensors in the motor were connected to the ESCs. The signal from these sensors, representing the motor speed, is the output that the ESCs would attempt to bring to a certain value by altering the power supplied to the respective motors. With the sensors connected, the ESCs could read the motor's speed, and PID control was configured. PID control operates by using three tunable parameters to guide the system's response to error between the system's response and the commanded signal. Equation (8-1) shows the standard form for a PID controller.

$$C(s) = K_p + \frac{K_i}{s} + K_d s \tag{8-1}$$

The proportional term, K_p, per its name, proportionally increases the control effort in response to an increase in instantaneous error. As K_p increases, the control effort to combat a given error will increase. A high K_p results in a system that responds quickly to error, but this can also lead to oscillations in the system's response and even catastrophic instability. The integral term, K_i, tracks the cumulative error over time and alters the control signal to drive it to zero. For example, if the response of the system is continually less than the desired response, this term will continue to increase the control effort. The inclusion of this term drives the steady-state error to zero for step inputs. Lastly, the derivative term, K_d, responds to the rate of change of the error. This term helps to decrease large overshoots above the desired value. Table 0-1 shows the utilized parameters in this system.

Table 0-1: PID controller parameters

$\mathbf{K_p}$	$\mathbf{K_i}$	$\mathbf{K_d}$
0.005	0.003	0.00005

The control signals from the radio remote were now mapped to speeds. The ESCs regulate motor effort in accordance with the PID parameters presented above to maintain the commanded speeds. Ideally, the system would now be able to maintain a given speed given only a step input.

1.30.1. Overcurrent Fault Mitigation

After altering the control method to PID, initial tests revealed that the TCR was not operating as expected. The TCR would lurch forward at a given input before suddenly stopping and remaining unresponsive for a few seconds. After investigation, it was determined that the ESCs were experiencing a fault and were cutting the circuit for a moment to protect the components. The fault code was FAULT_CODE_ABS_OVER_CURRENT. The ESCs allow the user to define limiting parameters to protect various components in the system. Two parameters protect the motors from drawing too much current: Maximum Current and Absolute Maximum Current. Maximum Current is the value at which the system will prohibit the drawing of more current. If the current exceeds this value, the system will continue to operate but will quickly reduce the current back to this saturation value. Absolute Maximum Current, however, defines the point above Maximum Current where the system will open the circuit and reset. This setting guards against spikes in current,

which are too drastic to be limited by the Maximum Current setting and threaten to harm components.

Altering the Maximum Current value did little to mitigate the occurrence of overcurrent faults. The ESCs allow for recordings of the onboard current data, and it was observed that the overcurrent faults were occurring before the current ever reached the defined Maximum Current value. In hindsight, this was due to the current spikes being too quick to be recorded and reduced and were, in fact, triggering the Absolute Maximum Current value. The ESCs were found to be rated for 50 A of continuous current and 240 A of instantaneous current. Therefore, the Maximum Current was set to 50 A, and the Absolute Maximum Current was set to 240 A. After this change, the overcurrent faults essentially ceased. The difference between the Maximum and Absolute Maximum settings was large enough that the system had time to measure and regulate the current before exceeding the absolute limit. Previously, the two values were too close together, and spikes would regularly be able to exceed the Absolute Maximum Current before being limited to the Maximum Current value. To note, 240 A is a very large amount of current. The battery itself can only output 240 A continuously, and in theory, both ESCs could be outputting this amount of current in the same instant. However, it is important to distinguish that these are motor current values rather than battery current values. Battery current refers to the current from the battery into the ESC, and motor current refers to the current flowing from the ESC into the motors. These two values will generally be distinct, with the motor current value always being greater than or equal to the battery current. This behavior is because the ESC controls the motor using pulse width modulation (PWM). PWM describes a signal constructed of rectangular wave pulses occurring at a constant frequency with a varying duty cycle. The pulses have a constant amplitude, and the signal has zero amplitude elsewhere. Duty cycle refers to the percentage of the period which the pulse occupies. In the case of the ESC, the battery voltage is applied to the motor using PWM. Therefore, the effective voltage at the motor is the duty cycle multiplied by the battery voltage, always resulting in a lesser or equal voltage to the battery. Due to the conservation of energy, a decrease in the effective voltage at the motor results in a proportional increase in current compared to the battery current. Therefore, for low duty cycles, the motor current will be much higher than the battery current and may reach very high values. This phenomenon explains why the motor current may be absolutely limited to 240 A for each ESC while the battery current will never reach values nearly this high.

After this change, the TCR was able to generally respond to control inputs without triggering the overcurrent fault.

1.30.2. Input Mapping

Another control system issue arose with mapping the control inputs to desired speeds. The ESCs are designed for the control of electric skateboards. In these skateboards, two ESCs will sometimes be paired together to control separate motors; however, the ESCs will be configured in a master-slave configuration where one is controlled and then controls the other identically. For the TCR, steering inputs are necessary. Therefore, the ESCs are operated completely independently, so distinct control signals may be inputted to both. With distinct control signals applied to each, these signals must be manually calibrated to one another such that a given input results in an identical response from either motor.

When initially testing the TCR at a constant speed, it became apparent that the two tracks were traveling at different speeds given an identical input. The input to the ESCs comes in the form of a pulse length (measured in ms) from the radio remote. The ESC calibrates the throttle by reading the remote's minimum, dead stick, and maximum pulse length values, or these values may be inputted manually. It then forms two linear throttle curves defining the control input to commanded speed mapping from -100% to 0% and 0% to 100%. Initially, one side was automatically calibrated, and the resulting pulse lengths were manually inputted to the other side so that the throttle curves would line up identically. During preliminary operations, it was observed that the TCR appeared to undergo constant steering, indicative of a differential in track speeds. The TCR was placed upside down so the tracks would not contact the ground. A constant input was then applied to both motors, and the response was measured using the real-time data recording feature of the ESCs. At this time, Bluetooth data recording had not yet been configured for the ESCs, and data could only be recorded from one ESC at a time using a cable attached to a computer. The mean motor speed could be calculated for a given input. This method found that the left track traveled 0.08 mph quicker than the right at 35% throttle, Figure 0-1.

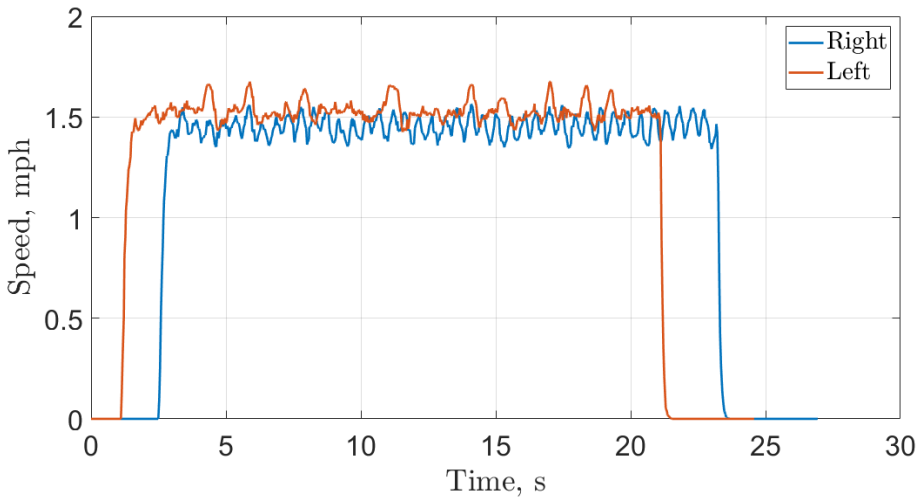

Figure 0-1: Right and left motor speeds in response to a 35% throttle step input. The tests were conducted separately and overlaid afterward

Although relatively small, this value is equivalent to one track traveling 1.4 in./s. quicker than the other, which creates a noticeable steering input while operating. After the speed differential was observed, both sides were recalibrated automatically. It was clear that the pulse lengths from the radio remote did not coincide with one another for unknown reasons, and it was hoped that automatic calibration would eliminate this issue by aligning the minimum, dead stick, and maximum throttle positions between the two ESCs. Table 0-2 presents the original and recalibrated throttle curve values for both ESCs.

Table 0-2: Comparison between the original, automatically recalibrated, and final pulse length values for throttle curve creation

		Minimum (ms)	Dead stick (ms)	Maximum (ms)
Original	Right	1.1410	1.5440	1.9500
	Left	1.1410	1.5440	1.9500
Recalibrated	Right	1.1590	1.5390	1.9380
	Left	1.1400	1.5430	1.9530
Final	Right	1.1590	1.5403	1.9393
	Left	1.1400	1.5430	1.9530

The original values were made identical and were based on the automatically calibrated values for the left ESC. When automatically calibrated, the right ESC has distinct values from the left side. After recalibrating, an identical test to the above was conducted across a range of throttle inputs, Table 0-3. The TCR was again placed upside down, and constant throttle inputs were applied. The average speed was recorded for each motor, and the results were compared to one another. The results show that the right motor consistently ran quicker than the left motor at a given input. On average, the right motor traveled 0.05 mph quicker. The slope of the two throttle curves appears to be in general agreeance, as the difference between the two remains constant. Therefore, it was decided to shift the dead stick and maximum values for the right ESC by the same amount until the two curves were essentially on top of one another. The final pulse length values are shown in Table 0-2

Table 0-3: Right and left motor speeds at various throttle values after recalibrating both throttle curves

	Speed Differential [$V_R - V_L$] (mph)	
Throttle (%)	Auto. Recalibrated	Right Values Shifted
20%	0.055	0.015
30%	0.061	0.010
40%	0.054	0.000
50%	0.046	-0.005
60%	0.048	-0.012

After trial and error, it was found that shifting the dead stick and maximum right motor throttle pulse length values to the right by 0.0013 ms resulted in favorable results, Table 0-3. The slopes do not fully correspond to one another in this configuration, leading to a velocity difference that goes from positive to negative as the throttle increases; however, the maximum speed difference is 0.015 mph at the maximum, only 0.26 in./s. Additionally, the speed differential approaches zero at 2.5 mph, which is within the range of possible operating speeds in the track bed. These results demonstrated that the ESCs were now adequately calibrated with one another and responded similarly to an identical input within the expected operating range of the TCR.

1.30.3. Speed Calibration

It was then desired to calibrate the real-world speed of the TCR to the output of the ESC's real-time data recording. The ESC calculates the TCR's land speed by using the motor's rotational velocity, gear ratio, and drive wheel diameter, i.e.,

$$V = \frac{\omega_{motor}}{Gear\ Ratio} * \frac{D_{drive}}{2} \tag{8-2}$$

The gear ratio and wheel diameter are parameters that are inputted by the user. As noted, the gear ratio of the TCR is 3.939, and the outside diameter of the tracks around the drive sprocket was approximately 100 mm (3.937 in.), Figure 0-2.

Figure 0-2: Measurement used to input the initial wheel diameter

Given this configuration, a set of tests were conducted to evaluate the TCR's land speed compared to the speed outputted by the ESC. The tests were conducted across a 20 ft. stretch of flat asphalt marked by a strip of tape at either end. The TCR was aligned to intersect both strips of tape perpendicularly but was placed a distance behind to allow for accelerating to the test speed. A throttle value was then applied using a switch on the radio remote, creating a step input. The TCR then traversed the distance between the strips of tape at the testing speed while a camera was recording the entire scene from a tripod. The exact frames where the front edge of the TCR crossed the beginning and end of the testing distance were extracted, and the time elapsed between the two was found. This time was then used to calculate the average testing speed at a given throttle. Equation (8-3) converts the time taken to cross the 20 ft distance into a speed with units of mph.

$$V = \frac{20ft}{t_{cross}(s)} * \frac{3600\ s}{hr} * \frac{1\ mi}{5280\ ft} \tag{8-3}$$

These values were then compared to the speeds outputted by the ESC. The tests were conducted at throttle values, which commanded 1-5 mph speeds based on the ESC readings. Table 0-4 shows the results from the first round of testing.

Table 0-4: Commanded vs. actual results for the initial speed validation tests

Commanded Speed (mph)	Time (s)	Actual Speed (mph)	Actual/Commanded
1	16.83	0.811	0.811
2	8.12	1.680	0.840
3	5.42	2.518	0.839
4	4.03	3.381	0.845
5	3.25	4.196	0.839
		Average	**0.835**

The initial results revealed that the TCR was consistently traveling at a slower speed than commanded. The ratio between the actual and commanded speeds remained relatively constant at 0.835. Therefore, it was determined that there was some form of disconnect between how the ESC was calculating speed and the speed achieved. After investigation, the wheel diameter appeared to be the most likely point of error. The measured diameter, Figure 0-2, of 100 mm (3.937 in.) was measured from the outside of the tracks. However, when wrapped around the sprocket, the tracks fan out, creating a farther distance to travel between them than when lying flat. The true land speed of the TCR depends on the number of chain links being driven through the sprocket. The chain links serve as the pivot location for the tracks; therefore, the distance between them will not change. By using the diameter through which the links pass, as opposed to the outer diameter, the calculated land speed by the ESC should become much more accurate. From the data, the wheel diameter parameter should be reduced by a factor of 0.835. Beginning with the 100 mm (3.937 in.) value, this leads to an 83.5 mm (3.287 in.) wheel diameter. The modified wheel diameter is much closer to the drive sprocket's pitch diameter of 2.992 in. This makes sense as the chain links should generally travel through the path formed by the pitch diameter.

Before the above tests could be repeated with the modified pitch diameter value, the throttle curve within the ESCs had to be recalculated. With the altered parameters, the ESC would now calculate a different land speed given a certain rotational speed at the motor. The new mapping between throttle values and ESC calculated speeds had to be documented to compute the commanded speed, which would be compared to the actual speed. At this point, the above-described input mapping work was conducted, where the pulse length values for each ESC were calibrated to produce identical responses. The validation results, comparing the left and right speeds to one another after calibration was completed, Table 0-3, were used to then create the throttle curve. A line of best fit was used to compute the resulting throttle curve from the results of both the left and right motors, Figure 0-3. The line of best fit was constructed in MATLAB using POLYFIT. The left and right speeds are visibly in agreeance with one another, and they increase linearly with the throttle percentage.

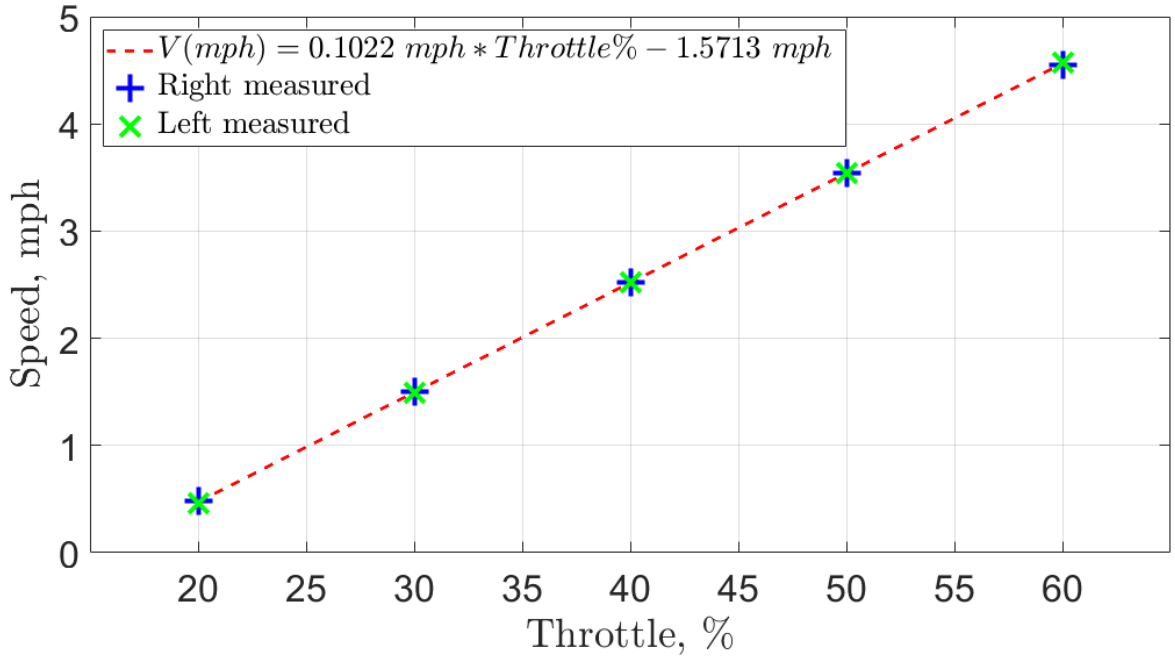

Figure 0-3: Throttle curve resulting from a line of best fit relating motor speed to the applied throttle percentage

With the commanded speed now known, it was possible to compare it to the TCR's actual operating speed by completing the timed tests across a 20-ft. distance. Table 0-5 presents the results from the second round of testing. The throttle values are included for reference, and the 1-5 mph commanded speeds are computed with greater precision than in the previous test to compare the two sets of speeds more precisely.

Table 0-5: Commanded vs. actual results for the speed validation tests with the modified wheel diameter and throttle curve

Throttle (%)	Commanded Speed (mph)	Time (s)	Actual Speed (mph)	Actual/Commanded
25	0.98 (1)	13.5	1.01	1.03
35	2.01 (2)	6.8	2.01	1.00
45	3.03 (3)	4.55	3.00	0.99
55	4.05 (4)	3.35	4.07	1.00
64	4.97 (5)	2.70	5.05	1.02
			Average	**1.01**

The results demonstrate an excellent ability to control the TCR's land speed using a given throttle percentage. On average, the TCR travels 1% quicker than commanded. The predicted speeds now closely correlate to the actual speed of the TCR. In future testing, the speed data gathered from the ESC can confidently be used for evaluation of the TCR's speed in the track bed. The TCR's ability to maintain a commanded speed in the real-world inspection environment must be validated, as will be presented in a later chapter of this paper. With this work completed, the PID control system

had now been shown to be robust to current spikes, calibrated between the two ESCs, and an accurate predictor for real-world speeds.

1.31. Improving Control Using a First-Person View System

As noted, it was determined that a method for providing the operator with real-time video footage from the TCR to serve as control feedback should be included in the design. First-person view (FPV) camera systems are used extensively in the drone market to stream real-time footage from an onboard camera to a monitor at a very low latency (< 30 ms) [66]. Adding such a system to the TCR would allow the operator to always view the TCR's heading and position, providing the necessary information for timely and precise steering inputs; however, latency, vibrations, and adverse lighting conditions present challenges for consistently and effectively conveying this feedback to the operator. To add the FPV system to the TCR, various components were purchased. The FPV camera (5.8 GHz video transmitter) was chosen as a low-profile camera and transmitter combination, and a compatible monitor (4.3 in. 5.8 GHz FPV monitor) was chosen for displaying the camera's transmissions. The monitor can also record the transmitted videos for analysis after a test. A set of 3.7V, 2000 mAh Lithium batteries were purchased to power the FPV camera. The FPV camera is stated to consume 500 mA during typical usage, giving each battery an estimated lifetime of 4 hours, much longer than needed for an inspection.

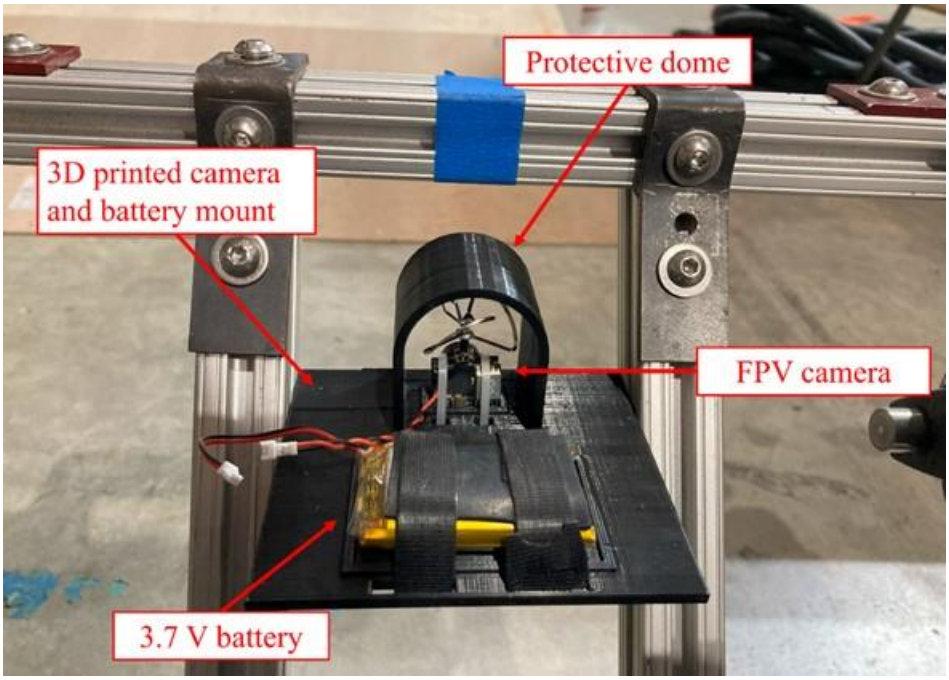

Figure 0-4: FPV camera mounting location at the front of the TCR.

The FPV camera was mounted at the front of the TCR between two frame members,

Figure *0-4*, to capture a useful camera angle while remaining protected by the frame. A mount was 3D printed to locate the camera and battery in place with a dome added to protect the camera's

antenna. The mount included slots for zip ties to secure the FPV camera and for Velcro straps to secure the battery.
Another set of 3D printed mounts, shown in Figure 0-5, secures the monitor to the radio remote so the video feedback would remain readily viewable while operating the TCR. The monitor mount consists of three parts. One creates a friction fit with the radio remote antenna and is further secured to it with a zip tie, providing a mounting location for the other pieces. The other pieces bracket the top and bottom of the monitor. The two parts mate together with a set of compatible pegs and holes. Zip ties are then used to clamp the two pieces together, securing the monitor. These parts are then mounted to the friction-fitted part via a set of tabs on each part, which interlock together and allow a bolt to pass through, securing the parts together while allowing for angle adjustments.

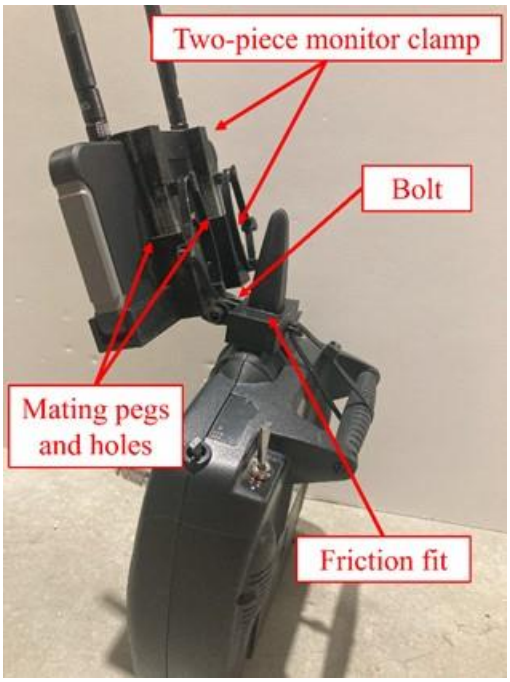

Figure 0-5: 3D printed parts mounting the FPV monitor to the radio remote

Initial tests revealed that the FPV camera would build up heat rapidly. An infrared temperature sensor pointed at the camera read temperatures up to 185 °F after approximately 5 minutes of operation. Sources indicate that conventional electronics are designed to withstand 160 °F while it is best practice to limit temperatures to 105-120 °F [67,68]. Therefore, the system was well outside of the range of recommended temperatures and at risk of failure. These cameras are often used on racing drones. In this case, the camera will be surrounded by high-speed air which will aid in cooling. In comparison, the speed of the TCR is very low, and supplemental cooling may be required. In response, a 12 V, 0.1 A computer fan was tested for its ability to cool the FPV camera. A modified version of the camera and battery mount was 3D printed to include the fan in the design, Figure 0-6. A large hole was placed in each wall of the protective dome, allowing air to pass perpendicularly across the camera. This configuration was chosen as the FPV camera consists of two main circuit boards parallel to one another and perpendicular to the direction of filming. Therefore, air passing perpendicularly across the camera would flow around and between these circuit boards, minimizing the chance of areas being unreached by the air. The fan was hot glued

to the surface of the new mount, and a mounting location was included for the 11.1 V LiPo battery used to power it.

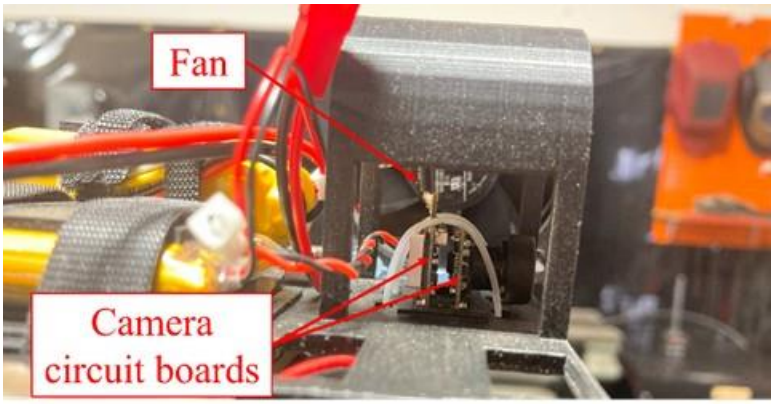

Figure 0-6: Modified camera mount to include the cooling fan

A control test was conducted using a calibrated thermocouple to measure the uncooled rate of heating of the FPV camera. The thermocouple was calibrated by measuring the temperature of ice water, ambient air, and hot water and comparing the measured voltage with the reading of a food thermometer, leading to the following calibration curve, Figure 0-7. The thermocouple voltages were measured to the microvolt level. The resulting calibration curve closely agrees with the gathered data points, and it was used to convert the measured voltages to temperatures in each test.

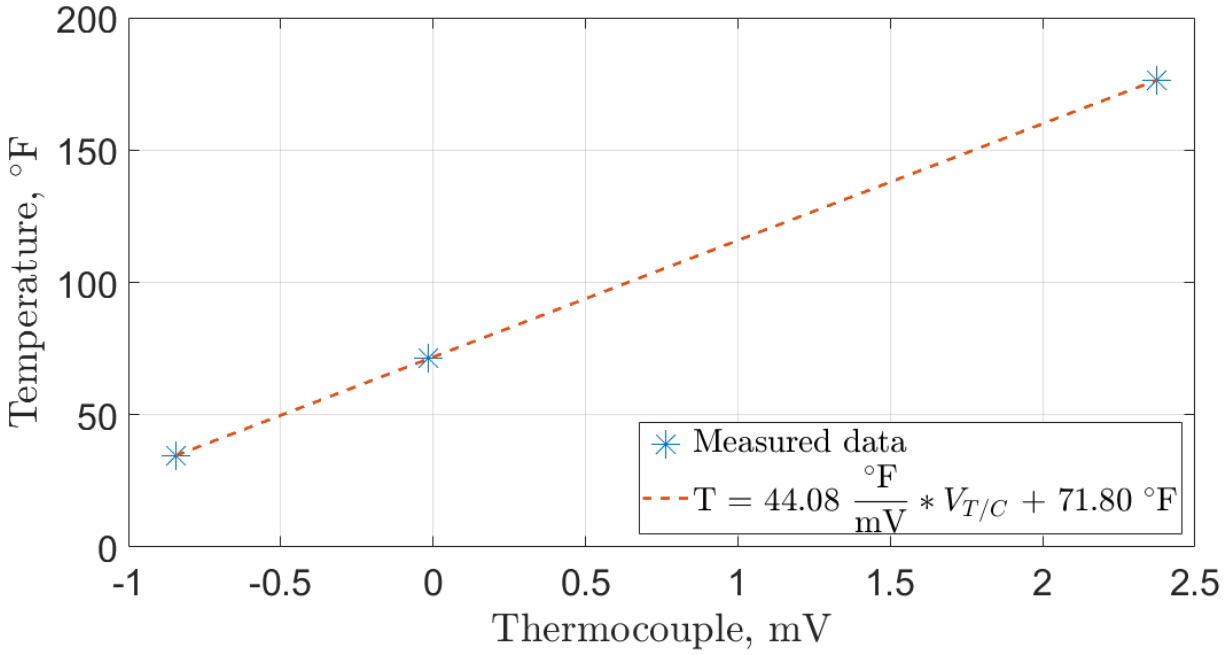

Figure 0-7: Thermocouple calibration curve with the data points gathered to create it

Before conducting the control test, it was desired to find the hottest location on the FPV camera at which to measure temperature for both the control and cooled tests. The fan and camera were

powered on for approximately 5 minutes before contacting the thermocouple across the camera's surface to find the hottest location. It was found that the bottom center of the rear circuit board held the highest temperature, being around 0.2 mV (9 °F) higher than most other locations on the camera. Temperature was measured from this location during both tests. The control test was then conducted. With the thermocouple held to the camera, the FPV camera was powered while a video recorded the readout of the multimeter. The monitor was powered throughout the test, to visually validate that the camera was continuing to operate correctly. This test ran until the multimeter reached 2.1 mV, indicating temperatures greater than 160 °F. Secondly, a long-term cooled test was conducted with the fan in operation. This test ran for 35 minutes with thermocouple readings collected at time intervals, which increased from 20 seconds to 5 minutes throughout the test. The thermocouple was not constantly applied to the camera during this test to avoid interfering with airflow; therefore, the thermocouple was applied only for a few seconds before a steady-state value was reached and the data point was recorded. Lastly, the ambient temperature was noted before and during each test and remained nearly constant throughout.

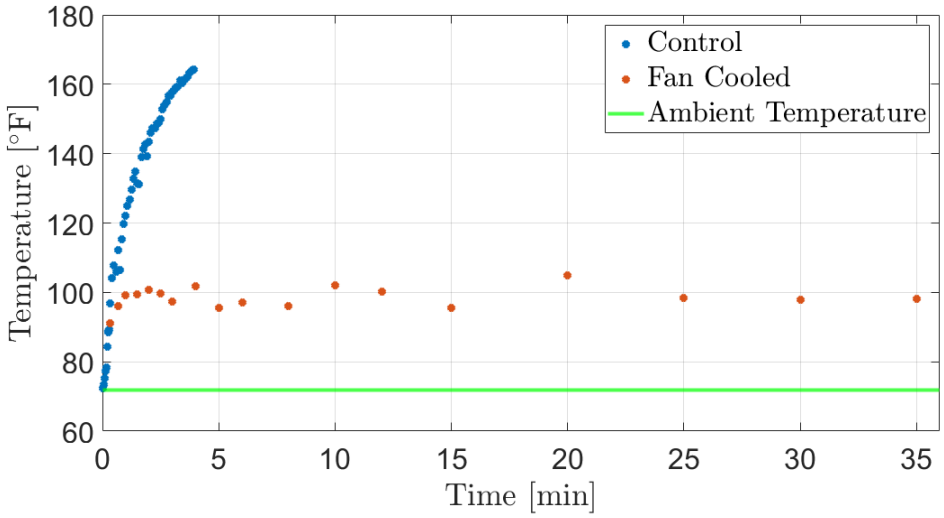

Figure 0-8: FPV camera cooling test results

The FPV camera cooling test results, Figure 0-8, demonstrate the hypothesized rapid heat buildup in the uncooled FPV camera. The camera reaches temperatures above 160 °F within 4 minutes of the test starting, temperatures that could prove harmful or even fatal to the camera if prolonged. The first portion of the cooled test, interestingly, shows similar heating dynamics to the uncooled test up to around 95 °F; however, the lower resolution of this data due to the inability to maintain continuous thermocouple contact during the cooled test hides the exact shape of these initial dynamics. After this point, however, the cooled results rapidly flatten, settling at approximately 95 °F for the remainder of the test with a maximum temperature of 105 °F occurring at 20 minutes. This test demonstrates the ability of the cooling fan to limit heat buildup in the FPV camera and maintain its temperature below hazardous values when operating at an ambient temperature of 72 °F, although its effectiveness may be reduced at higher ambient temperatures. Based on these results, the cooling fan was used to cool the FPV camera and was powered during all future testing. Tests were conducted to evaluate the viability of the installed FPV system. The TCR was driven across the length of the Test Bed at 3 mph using only the FPV system to provide feedback to the

operator. As will be shown in a later chapter, 3 mph is slightly above the TCR's maximum reliable and controllable speed within the track bed. Therefore, the test was used to qualitatively evaluate the system's latency and robustness to vibrations at the maximum operating speed in the rough Test Bed terrain. If latency were too high, the operator would not have enough time to precisely adjust the course of the TCR throughout the test. Additionally, if vibrations seriously degrade the quality of the video feedback, the FPV system may be rendered useless. Also, the Test Bed is narrower than a standard track bed leading to a more difficult control scenario than will be regularly experienced during inspections. The TCR was located a short distance behind the Test Bed and aligned parallel with it to allow the system to reach testing speed before traversing it. The throttle was applied as a step input using a switch on the radio remote. The footage from the FPV camera was recorded for analysis.

Figure 0-9: Frame from the FPV camera footage during the 3 mph Test Bed evaluation

This testing showed that the FPV system was sufficient for providing feedback to traverse the Test Bed at up to 3 mph. The TCR was successfully controlled across the entire Test Bed without contacting either side. This test qualitatively demonstrates that the FPV system operates with low enough latency to be sufficient for feedback even when large disturbances are present and that vibrations will also not degrade the video footage to the point of becoming unusable. The vibrations did not appear to greatly blur the images, and although low resolution, the video feedback remained clear throughout testing, Figure 0-9.

Another set of tests was conducted to evaluate the effectiveness of the FPV system for control during under-trailer testing. These tests evaluated the ability of the FPV system to operate under similar lighting conditions as will be seen beneath the rolling stock. On clear days, traversing between cars will expose the FPV system to highly variable lighting conditions. The area between railcars will be substantially brighter than the area beneath them. If the FPV system cannot quickly adjust to these lighting changes, the footage will exhibit poor contrast or saturation for a substantial period. The footage will become unusable for feedback during this time, making precise course adjustments impossible. To investigate these effects, tests were operated at speeds up to 6 mph, which further evaluated the effects of the system's latency on overall controllability.

(a) **(b)**

Figure 0-10: Images from the 6 mph under-trailer test: (a) Image taken as the TCR passes under the rearmost axle of the trailer, (b) Image taken 0.24 s later when the camera has readjusted to the scene

Tests conducted at 6 mph beneath the trailer indicate the FPV system's ability to operate in similar lighting conditions as seen beneath the railcars. The FPV camera effectively altered its sensitivity to provide a clear image both beneath the trailer and the sky, although, as expected, periods of saturation or dimness occurred when transitioning from dim to bright and vice versa, respectively. Figure 0-10 shows one such transition as the TCR travels into a brightly lit area from beneath the rearmost axle of the trailer. Figure 0-10a shows an image while the TCR passes beneath this axle. The scene directly ahead is almost completely saturated, making effective navigation difficult. The underride guard located directly in the TCR's path is almost invisible. If this component were an obstacle in the TCR's path, the operator would most likely not have identified it at this point. Figure 0-10b is taken at the first moment when the FPV camera has effectively adjusted to the new lighting conditions. This frame occurs 0.24 s. later in the video. A quarter of a second can be a significant length of time; however, at the operating speed of the TCR, the transition period does not appear to pose a critical risk to controllability. Additionally, these tests demonstrated that the system was able to be controlled at more than twice the track bed operating speed without detrimental effects due to latency. The FPV had now been tested in similar vibratory and lighting environments as will be seen beneath railcars, and the system was deemed fit. A later section will cover the final validation of the system in the real-world inspection environment.

Chapter 9
Mobility and Reliability Improvements

The TCR's mechanical performance may be divided into two categories: mobility and reliability. Mobility refers to the TCR's ability to consistently and quickly perform maneuvers necessary for undercarriage inspections. The most difficult maneuvers are rail climbing and turning within the rails. The TCR must be able to reliably perform both maneuvers to conduct inspections without manual assistance. As noted earlier, the TCR will be deployed trackside before climbing into the track bed and conducting the inspection without any manual assistance. Reliability refers to the TCR's ability to withstand the forces inherent to climbing the rail and operating on the rough terrain that is inherent to railroad tracks, without any component failure.

1.32. Assessment of Initial Design

The first evaluations of mobility and reliability were constant speed tests across the Test Bed. The TCR was placed a short distance from the ramp of the Test Bed to allow it to reach testing speed before traversing. The TCR's performance was evaluated using video images. At speeds below 3 mph, the TCR was observed colliding with the edges of the ties, but the collisions did not appear significant, with a few causing the front end of the TCR to become slightly airborne. However, at 4.25 mph, the TCR was violently jolted by collisions with ties, and the front end became airborne to a more significant degree, Figure 0-1a. As noted, the TCR has no suspension. Collisions such as this impart large shock loads into the idler sprocket assemblies. It was determined that speeds above 3 mph would not be attainable with the current configuration but determining the maximum controllable and reliable speed would require further investigation. During these tests, it was suspected that the undercarriage bearings and housing were being contacted by the ballast. To investigate this, a camera was placed at the end of the Test Bed to film the interaction between the ballast and undercarriage components throughout the test. Video from this camera clearly showed the bearing housings being impacted by ballast, Figure 0-1b. Further inspection of these components revealed that they all showed signs of impact, and a few of the bearing housings had become deformed to the point of no longer securing the bearings and axles in place. From this evaluation, it was determined that the current idler sprocket assemblies would need to be redesigned such that the bearings and housings would no longer be vulnerable to consistent impacts.

(a)

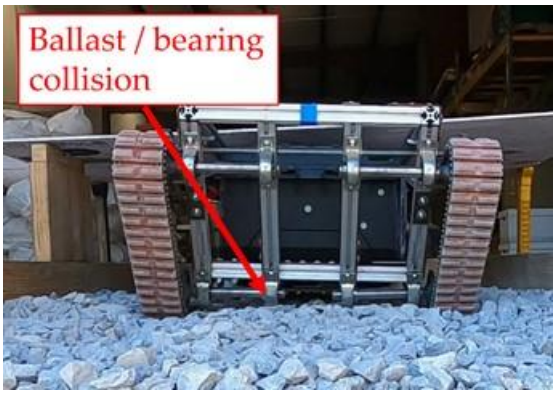

(b)

Figure 0-1: Test Bed evaluation results: (a) Sharp collision during 4.25 mph test causing the front end of the TCR to become airborne; (b) Impact between the ballast and bearing housing

Tests were then conducted to evaluate the ability of the TCR to climb in and out of the track bed and perform a turn within the track bed. As a note, different sizes of rail are used for different applications. The variants are identified by their weight in pounds per yard. As this number decreases, the cross-sectional area of the rail decreases, as does the height of the rail. Class 1 railroads often use 136 lb/yd rail; short-line and regional railroads may use 115 lb/yd rail or other smaller variants. The TCR should be capable of climbing each widely used rail cross-section. These tests were conducted on a set of local tracks using 115 lb/yd rail. The TCR was placed trackside, and the test involved attempting to climb into the tracks, turn 90°, travel a short distance, turn 90° further, and climb back out of the tracks. The TCR was controlled manually throughout the process. Data was gathered from both ESCs during this testing via Bluetooth. This data included motor speed and motor current measurements throughout the test that could be used for later analysis. As a note, these tests occurred after the idler sprocket assemblies were modified in response to the abovementioned issues.

(a) **(b)**

Figure 0-2: (a) TCR shown stuck rail climbing as the edge of the protective plate impacts the rail; (b) the protective plate mounted to the TCR's undercarriage

During the rail climbing portion of the test, the TCR was unable to consistently climb over the rail, stopping many times at the location shown in Figure 0-2a. The system possessed enough torque and traction to begin pulling itself onto the rail; however, the leading edge of an undercarriage plate intended to guard electrical components, Figure 0-2b, would ram into the edge of the rail, stopping rail climbing. This collision was due to the level of tension within the tracks. With most of the TCR's weight supported by a small section of the tracks, that portion would sag below the level of the protective plate, allowing collision to occur. At times, it was possible to clear this edge; however, the rail would then rest against this plate. The traction at the tracks decreased as the plate supported a portion of the TCR's weight. This led to track slippage, which further hindered rail climbing. Despite these issues, the system eventually climbed into the track bed during this test. When attempting to climb out, the same issues occurred; however, they were compounded by the fact that the tracks were causing the ballast to slip. Rail climbing is a high-torque maneuver, and the ballast was breaking away under the forces causing a further loss of traction. These conditions led to the TCR being unable to climb out of the track bed during the initial tests.

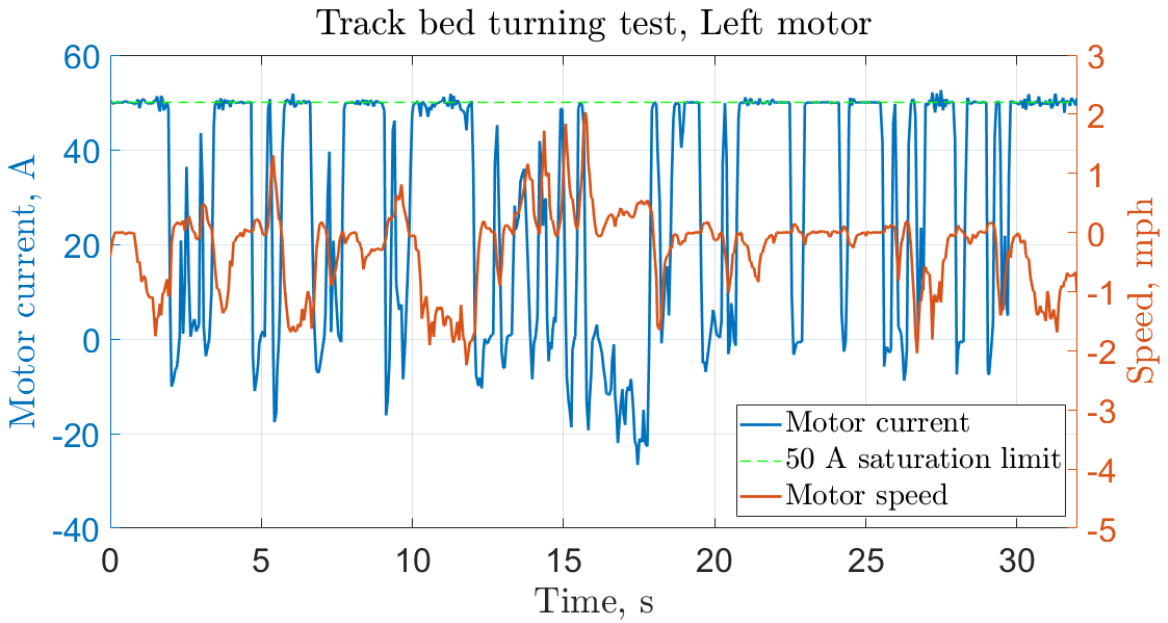

Figure 0-3: Overlaid current and speed data from the left motor during the initial track bed turning test

The turning portion of this test demonstrated that the TCR was able to complete a turn within the track bed; however, the turn was neither neutral nor pivot steer. The TCR had to be continuously shifted forward and backward to gain traction and avoid stalling. At times, the ballast would slip, causing a track to spin in place. Alternatively, at times, traction was sufficient, but the motors did not possess enough power to turn the TCR. As a result, the turn was a combination of many small turns, and the single maneuver took longer than 30 seconds to complete. The left motor data is presented in Figure 0-3. This graph shows that the motor current is consistently limited by the 50 A Max Current parameter discussed earlier, indicating that the system wants to draw more current to complete the maneuver but is limited. This fact is most evident during portions of the test where the current is saturated while the motor speed remains at or around zero. Although successful, this test highlighted a few key issues with turning. The maneuver is inconsistent and time-consuming. It was decided that work should be conducted to improve the system's ability to conduct this maneuver. These tests concluded that work would need to be completed to improve the TCR's ability to complete both rail climbing and turning maneuvers.

1.33. Improvement to Idler Sprocket Assembly

The initial assessment revealed that the original location of the bearings and housings located these components in positions where impacts with the ballast may occur, Figure 0-4. The impacts had plastically deformed a few of the bearing housings and posed a general threat to the TCR's reliability. Replacing these components would only delay their rapid degradation during operation; a more robust solution was needed.

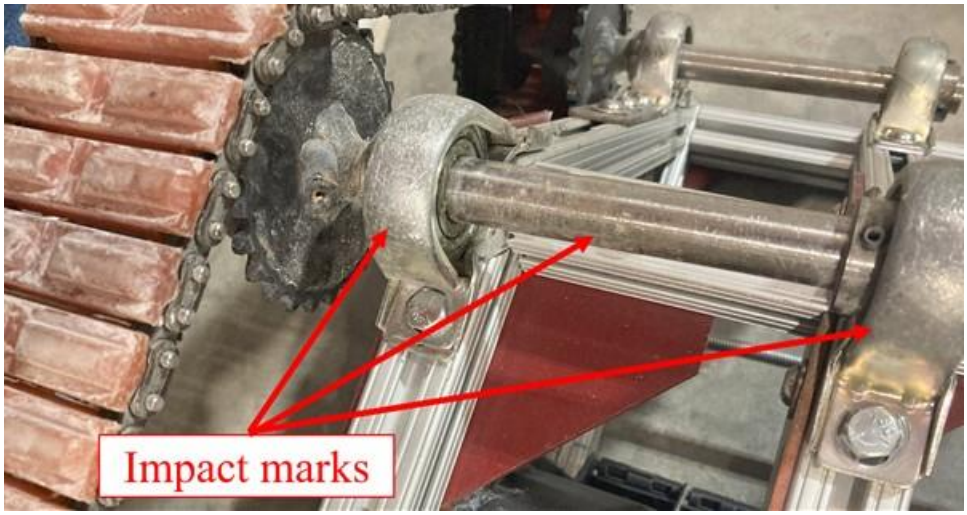

Figure 0-4: Original idler sprocket assembly showing evidence of impacts

Idler sprockets were deemed a potential option to relocate vulnerable components from the TCR's undercarriage. Idler sprockets refer to sprockets with integrated bearings, allowing them to spin freely on a fixed shaft. This component was favorable because housing the bearings within the sprockets would effectively shield the bearings from most impacts. A concept was created utilizing these components, Figure 0-5. The same 0.625 in. diameter 1566 steel shafts from the previous design, Table 0-1, were used as they had been proven to withstand the high forces inherent to operation. Compatible cast iron shaft mounts would be used to clamp onto the shafts, preventing all translational and rotational motion. These mounts would fix the assemblies to the frame rails. 20-tooth ANSI #35 ball-bearing idler sprockets would be placed onto the shaft and located using retaining rings in grooves. The only components exposed to direct impact in this design are the cast iron shaft mounts and a small portion of the fixed axle. All other components are shielded behind the tracks. These solid metal components are much more durable than the exposed bearings and housings in the previous configuration, and any impacts should not degrade the performance of the system. Unfortunately, both sprockets are located on the same side of the mount, creating the possibility for large moment loads. However, this was deemed to be the most beneficial arrangement. Supporting the shaft from between the sprockets and mounting the assembly from that position would relieve much of the loading from the shaft itself, but the loading would still be present within the other pieces of the assembly. Additionally, packaging issues would require the support at the center of the shaft to first travel parallel to the ground to clear the edges of the sprockets before traveling to the frame for mounting. This would create another moment arm, exposing the assembly to failure.

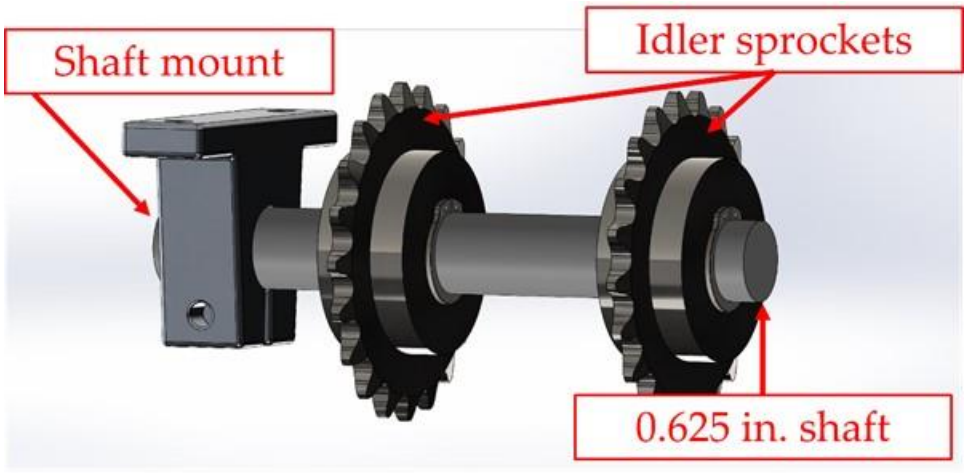

Figure 0-5: Model of the proposed idler sprocket assembly

To investigate the validity of this design, an FEA study was conducted in SolidWorks on the shaft and mount to simulate their response to a significant collision with a tie, Figure 0-6. The shaft and mount were fixed to one another to simulate their condition when clamped together. The mount was constrained with two fixed fixtures applied to the inside of the bolt holes. Roller/bearing fixtures were applied to the surfaces above and below the bolt holes to simulate the clamping supplied by the bolt. Lastly, a bearing fixture was placed on the face of the shaft mount opposite the sprockets to approximate the effect of a plate welded to the back of the mount and bolted to the frame to aid in moment transfer. This plate was later removed from the concept, but its inclusion in this study was deemed insignificant as the main investigation points were the shaft and the mount, not the interface between these components and the frame.

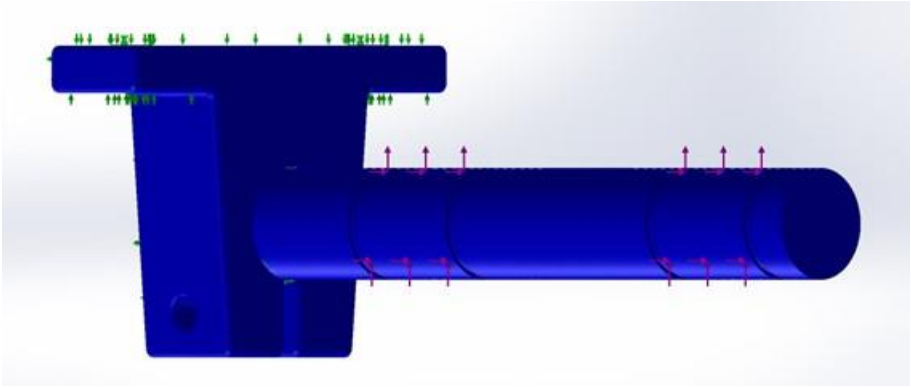

Figure 0-6: Shaft and mount FEA analysis results. Fixtures are shown with green arrows; forces are shown with pink arrows

The forces were applied to the surfaces between the retaining ring grooves where the idler sprockets would be located. The magnitudes of the forces were derived from video footage and chassis-mounted accelerometer data recorded during a large collision with a tie at approximately 5 mph on the Test Bed. The absolute maximum x-direction deceleration during the collision was found to be 2.8 G.

$$F = ma \tag{9-1}$$

Using Newton's second law of motion, Equation (9-1), the force in the x-direction was found to be 290 lb, given the TCR's current weight of 103 lb Next, the z-directional force was found by equating force to the energy imparted into the system over some distance, Equation (9-2), with the distance approximated by the impact time and the nominal velocity.

$$F = \frac{\Delta E}{\Delta d} \approx \frac{mg\Delta y}{V\Delta t} \tag{9-2}$$

From the accelerometer data, the collision length was found to be 0.017 s, and the video footage showed that the center of gravity was raised approximately 2 in. due to the collision. This calculation led to a z-directional force of 137.5 lb, which was tripled to 412.5 lb to approximate the maximal impact force. These resulting forces were then halved to share the collision forces across both axles, leading to −145 lb applied in the x-direction and 206 lb applied in the z-direction. The FEA results were again interpreted using a FOS plot. The part was colored accordingly. FOSs at or below 1 were designated with red, FOSs at or above 5 were designated with blue, and a gradient of colors was used for FOS values in between, as shown in Figure 0-7. Figure 0-6 shows that the shaft is almost entirely blue. The shaft has a minimum FOS of 4.5, indicating a strong ability to endure this load case. The mount, however, has a minimum FOS of 0.74, with a ring of low FOS locations lying at the edge of the interface between the shaft and the mount, Figure 0-7. Yielding at this location will only increase the bearing surface area and should, therefore, remain local, not posing a risk of buckling or heavily deforming the part; hence, the assembly was deemed adequate and was finalized.

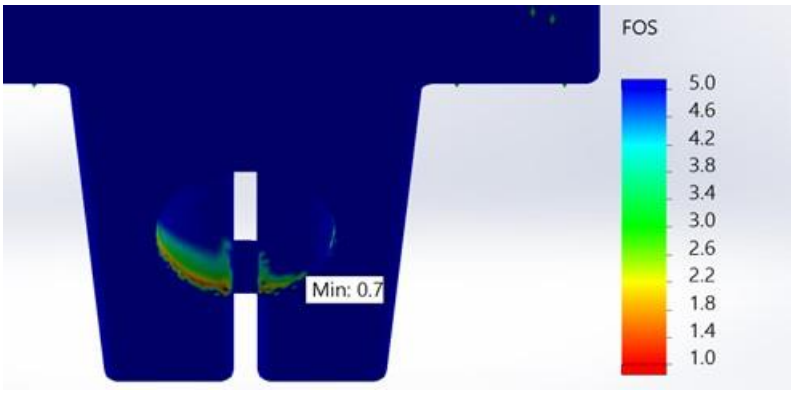

Figure 0-7: FEA results from the shaft mount with the shaft hidden

In hindsight, the configuration of fixtures in this study hid stress concentrations due to moments about the bolted joints, a weakness that would be revealed later; however, this analysis was initially used to validate the design.

The shafts were cut to length and turned on a lathe to create the retaining ring grooves. The sprockets were then installed on the shafts bracketed by retaining rings, and the shafts were fixed in the mounts such that the installed sprockets lined up laterally with the drive sprockets. The assemblies were then fastened to the frame rails using #10−32 bolts and specialty nuts designed to clamp onto the t-slots, Figure 0-8. As can be seen, the only exposed portion of this assembly is

now the end of the shaft and the shaft mount, both highly durable, non-moving components. The critical bearings remain shielded by the tracks. The resulting assembly decreased the total weight of the TCR by over 10 lbs.

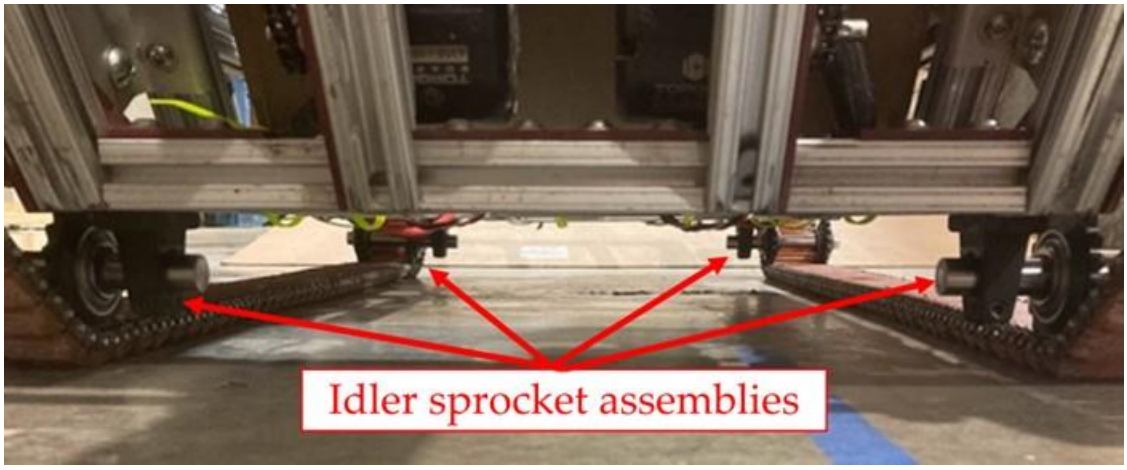

Figure 0-8: Installation of redesigned idler sprocket assemblies

1.33.1. Initial Testing and Axle Mount Failure

The new assemblies were then tested at a set of local tracks. The TCR was placed within the tracks and aligned to be parallel with them. Tests were then conducted at 1, 2, and 3 mph to evaluate the new system's response and overall reliability. These tests revealed that the #10−32 nuts used to secure the assemblies to the frame rails were insufficient. Both nuts of one assembly split in two, decoupling the mount from the frame, Figure *0-9*a. After further investigation, it was found that most of the other nuts had also been deformed. This failure was most likely due to the large stresses resulting from moments about the bolted joints. The bolted joints were not modeled in the FEA study, and this weakness was suppressed by the bearing fixture placed on the rear face of the shaft mount, which was meant to simulate a supporting plate for these moments. However, this plate was never included in the actual design. These large moments were then being resisted only by a set of #10-32 nuts and bolts. The thin walls of the nuts,

Figure *0-9*a, proved to be the weakest link and failed critically. The mounting configuration was modified accordingly in response to this failure. The assembly hardware was upgraded to Grade 8, 1/4-in.−20 bolts,

Figure *0-9*b, which increased the tensile area by over 80% [44]. Additionally, rather than clamping onto the frame's t-slots, through-holes were drilled to clamp across the entire beam, allowing for

more effective moment transfer from the idler sprocket assembly into the frame. Standard hex nuts were used in this configuration, eliminating the first design's thin-wall failure mode.

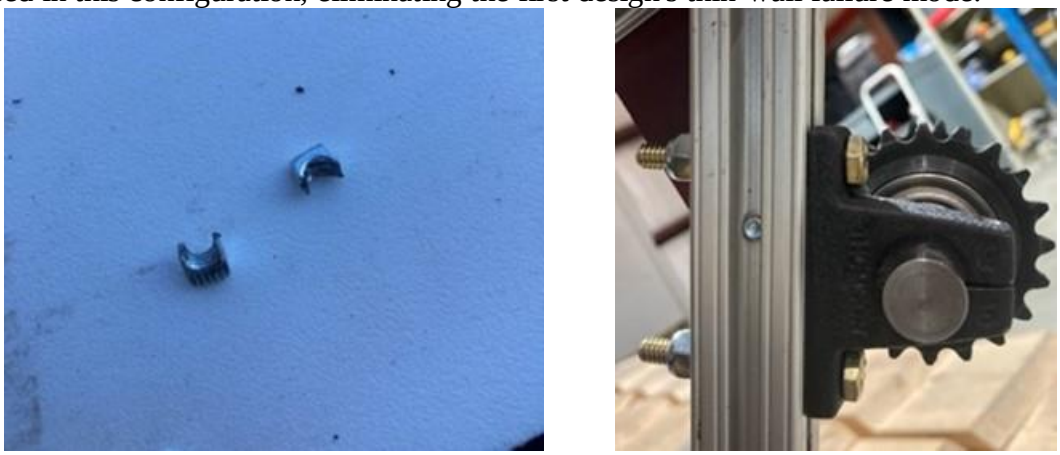

(a) **(b)**

*Fi*gure 0-9: (a) Split #10-32 mounting nuts from the validation test; (b) Improved mounting configuration using 1/4-in.−20 hardware

In addition to the modifications to the idler sprocket mounting assemblies, modifications were made to the operating conditions of the TCR. It was determined that operating at speeds above 2 mph within the track bed may be detrimental to the TCR in its current condition. Collisions with ties and ballast impart large shock loads into the system without any form of suspension. It appears from testing that this loading moves into unacceptable ranges between 2 and 3 mph. At 2 mph within the track bed, collisions with ties may cause the front of the TCR to become slightly airborne,

Figure *0-10*a; however, the motion is not incredibly violent, and control may be maintained throughout. At 3 mph, the front of the TCR is jolted upwards violently,

Figure *0-10*b. This behavior was observed on the Test Bed; however, 3 mph operation was acceptable during these tests, while large collisions were occurring at 4.25 mph. It appears that the actual track bed is slightly rougher than the Test Bed, causing large collisions to occur at lower speeds. It was, therefore, concluded that the TCR's operation should be limited to 2 mph within the track bed until further modifications or testing demonstrate its ability to operate above this threshold reliably and controllably.

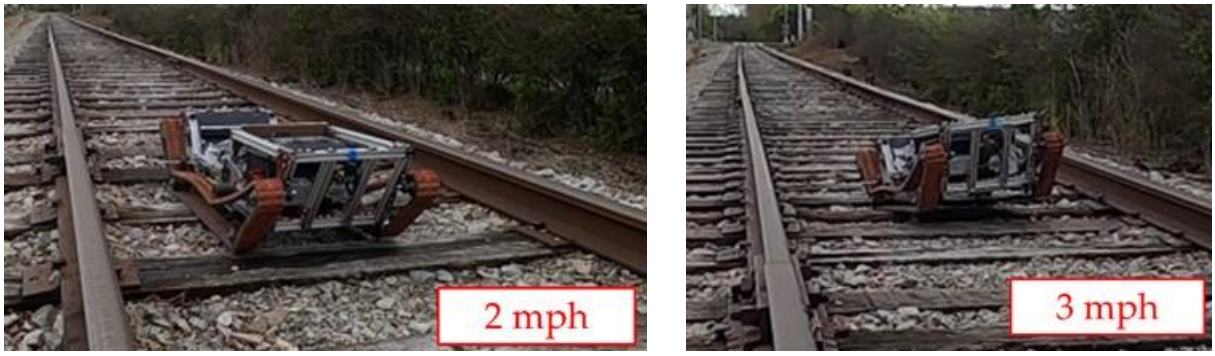

(a) **(b)**

Figure 0-10: Images of the TCR colliding with the edge of a tie within the track bed at (a) 2 mph and (b) 3 mph

The TCR was again tested at 1 and 2 mph at a local set of railroad tracks. These tests were operated across a 75 ft. stretch, with each speed being tested twice, once in each direction. After these tests, the idler sprocket assemblies were inspected, and no signs of damage were found. The assemblies were then determined to be acceptable for the current operating conditions of the TCR.

1.34. Rail Climbing and Turning Improvements

The initial assessment highlighted that rail climbing was either intermittent or impossible depending on the TCR's operating conditions. Additionally, turning was possible, but there was an opportunity to improve its consistency and efficiency. As shown, the TCR possessed the power to pull itself over the rail; however, issues arose with track tension, interference from the undercarriage protective plate, and traction. Figure 0-11 shows a test conducted on a section of indoor 136 lb/yd rail. The TCR was placed on the ties, as no ballast is present at these tracks. Although the leading edge of the protective plate cleared the railhead during this test, the plate now rested on the top of the rail. The plate then removes load from the tracks, reducing traction.

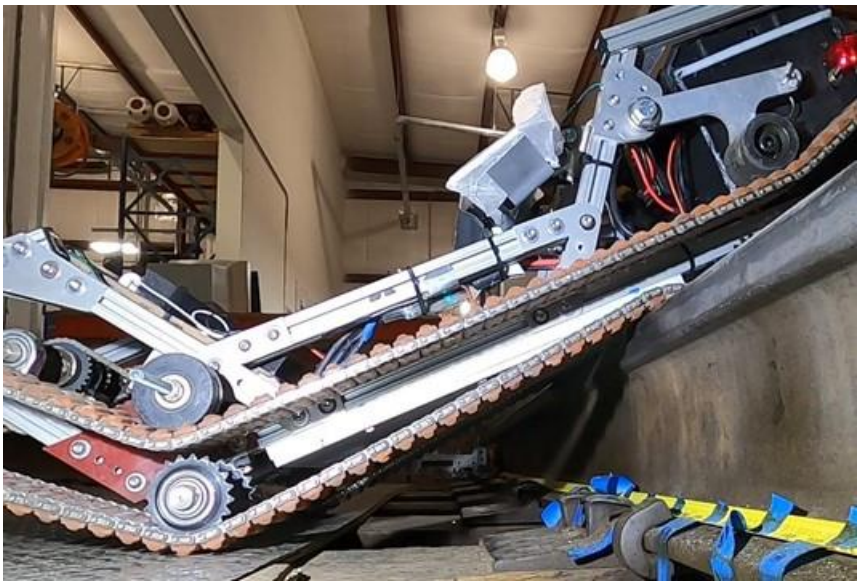

Figure 0-11: Indoor rail climbing test illustrating how the undercarriage plate removes traction from the tracks

Therefore, modifying the TCR to consistently rail climb was dependent on two parameters. Firstly, modifications were necessary to ensure that the leading edge of the protective plate could never contact the rail head. If this collision occurs, the current attempt at rail climbing will almost certainly fail. Secondly, modifications were necessary to ensure that the protective plate was not able to bear a significant portion of the TCR's weight as it passed over the railhead, thereby reducing traction. If these two parameters were met, the TCR should be consistently capable of pulling itself over a rail. Three modifications were enacted to aid in meeting these parameters: (1) an additional idler sprocket assembly was installed on the undercarriage, (2) the track tension was increased, and (3) the height of the undercarriage protective plate was reduced. The idler sprocket assembly would serve to eliminate the chance of collision between the leading edge of the protective plate and the railhead. Wherever an idler assembly is placed, the track must travel over the sprocket, fixing the track's height at this location. If installed correctly it could ensure that the tracks would never drop below the height of the protective plate when approaching the rail, eliminating the chance of a collision. Additionally, it could also aid in preventing the track from resting on the protective plate, depending on its location.

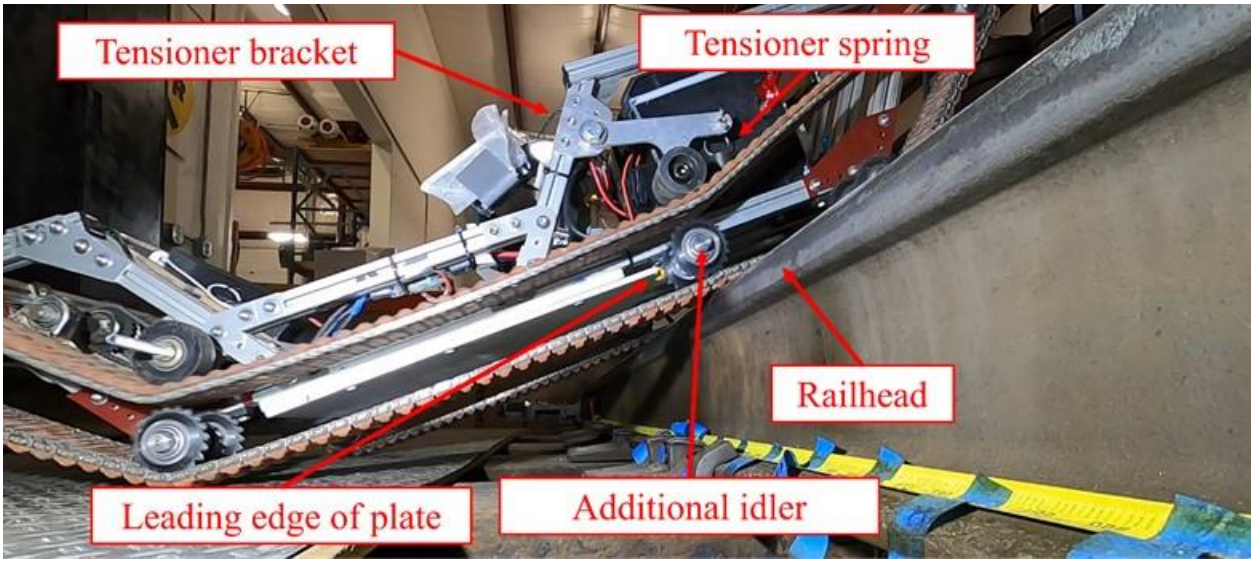

Figure 0-12: Rail climbing test with an additional undercarriage idler, illustrating its ability to eliminate collisions between the leading edge of the protective plate and the railhead

Figure *0-12* illustrates how the additional undercarriage idler eliminates the possibility of the leading edge of the protective plate to contact the railhead in this configuration. Also illustrated is the location of the tensioner for this test. The tensioner bracket is mounted to the forward angled frame member. This bracket may be relocated elsewhere on this frame member when loosened. The tensioner spring is labeled in the figure. This spring connects the tensioner bracket to the lower longitudinal frame member. Increasing the tension on the tracks will reduce the amount of sag when under load. Decreasing the sag will aid in avoiding contact with the surface of the undercarriage plate. The tension may be increased by lowering the location of the tensioner bracket. As this occurs, the bracket pivots counterclockwise around the roller, which contacts the tracks. This rotation causes the mounting location for the spring to rise, stretching it further. As the spring is stretched further, the tension applied increases.

Lastly, the height of the undercarriage protective plate was decreased. Initially, this plate was mounted on top of 0.625 in. high spacers,
Figure *0-13*a. These spacers allowed wires to travel beneath the frame while being protected by the plate. The protective plate was removed, and any wires traveling beneath the undercarriage were rerouted elsewhere,

Figure *0-13*b. The spacers were removed, and the protective plate was bolted in place. This modification increased the TCR's ground clearance by 0.625 in., further limiting the amount of contact possible between the plate and the railhead.

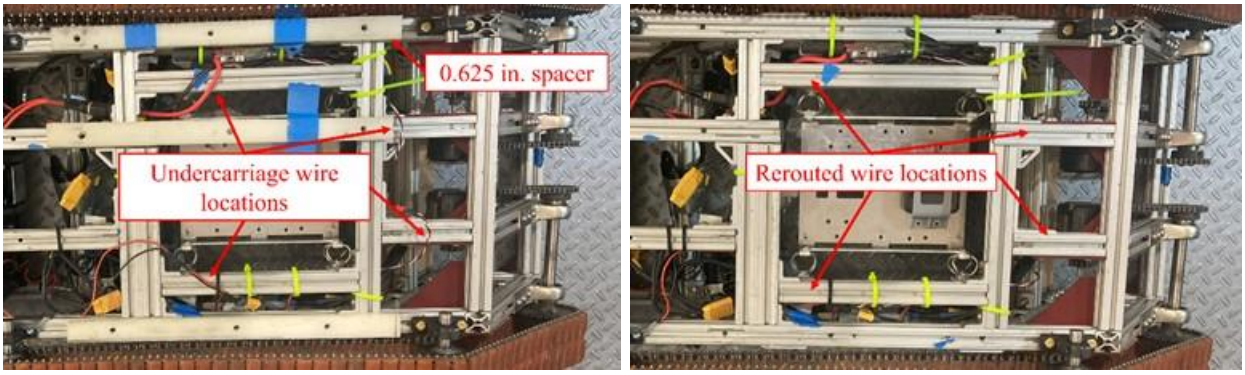

(a) **(b)**

Figure 0-13: TCR undercarriage (a) before and (b) after rerouting wires to enable the protective plate spacers to be removed

A test was then conducted to evaluate the ability of the modified system to climb in and out of a track bed. The test was conducted on a set of local tracks using 115 lb/yd rail. The test involved placing the TCR trackside perpendicular to the rails. Rail climbing into the track bed was then attempted, followed by a 180° turn and an attempt to climb out of the track bed. The turning portion of this test will be discussed later in this section. The TCR was controlled manually throughout this test, and video footage was taken for later analysis.

(a) **(b)**

Figure 0-14: Images from the rail climbing test of the improved system: (a) TCR tipping into the track bed while climbing in, (b) TCR becomes stuck on a tie while attempting to climb out

The results from the rail climbing test of the modified system display a greatly improved ability to conduct rail climbing. The TCR was able to climb into the track bed without issue, Figure *0-14*a. This maneuver involved climbing the ballast slope next to the tracks while attempting to climb the rail. These operating conditions are more difficult than may be expected in a typical railyard, where the tracks are likely to be at ground level. Completing the maneuver in these conditions demonstrates an ability to operate successfully in a more difficult scenario than expected. The improved system was also able to climb back out of the track bed. However, during

a similar test conducted without the presence of the additional idlers, both tracks ended up on portions of the ballast when attempting to climb out,

Figure *0-14*b. Due to the high-torque nature of this maneuver, the ballast began to break away, causing the tracks to slide. As the ballast was pushed away, the TCR eventually came to rest on the tie between its tracks. The level of the ballast was decreased to the point where the tracks no longer had meaningful traction, and the TCR was completely stuck on this tie. The TCR had to be manually moved before this test was continued. Although only occurring during the test without the presence of an additional idler, this behavior is noted here as it does not appear to be dependent upon the presence of the additional idlers. During the test with the improved system, both tracks were located on ties as the TCR climbed out of the track bed. During the test without additional idlers, both tracks were located on the ballast, allowing the mentioned failure mode to occur. Therefore, it may be prudent to only attempt climbing out of the track bed once at least one of the tracks is located on a tie. The tracks on which these tests were conducted are mostly out of use and do not experience regular maintenance. Testing the TCR on revenue service track is required to determine whether the ballast in those conditions retains enough cohesion to complete this maneuver. Lastly, as these tracks use 115 lb/yd rail, which is shorter than the standard 136 lb/yd rail, the TCR must also be retested to validate its performance under these conditions. The final validation will be covered in a later section.

It was hypothesized that the additional idler assembly may also help with turning within the track bed. Much of the resistance to turning a tracked vehicle is due to tracks slipping and sliding perpendicularly to their direction of travel for turning to occur. The large grip (traction) that is needed for moving the tracks forward mandates large forces when they are commanded to slide sideways or perpendicular to their longitudinal axis (direction of forward motion). The additional idler assembly essentially splits the undercarriage portion of the track into two smaller sections. With the rough terrain of the track bed, it is possible that one set of sprockets on either end of the TCR will lose contact with the ground. In this case, the undercarriage section of the tracks becomes the portion between the additional idler sprocket and the other sprocket that has remained on the ground. Turning this smaller section of the tracks will require less force as there is less length of track to slide. Therefore, the modifications meant to improve rail climbing may also improve turning. To evaluate this hypothesis, the 180° turn conducted for the rail climbing test was compared to an identical 180° turn conducted at the same location with the additional idler assembly removed. Real-time data was recorded from both ESCs during each test. The resulting data was then analyzed to gather any available conclusions.

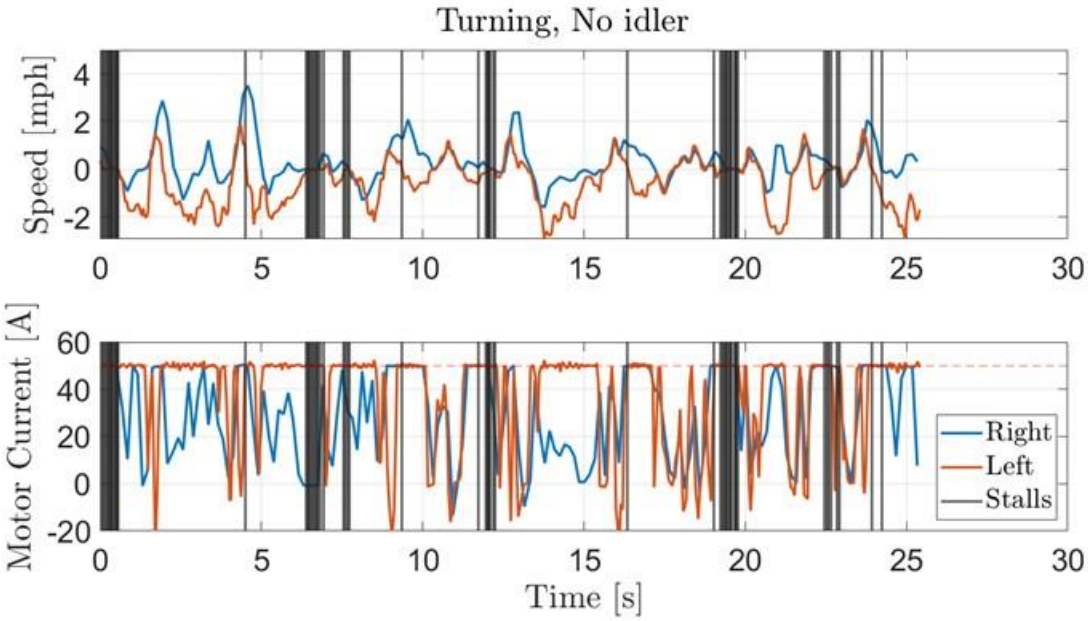

(a)

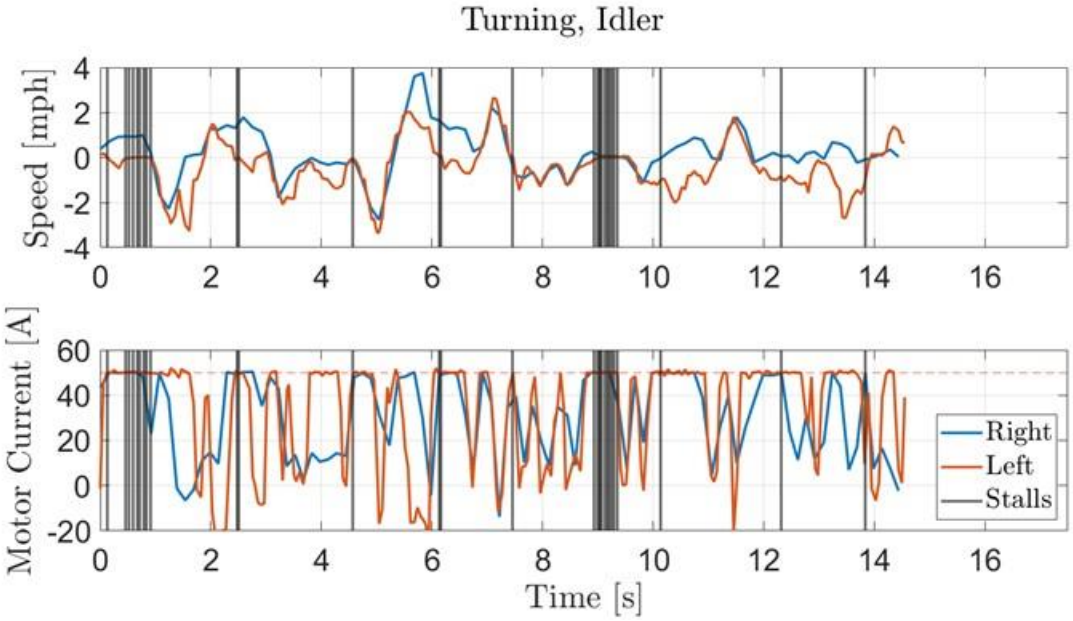

(b)

Figure 0-15: Real-time motor current and speed data from both motors during the turning tests with (a) no additional idlers and (b) additional idlers. Stalls are highlighted with black lines

The real-time data from the two tests,

Figure *0-15*, revealed a few key takeaways. At first glance, the turn conducted with the additional idlers took around 15 s., whereas the turn without the additional idler took around 25 s. Therefore, adding the idlers resulted in a 40% reduction in the time taken to conduct the maneuver. After conducting each test, it was hypothesized that the no-idler test experienced more stalls than the

idler test. To evaluate this, stalls were marked on each plot. A stall was defined as any moment when a motor's current was at or above 49 A while the motor's absolute speed was at or below 0.1 mph. This subset would encompass moments when the motor was working at full capacity while not moving at all. Visually, it is observed that the no-idler test contains nearly double the instances of extended stalls lasting more than a few data points. The combination of these metrics shows that the inclusion of the idlers can be correlated to reduced time and reduced stalling while conducting a turn within a track bed. It was concluded that the inclusion of the assembly aided in the consistency and efficiency of this maneuver. However, 15 seconds is a significant period to conduct a single turn, and further improvements could be made. Lastly, as the tracks on which the tests were performed were largely unmaintained, observing the TCR's performance on revenue service track may reveal additional results.

Chapter 10
Safety Improvements

Beyond ensuring the mechanical and operational safety of the TCR that was discussed in the earlier chapters, this chapter discusses the safety improvements to the electrical system. The improvements discussed here are mainly targeted toward ensuring that the batteries do not over drain in case the electrical system is inadvertently left on.

1.35. Assessment of Initial Design

Several safety improvements were made during the study. The first safety improvement is related to the original 100 A circuit breaker, which regulates the entire circuit of the TCR. During a round of shakedown tests at a set of local tracks, the TCR would suddenly lose all power and stop repeatedly. After each of these instances, it was found that the circuit breaker had been triggered. It was assumed that the circuit breaker had been triggered by a surge of current due to the operating conditions. The track bed is quite rough, and it was hypothesized that the collisions with ties might cause a current spike as the PID control system attempted to counteract this rapid deceleration.

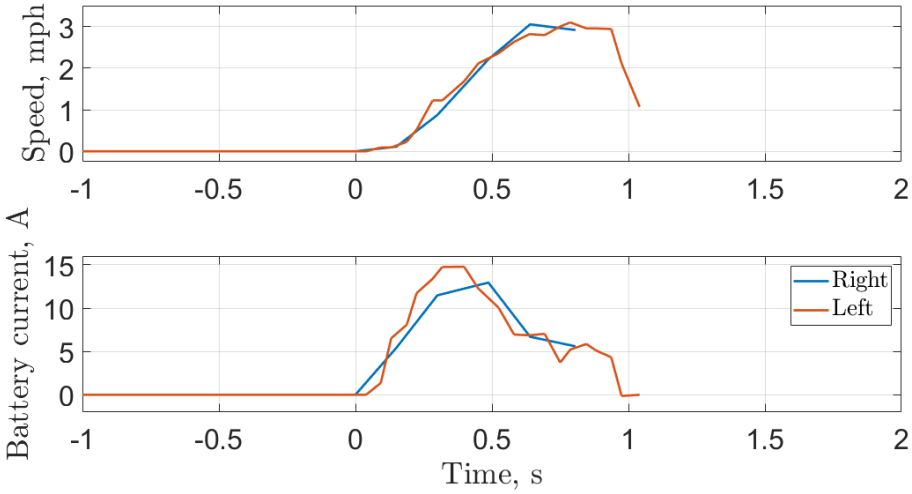

Figure 0-1: Speed and battery current data from both motors capturing the moment the circuit breaker tripped during a 3-mph test within the track bed

To investigate these incidents, both motors' speed and battery current data were analyzed from an event in which the circuit breaker tripped almost immediately after beginning a 3-mph test (Figure *0-1*). The TCR struck the edge of a tie shortly after the test began and then lost power. The data shows that the TCR reached the 3-mph testing speed within a second. After this point, no more data from the right ESC is available; however, the left records for another quarter second. The data from the left ESC shows the moment of contact with the edge of the tie just before the 1 s. mark. A steep decline in speed marks this collision. The battery current drawn by the left motor, however, decreases during this collision, and no current spike is visible, as hypothesized. As was discussed in the Operational Control Improvements chapter, current spikes may occur quickly enough not to be recorded; however, it can be seen that, at maximum, each motor is drawing less

than 15 A from the battery, and at the moment when the circuit seemingly loses power, the left motor is drawing 0 A. The data does not support the hypothesis that the collision is causing a large spike in battery current, which would need to reach above 100 A across both motors to trip the circuit breaker. Another hypothesis was formed to explain the tripping of the breaker. It was realized that the circuit breaker is located on the forward wall of the electrical box. The battery occupies most of the box and may move slightly in one direction or another during operation. It was hypothesized that during rapid deceleration, the battery would list forward and trigger the manual reset button on the circuit breaker, which faced the battery and was exposed, Figure 0-2. This behavior would explain why the circuit breaker triggered when the TCR struck the edge of a tie and why large currents were not associated with the incident. Testing within the lab found that this hypothesis was correct. With the TCR powered, a lab member quickly pulled it backwards with the lighting system powered. The lighting system flickered during the pull but did not power off afterward.

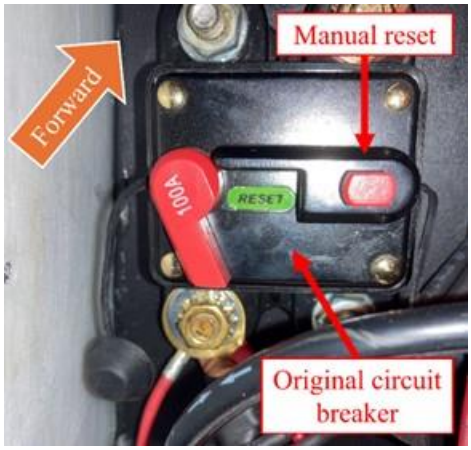

Figure 0-2: Original 100 A circuit breaker mounted to the forward wall of the electrical box. The arm is open, although the circuit is closed

It was thought that the lights were flickering because the manual reset button was partially depressed before returning to its original position; however, after this test, an investigation of the circuit breaker showed that it had been triggered. Figure 0-2 shows the original circuit breaker mounted to the forward wall of the electrical box. The figure shows the circuit breaker with the circuit closed; however, the arm is not covering the green "RESET" marker as it should. The arm instead is resting in the location where the arm should travel once the circuit breaker has been triggered. Once this circuit breaker was triggered, the arm rotated even farther clockwise. Upon investigation, it was found that this motion initially opens the circuit; however, if the arm is allowed to move even further clockwise, the circuit will close again. This behavior is what occurred during the test where the lights flickered. The circuit breaker was manually triggered by the battery contacting the manual reset button; however, the arm was allowed to swing far enough clockwise that the circuit closed once again due to some malfunction within the circuit breaker. This malfunction posed a large safety risk to the project. If the circuit breaker was triggered due to a short circuit, there was a chance that the circuit could close once again. It was determined that the circuit breaker must be replaced immediately. The new system must also be redesigned such that the battery may not trigger it during rapid deceleration.

The other safety concern that arose was also related to the system's electrics. One of the TCR's batteries was mistakenly left connected to the system for a few days. When inspected, it was found that the battery cells were at voltages as low as 1.4 V. The LiFePO4 cells used within the battery are designed for usage between 2.5 – 3.65 V. At 1.4 V, the battery cells were considered deeply discharged to the point where battery damage may have occurred. The damage may have included capacity loss, increased internal resistance, and the formation of lithium dendrites [69]. Lithium dendrites are metallic structures that form on the negative side of a battery. These dendrites may grow to the point where they puncture the divider between the positive and negative sides of the battery, causing an internal short circuit, which could have devastating effects [70]. Due to this risk, it was determined that the battery should be retired, and a system should be put in place to ensure that this failure does not happen again.

1.36. Replacement of Faulty Circuit Breaker

As discussed, the original circuit breaker was inadequate because the battery could manually trigger it during rapid deceleration and could close the circuit after it was triggered. A design using an automatic reset circuit breaker was proposed to replace this system. Unlike the original circuit breaker, automatic reset circuit breakers do not possess an external switch and arm for manually resetting the circuit. Instead, the circuit breaker operates using thermally deformable contacts. As the current increases, the temperature of the electrical contacts will increase, causing thermal deformation. The breaker is designed so that at the maximum current, the contacts deform to the point where electrical contact is broken, opening the circuit. Once the current has stopped flowing, the contacts begin to cool, slowly returning to their original shape. The contacts will restore electrical contact after a short period of cooling, creating a system that automatically resets.

Figure 0-3: Installation of the auto-reset circuit breaker

An automatic reset circuit breaker with a maximum current of 100 A was purchased to implement this design. The circuit breaker was again connected immediately downstream of the battery's positive lead, ensuring that it would regulate any current passing through the circuit. During later

operations in the track bed, no further events of the circuit breaker malfunctions have been observed.

1.37. Installation of Battery Management System

To prevent the cells from discharging beyond their working voltage range, a battery management system (BMS) was installed. The inclusion of a BMS is standard for batteries of the size used in this project. A BMS is installed between the battery's negative lead and the rest of the circuit, ensuring all current passes through it, much like the breaker. A well-designed BMS will serve several important functions to ensure the safety of the battery. The BMS will read the voltages from each cell within the pack. The BMS will open the entire circuit if a cell deviates from its acceptable range. Additionally, the BMS is capable of balancing cells within a pack. Balancing refers to ensuring that all cells within a pack operate at the same voltage, and the BMS will internally transfer energy within the battery pack to maintain this balance. Other features include a maximum current setting and maximum operating temperature monitored by thermocouples. A BMS compatible with the TCR battery pack was chosen. The BMS is capable of 200 A of continuous current and a peak of 350 A, much higher than the TCR requires.

The BMS was installed against an inside wall of the electrical box. The circuit was modified such that the BMS would lie between the negative terminal of the battery and the rest of the circuit. A connector between the BMS balance port and the battery's balance leads was spliced together to allow simple connection and disconnection. The negative wire from the main battery connector was connected directly to the corresponding port on the BMS, and a jumper wire connected the BMS to the main negative terminal from the TCR's components. To power on the BMS, a 9 V battery is jumped across its two leads. A 9 V battery was connected to a button and was placed in series with a small resistor to avoid sparking. A short press of the button will result in the system powering on when the battery is connected.

Table 0-1: BMS Parameters Regarding Cell Voltages

Cell over-voltage protection	3.65 V
Cell over-voltage protection resume	3.55 V
Cell under-voltage protection resume	2.65 V
Cell under-voltage protection	2.60 V
Power-off voltage	2.50 V

When the battery type of LiFePO4 was inputted into the system, the governing parameters were automatically populated, as shown in Table 0-1. The under and over-voltage protection parameters range from 2.6 – 3.65 V. These values define the maximum operating range of the TCR. Any values outside of this range will prompt the BMS to open the circuit. The under and over-voltage protection resume parameters range from 2.65 – 3.55 V. After opening the circuit due to out-of-range cells, the BMS will only reclose the circuit once the cell voltages all fall within this smaller range. Finally, the power-off voltage is set to 2.5 V. After disconnecting the circuit for under-voltage cells, the BMS continues to monitor the circuit. The BMS will draw a very small amount of current, and this current draw may continue to drain the under-voltage cells. Once a cell reaches 2.5 V, the BMS will power itself off in a final effort to prevent the cells from reaching dangerously low voltage levels. After the successful installation of the BMS, no other issues were observed

with the battery. Together, the circuit breaker and BMS modifications have greatly increased the safety of the electrical system and the TCR.

Chapter 11
Final Field-Testing Results

Earlier sections detailed the process of implementing various modifications to the TCR to improve its ability to perform undercarriage inspections of railcars. They presented intermediate results that informed engineering and implementing improvements, which were tested in a controlled environment in the laboratory and to a limited extent on tracks. This chapter will provide the results of field testing under a stationary railcar at the Virginia Museum of Transportation in Roanoke, Virginia as well as a mobility test on a stretch of revenue service track. First, the test setup will be introduced, followed by the test details and analysis of the results.

1.38. Test Setup

This section describes the final test setup used to fully validate each system for real-world inspections of railcar undercarriages.

1.38.1. Image Quality and Lighting

Although the processes for improving the image quality and lighting systems were distinct, it is impossible to separate the results from one another; therefore, the two systems' testing and results were combined in this final evaluation. The tests were conducted beneath two railcars resting on a set of tracks. The TCR was centered within the tracks, and a step input of 2 mph was applied throughout the test. 2 mph was previously defined as the maximum operating speed of the TCR. Traveling at the maximum speed would provide the most difficult scenario for reducing motion blur. The three onboard GoPro® cameras captured images throughout each test. Three tests were conducted utilizing shutter speeds of 1/480, 1/960, and 1/1920 s., respectively. Varying the shutter speeds would determine at which point motion blur would become noticeable in this real-world environment. As noted, the lighting within the images is directly coupled to the shutter speed, affecting the resulting image quality.

The tests were then carried out, traversing beneath a boxcar and a hopper car, Figure 0-1. The images from each test were then analyzed for adequate clarity and contrast.

Figure 0-1: The TCR at the testing site, shown beneath the hopper railcar

1.38.2. Field of View

The images from the above-introduced image quality and lighting tests were then used to validate the imaging system's FOV. Portions of the test where the TCR traversed beneath low-lying components were extracted. These portions include rail axles and hopper gates, Figure 0-1. To validate the field of view, the side-view images must overlap with the vertical camera's view. Additionally, the side-view images must capture the outer edge of the undercarriage. The images were analyzed to investigate their ability to meet these conditions in each case.

1.38.3. Control

The control system was evaluated during a railcar undercarriage inspection. First, the performance of the PID control system was evaluated. Tests were conducted beneath the railcars at 1 and 2 mph. During these tests, real-time motor data was recorded from each ESC via Bluetooth. The data was analyzed to evaluate the system's step response at the onset of the test and the control system's ability to maintain a desired speed throughout the steady-state portion of the test.

In addition, the FPV system was evaluated. Throughout the 1 and 2 mph tests beneath the railcars, the FPV system was utilized to supply the operator with feedback regarding the TCR's position and heading within the track bed. Additionally, the TCR was not in view for much of the test as it passed beneath the bogies, leaving the FPV system as the only means for control feedback. These tests qualitatively evaluated the ability of the FPV system to be used in the real-world inspection environment. The results of the tests would inform whether the lighting, vibrations, or disturbances inherent to the environment would combine to make control via this method unattainable. The video footage from the FPV camera was recorded for later analysis.

1.38.4. Mobility and Reliability

A test was conducted on a set of revenue service tracks to assess the TCR's ability to conduct the maneuvers necessary for undercarriage inspections. Previous mobility tests were not conducted on

revenue service tracks and were instead on unmaintained or out-of-service tracks. Testing on revenue service tracks presents the challenge of scaling a larger rail; however, the ballast may also be in better condition, which would aid in maneuvering. Before the test, the TCR was placed trackside and aligned perpendicularly to the rails. The TCR was then manually operated to complete the test. The TCR climbed over the rails, completed a 180° turn within the track bed, and climbed out of the track. Video footage was recorded of the test for later analysis, and the real-time data from each ESC was recorded via Bluetooth.

Mobility was also evaluated by measuring the TCR's effective range. The current drawn from the battery and the distance traveled by the TCR could be used to compute the TCR's effective range at given operating speeds. These ranges could then be compared to the expected length of trains to determine whether the current system could feasibly conduct a full-scale undercarriage inspection of a train without the battery losing charge mid-test. The data gathered from both ESCs during the undercarriage inspection tests beneath a set of railcars were used. Battery current and motor speed data were measured from each ESC. Additionally, the current drawn from the lighting system was evaluated using the BMS. The BMS can read the current being drawn through it. The lighting system was powered while all other components were disconnected, and the current reading was gathered from the app interface to determine the additional current draw due to the lighting system. From this collection of data, the TCR's range on a single battery charge may be estimated for traversing the track bed at 1 and 2 mph.

Reliability was not directly tested in a way that could garner results; however, throughout the course of the above-mentioned tests the TCR would travel consistently at its maximum operating speed of 2 mph and perform all necessary maneuvers for real-world inspections. The system's condition after completing these tests could then be evaluated to determine if any failures had occurred which could inform the state of the TCR's reliability.

1.39. Results

The results of the above-mentioned tests will now be presented and analyzed as they pertain to the ability of the TCR's individual systems to complete real-world undercarriage inspections.

1.39.1. Image Quality and Lighting

(a)

(b) **(c)**

Figure 0-2: Retaining clip on a railcar undercarriage captured at 2 mph using a shutter speed of (a) 1/1920 s., (b) 1/960 s., and (c) 1/480 s.

Figure *0-2* compares images of retaining clips captured during a 2-mph inspection beneath a railcar while imaging at various shutter speeds. Each image displays adequate lighting. The retaining clip is quite close to the track bed, making lighting less of a concern compared to motion blur. The 1/1920 s. (

Figure *0-2*a) and 1/960 s. (

Figure *0-2*b) tests both capture the retaining clip sharply and without visible blur. The 1/480 s. test (

Figure *0-2*c), however, demonstrates a small amount of blur, which is evident around the edges of the retaining clip. Being close to the track bed, this imaging target presents one of the most challenging scenarios for rejecting motion blur during an undercarriage inspection. From these results, it can be determined that both 1/1920 and 1/960 s. shutter speeds are sufficient for motion blur rejection, given the TCR's maximum operating speed of 2 mph. The blur in the 1/480 s. case is not significant, however, and its ability to gather more light than the other cases may be an acceptable tradeoff for this small amount of blur.

(a)

(b)

(c)

Figure 0-3: Rail axle and wheel captured at 2 mph using a shutter speed of (a) 1/1920 s., (b) 1/960 s., and (c) 1/480 s.

Figure 0-3 presents images of a rail axle and wheel from the 2-mph tests captured at each shutter speed. In this case, the imaging targets are much farther away relative to the retaining clip observed previously. Motion blur will be less of a concern when capturing such imaging targets as the relative motion will be much less. The driving concern with these images is the lighting. Visually, it appears that each of these images possesses adequate lighting to capture the scene. It appears that the images may become slightly brighter as the shutter speed decreases, which is to be expected.

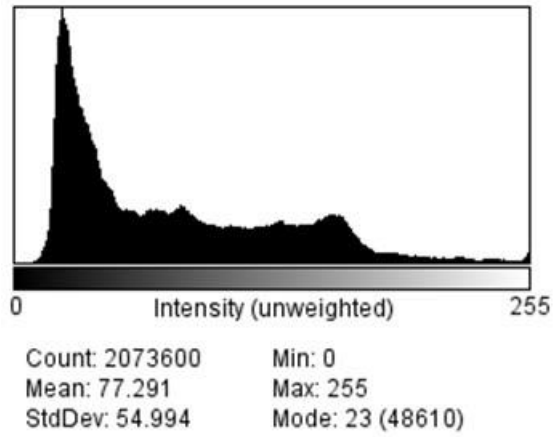

(a)

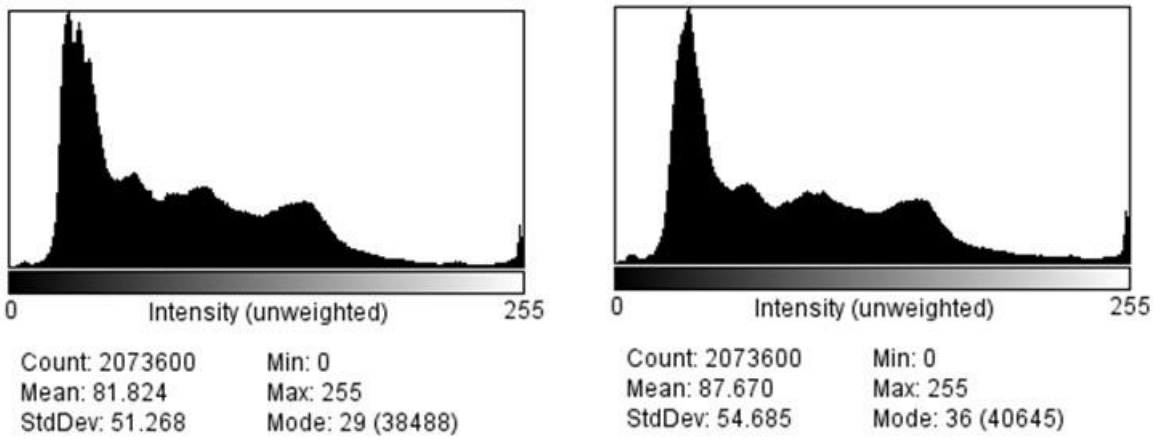

(b) **(c)**

Figure 0-4: Pixel intensity histograms of the rail axle and wheel images using a shutter speed of (a) 1/1920 s., (b) 1/960 s., and (c) 1/480 s.

Figure 0-4 presents the pixel intensity histogram from each rail axle and wheel image. A close inspection shows that the intensity distribution for each image is very similar. The mean values of each histogram indicate that the images do, in fact, grow brighter as the shutter speed decreases, but the effect is not drastic, ranging from 77-88. Additionally, the 1/1920 s. case (Figure 0-4a) appears to lack detail in the plateau located near the center of the sensor's range. The 1/960 s. (Figure 0-4b) and 1/480 s. (Figure 0-4c) cases share similar peaks and valleys in this region, whereas the 1/1920 s. case appears to not capture this intensity range with as fine of resolution. Interestingly, the contrast (represented by standard deviation) remains nearly constant across the set of images, between 50-55. This statistic suggests that each image contains a roughly equal amount of information. This statistic was unexpected. The 1/480 s. case gathers 4 times the light of the 1/1920 s. case. It would be expected that this increase in exposure would allow for greater information to be gathered. Investigating the images closely reveals the reason.

(a)

(b) **(c)**

Figure 0-5: Zoomed-in photo from the label of the rail wheel captured at shutter speeds of (a) 1/1920 s., (b) 1/960 s., and (c) 1/480 s.

Close-up images of the label on the rail wheel, Figure 0-5, demonstrate that the shutter speed is, in fact, altering the amount of information captured within the image. The 1/1920 s. case (Figure 0-5a) clearly exhibits a level of blur not seen in the 1/960 s. (Figure 0-5b) or 1/480 s. (Figure 0-5) cases. This blur is not due to motion as the 1/1920 s. shutter speed is the most robust to motion across the three. Most likely, this blur is due to noise from the imaging sensor. It is present in this case due to the decrease in light gathered by the 1/1920 s. case. The camera increases the sensor sensitivity to properly expose the images at this light level, leading to the similar pixel intensity histograms seen in Figure 0-4. However, this increase in sensitivity comes at the cost of an increase in noise. This noise obscures the fine details within the image. Interestingly, it appears that there is not a large distinction between the 1/960 s. and 1/480 s. cases in terms of this noise.
These results concluded that imaging with a shutter speed of 1/960 s. would be the most beneficial option. Using this setting, the imaging system consistently captures the railcar undercarriages with sufficient clarity and contrast. The shutter speed is quick enough to capture close-up objects without noticeable motion blur, and enough light is still gathered to retain detail when the imaging target is farther from the lens. These results validated the image quality and lighting systems for undercarriage railcar inspections.

Alternatively, the 1/1920 s. shutter speed could be used while utilizing image processing software to improve the image quality. It is possible that image processing software could help remove much of the noise within the image, resulting in a clearer view of the undercarriage. If this is the case, 1/1920 s. may become the most beneficial option as it could eliminate motion blur at higher operating speeds than 1/960 s. This point could be investigated in future work, as another consideration is the added processing time that this method would add.

1.39.2. Field of View

The FOV of the imaging system was validated in two scenarios: (1) low-lying bogie components and (2) hopper gates. These two scenarios represent imaging targets where low-lying components stretch laterally across the railcar's undercarriage and will require the widest FOV to fully capture.

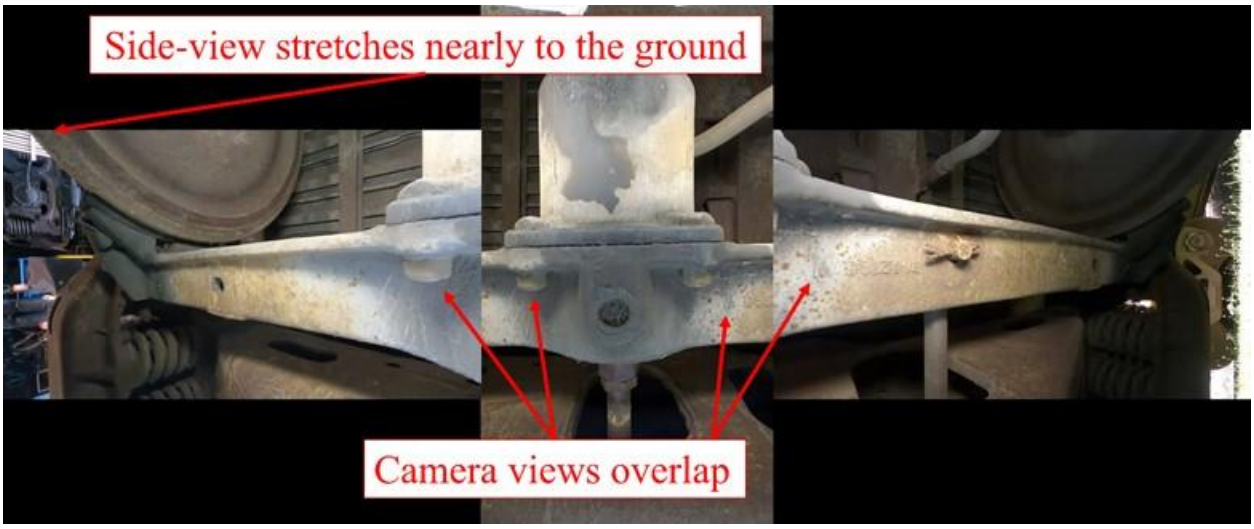

Figure 0-6: Images from the left, vertical, and right-view cameras of a lateral member within the railcar bogie

Figure 0-6 presents the images for the first case. The images primarily capture a lateral member within the bogie of a railcar, one of the lowest components within the railcar, which stretches across the entire undercarriage. The two side-view cameras clearly overlap with the view of the vertical camera, demonstrating a lack of gaps between the views. Additionally, the side-views capture the full length of the lateral member and stretch nearly to the ground on either side.

Figure 0-7: Images from the left, vertical, and right-view cameras of a lateral member within the railcar bogie

Figure 0-7 presents the images as the TCR passes beneath a set of hopper gates. Again, the side-view images overlap with the vertical image. The opening of the left hopper gate is visible in two images, and the bolts on the side of the right hopper gate are visible in two images. The side views then capture the full width of the undercarriage. The lateral sides of the hoppers are not viewable

as they are obscured behind the hopper gates; however, a trackside inspector can readily view this portion of the undercarriage without issue.

These two cases demonstrate the robust ability of the imaging system to capture the entire undercarriage in at least one image. An operator could then conduct a single pass with the TCR and be confident that no areas will be overlooked. The undercarriage robot developed by Chiaradia et al. [44] can image components from multiple angles using its articulated arm, whereas the TCR can only gather a single angle, creating the possibility for blind spots. However, this robot cannot match the single-pass efficiency of the TCR. Inspectors will not have the time to manually traverse to each component of interest and control an articulated arm to gather multiple views. The same is true for the ATUVIS robot [45]. This system performs a similar task to the TCR but cannot image the entire railcar in a single pass. Usage of this device for a pre-departure inspection would require manual control of the cameras to reach every component of interest. In pre-departure inspections, inspectors need an efficient, reliable method for gaining a clear point of view of the entire undercarriage. The TCR could help identify many more undercarriage defects than is now possible during pre-departure inspections, and technologies, such as the previously mentioned robots, may be suitable for maintenance-point inspections of areas suspected of possessing defects where efficiency is not as great of a concern.

1.39.3. Control

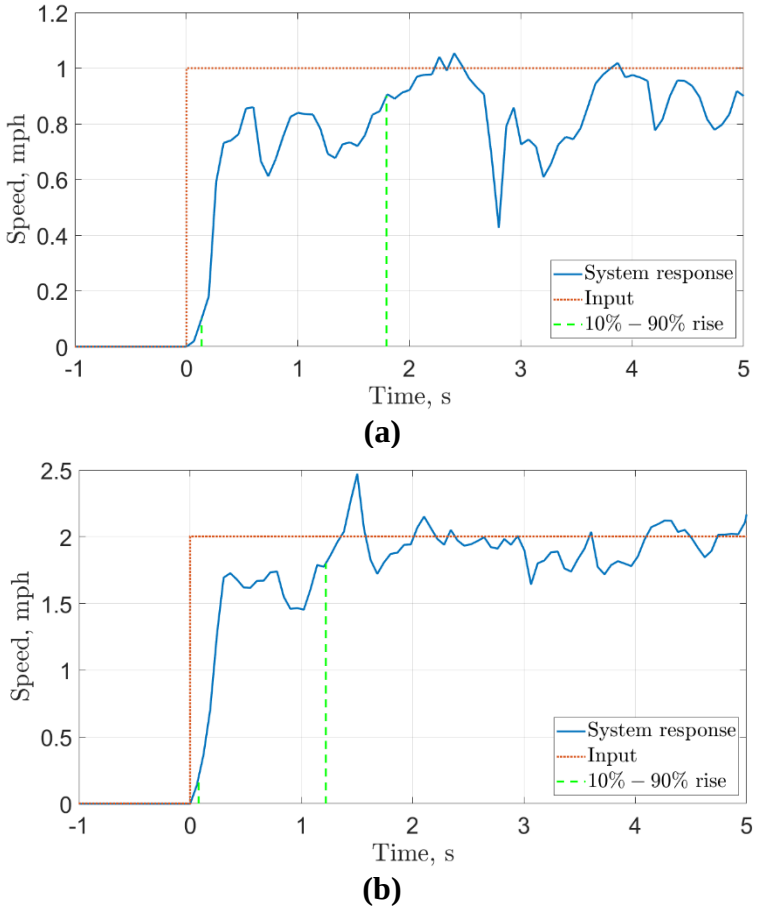

Figure 0-8: Step response during the railcar undercarriage inspections at (a) 1 mph and (b) 2 mph

Figure 0-8 presents the step responses during the 1-mph (Figure 0-8a) and 2-mph (Figure 0-8b) tests with the 10%-90% rise highlighted. The left motor data was analyzed in each case. In both cases, the TCR quickly accelerates toward the testing speed before apparent disturbances cause a short plateau. For the 1-mph test, the 10%-90% rise time is 1.7 s. and 1.1 s. for the 2-mph test. In both cases, the TCR reaches testing speed within 2 seconds. Interestingly, the 2-mph case reached testing speed before the 1-mph case. This is likely because the TCR carried more momentum during the 2 mph, making it less responsive to disturbances from the rough track bed environment. Despite the disturbances, the control system quickly brings the TCR to an approximate testing speed in each test. The speeds do not settle, however. Disturbances throughout the test cause deceleration, and as the TCR increases power to return to the desired testing speed, a decrease in resistance can then cause overshoot. Again, the data from the 1-mph test shows that the TCR is more sensitive to disturbances in this case. The decelerations are much larger proportionally than those observed during the 2-mph test.

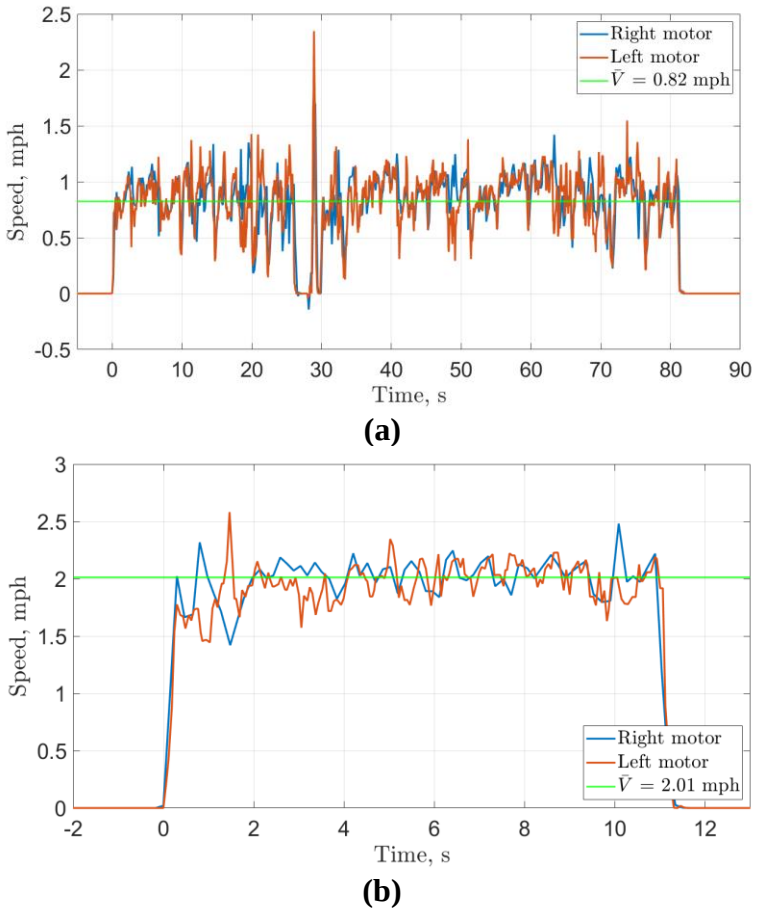

Figure 0-9: Motor speed data throughout the railcar undercarriage inspections at (a) 1 mph and (b) 2 mph

The speed data from each motor throughout both tests are presented in Figure 0-9. Again, the 1-mph test (Figure 0-9a) shows a high sensitivity to disturbances. There was even a moment during this test near the 25 s. mark where a collision with a tie caused the TCR to stop, and the control effort was not large enough to immediately accelerate the TCR again. A large throttle had to be

manually applied to bring the TCR over the edge of the tie before the step input could be reapplied. This period of stoppage and other large decelerations led to the average speed during the test being 0.82 mph, nearly 20% less than commanded. The 2-mph case (Figure 10-9b) shows a much better resilience to disturbances. Although the speed does not settle at any point throughout the test, the speeds remain much closer to the commanded speed than during the 1-mph case. Compared to the 1-mph case, where disturbances cause large deceleration, and the 3-mph case, which was not tested due to its potentially damaging shock loads, the 2-mph testing speed strikes a medium between the two. In this case, the TCR possesses enough momentum to roughly maintain its speed throughout constant disturbances; however, the speed is not too great to cause violent collisions, risking damage and loss of control. As a result, the average speed for this test was 2.01 mph, less than 1% off from the commanded speed. These results demonstrate that 2 mph is the most appropriate operating speed for the TCR, given its current design. Additionally, 2 mph is still much quicker than the speed of a manual inspection. Rather than the 60 s. per car given to an inspector, the TCR could inspect a 60 ft. long rail car in just 20 s.

The railcar inspection tests served to qualitatively demonstrate the ability of the FPV system to effectively provide control feedback in its operating environment. The FPV system was used almost exclusively to determine the TCR's heading and position throughout the tests. As hypothesized, it was difficult to direct the TCR using line-of-sight control, and line-of-sight was impossible as the TCR passed beneath bogies. Throughout each test, the TCR never struck either rail or any components. The constant and low-latency feedback was sufficient for maintaining the TCR's course in the center of the tracks. The camera also demonstrated an ability to adjust its sensitivity for operating beneath the railcar and when exposed to the sky between railcars.

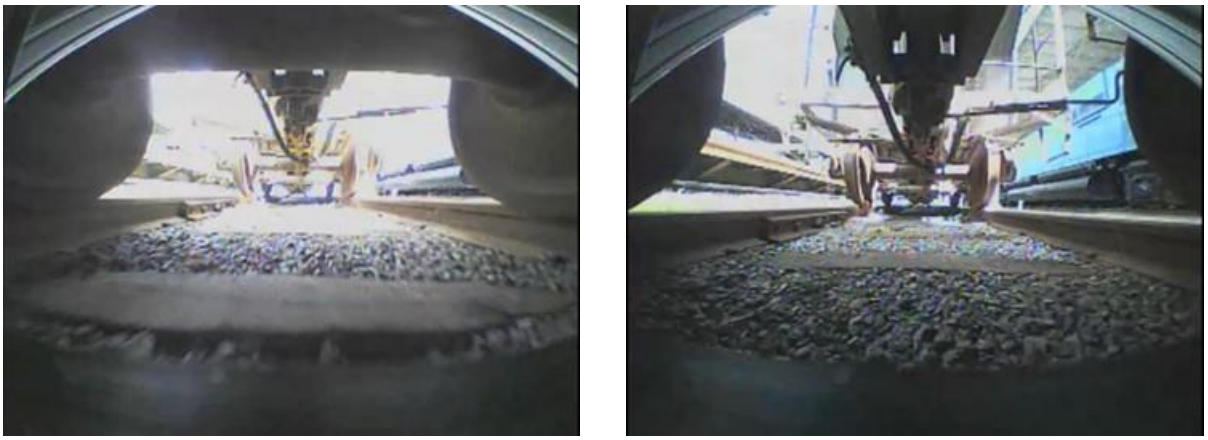

(a) **(b)**

Figure 0-10: Images from the FPV camera as the TCR transitions from (a) beneath the railcar to (b) between the railcars

Figure 0-10 shows frames from the FPV footage as it transitions from beneath a railcar to in between. While under the railcar (Figure 0-10a), the area directly in front of the TCR is saturated due to the much brighter light from the sky. However, 0.33 s. later, the TCR is still traveling out from beneath the railcar, and the scene directly in front is now well-exposed, Figure 0-10b. The system quickly adjusted to the oncoming environment, and the risk of an operator being unable to avoid a collision due to inadequate lighting is deemed minimal.

These results showed that the TCR could now be easily controlled at its operating speed of 2 mph within the operating environment of a track bed beneath a railcar. The control system quickly brings the TCR up to testing speed and roughly maintains its speed despite disturbances. The FPV system has also proven itself to be a robust method for providing adequate feedback to the operator throughout the tests. To improve the disturbance rejection of the system and achieve a speed that settles at the commanded value, mechanical alterations would most likely be necessary. Due to the dynamics of the TCR, collisions will almost assuredly cause the sharp decelerations seen in the data. Modifications, such as a suspension system, could serve to dampen those disturbances and achieve more desirable dynamics.

1.39.4. Mobility and Reliability

The mobility test conducted on revenue service tracks was completed as planned. The TCR climbed over the rails, completed a 180° turn, and climbed out again,
Figure *0-11*.

(a) **(b)** **(c)**

Figure 0-11: Images from the mobility test on revenue service track: (a) climbing into the track bed, (b) turning, (c) climbing out of the track bed

Completing this test demonstrates that the TCR has been equipped with the mobility necessary to conduct undercarriage inspections of railcars unassisted. The test was completed relatively smoothly. Rail climbing into the track bed was delayed slightly as the TCR struggled to gain traction from the trackside ballast. The TCR had to be driven forward and reverse slightly to then gain enough traction to complete the maneuver. Turning within the rails was completed much the same as in the previous tests. The maneuver lasted around 18 s. The TCR was able to quickly climb out of the track bed without any issue. The TCR was controlled during turning so that the tracks would lie on ties before attempting to climb out of the track bed. Aligning the TCR in this way eliminates the effect of the ballast on the traction available to the TCR, allowing climbing out of the track bed to be conducted quickly and consistently.

Equation (11-1) presents the method for estimating the TCR's range.

$$Range = \frac{C_{battery}}{\bar{I}_{left} + \bar{I}_{right} + \bar{I}_{lights}} * \bar{V} \tag{11-1}$$

The I-bar terms represent the average battery current drawn by the left and right motors throughout a given test. The average current from the lighting system is added to these values to estimate the total battery current draw. The battery's capacity is divided by this total current. The battery pack's capacity is listed as 16 Ah, Table 0-1. This term then results in an estimated lifetime of the battery in hours. Multiplying this value by the average speed of the test, in mph, results in an estimated range of the TCR in miles. The BMS app interface determined that the lighting system draws approximately 7.2 A from the system when powered. This current value was added to the total battery current drawn from each motor to approximate the total current being drawn from the battery at a time. The average current drawn from each motor was found by isolating the steady state portion of the test after the TCR had accelerated to its operating speed. The current during this portion of the test was then averaged for each motor.

Table 0-1: Estimated ranges for the TCR at various operating speeds

Test	Average Speed (mph)	Avg. Batt. Current (A)	Lifetime (hr.)	Range (mi.)
1-mph	0.82	12.67	1.26	1.04
2-mph	2.01	16.47	0.97	1.95

Table 0-1 presents the final results from this analysis. The results demonstrate that the TCR's range in both the 1-mph and 2-mph cases is on the scale of a typical train length. The AAR reports that the median train length is 5,300 ft. (1.00 mi.) [71]. The TCR's range at both 1 and 2 mph is sufficient to cover this distance; however, this length is very close to the maximum range at 1 mph. The AAR reports that 10% of trains are greater than 9,600 ft. (1.82 mi.) in length. The 2-mph range of 1.95 miles is still sufficient to cover this distance; therefore, the TCR is estimated to be capable of conducting undercarriage inspections on over 90% of trains on a single battery life when operating at 2 mph. Interestingly, the range nearly doubles from 1 mph to 2 mph. This is most likely due to two factors. Firstly, the proportion of current due to the lighting system is much greater during the 1-mph test. The 7.2 A of lighting current is 57% of the total battery current compared to 44% during the 2-mph test. Secondly, as mentioned in the control section, the TCR traverses the rough terrain of the track bed more smoothly at 2 mph. At this speed, the TCR's momentum carries it through collisions, while it can experience sharp decelerations or become jammed at 1 mph. These two effects compound such that the 2-mph battery current is only 30% higher than the 1-mph test, even though the actual average speed was increased by 145%. As a result, the range of the 2-mph test was greatly increased from the range of the 1-mph test, further demonstrating its suitability as the TCR's operating speed during these inspections.

No component failures were discovered after completing the railcar inspections at 1 and 2 mph. Multiples of these tests were completed, and the absence of any failures demonstrates that the TCR is reliable for operating at speeds up to 2 mph, although it is difficult to predict a system's future reliability. However, a failure with the tracks was observed during the mobility tests. Firstly, the tracks were becoming derailed when attempting to conduct a turn on the trackside ballast. The tracks were relocated back on the sprockets before conducting the test. After the test was conducted, the TCR was being driven trackside, and one of the track links failed. The plate that connected two of the track links on one end was missing, and the remaining plate had become deformed under the increased loading. It is unclear whether the plate was missing before the failure occurred or whether this failure contributed to the tracks becoming derailed. Regardless, the tracks

may be regarded as a weak point mechanically on the TCR. During turning, the tracks will be subjected to large amounts of torque while sliding across the rough ballast surface. These conditions make derailment and failures more likely. Further investigation and improvement of the track system may be an important part of future work. The TCR must be equipped to reliably complete undercarriage inspections. Although still imperfect, the TCR's reliability has been greatly improved through mechanical modifications and alterations to the system's operating parameters.

Chapter 12
Conclusions and Future Steps

A summary of the results and findings of the research is provided, along with a few recommendations for future studies.

1.40. Summary

The design details of the Track Crawler Robot (TCR) were presented, including its performance requirements, original design, modifications and improvements made during this study, and the results of laboratory and field testing. Each subsystem was assessed for its ability to complete the railcar undercarriage inspection that the TCR is intended for. Those needing improvements were evaluated further and modified, tested, and retested until they met the performance requirements. The original state of the TCR was presented in detail. Key parameters were presented and calculated when applicable. The system's operational requirements were discussed, and the resulting challenges were highlighted. The imaging and lighting systems were known to be inadequate and needed modification. The field of view (FOV), control, mobility and reliability, and safety of the TCR were also suspected of being inadequate and needed investigation.

Giovanni Mantovani's previous work to improve the imaging system's vibrational response was presented. Dampers were included to reduce the transmission of vibrations into the imaging platform. The need for the Test Bed was then discussed, and its construction for this project was detailed. After tests across the Test Bed, it was found that the vibrational dampers effectively reduced the transmission of high frequency vibrations into the imaging platform; however, lower frequency vibrations could be amplified.

The image quality gathered by the TCR was then covered in detail. An assessment of the original imaging system was presented, highlighting issues with motion blur, lighting interference, and video stability. These issues were isolated, and the occurrence of each was explained. Raising the shutter speed to 1/1920 s. effectively eliminated the presence of motion blur at speeds of up to 6.5 mph on asphalt. Limiting the minimum sensitivity of the camera's sensor prevented bright lights from degrading the image quality of the undercarriage. Lastly, the utilization of a video stabilization program reduced jolts and rotations within the video while slightly reducing the FOV of the camera.

The TCR was then investigated for its ability to image an entire railcar undercarriage. The original FOV of the system was found through testing and only spanned 30% of the required amount. Frame and track routing concepts were presented to relocate components which obstructed the full FOV. The redesign of the frame structure was supported using static finite element analysis (FEA) and a modal analysis. After the system was modified, the addition of two side-view cameras expanded the FOV of the imaging system. The final FOV of the system was presented and shown to exceed the amount required to image a full undercarriage.

The lighting system of the TCR was then improved. High shutter speed imaging reduces the light gathered per frame. The amount of light required to adequately expose a high shutter speed image was quantitatively found by imaging at lower shutter speeds until proper exposure was observed. Light bars were chosen to supplement the original lighting system. The choice of the light bars was supported by the previous tests. The need for diffusion over these light bars was demonstrated using theory and gathered images of a pickup truck undercarriage. Proper diffusive methods were found through testing. Finally, the positioning of the added light bars was examined quantitatively, and the system was validated by testing beneath a tractor-trailer. The final system was shown to adequately illuminate the overhead and far lateral regions of an undercarriage for imaging at high shutter speeds.

The control of the TCR was investigated and improved in two areas. The shortcomings of motor current control in varying environments were discussed, and feedback control using a PID controller was implemented. Various tasks were completed to correctly implement the PID control, including mitigating overcurrent faults, calibration of the two electronic speed controllers (ESCs) with one another, and calibrating the ESC speed with land speed. The resulting system was able to control the TCR across the Test Bed at a relatively constant speed. The control was then evaluated from the perspective of the operator. The need for improved feedback was discussed, and a first-person view (FPV) system was presented to meet this need. The integration of the FPV system with the TCR and radio remote using 3D-printed mounts was presented. Testing was then presented, demonstrating the ability of the FPV system to provide feedback with low latency while experiencing vibrations and lighting changes.

The mobility and reliability of the TCR were then investigated. The undercarriage idler assemblies were shown to be in a location that potentially exposed them to hitting objects on the track and being damaged. These assemblies were improved using idler sprockets with integrated bearings. These assemblies relocated all moving components out of the direct path of the ballast. The redesign was supported using FEA; however, testing led to a failure in the mounting assembly. The failure was corrected by greatly strengthening the mounting assembly, using larger bolts and mounting across the frame member rather than within the t-slot. This failure also led to the decision to reduce the maximum operating speed of the TCR from 3 mph to 2 mph to avoid unnecessarily high loading. However, this speed still allowed the TCR to conduct inspections at 3 times the speed of inspectors. Next, the ability of the TCR to complete key maneuvers, such as rail climbing and turning within the track bed, was evaluated. An inability to consistently climb in and out of the track bed was discovered. A protective plate could collide with the railhead or rest on the railhead, leading to a loss in traction. Also, loose ballast within the track bed caused traction loss, inhibiting rail climbing. The inclusion of an additional undercarriage idler assembly was proposed to correct the issue. The idler eliminated the railhead's ability to contact the protective plate's leading edge. Lowering the protective plate and increasing track tension were also necessary to allow the TCR to consistently climb the rail when sufficient traction was available. It was also demonstrated that the additional idler assembly aided in turning within the rails, and a hypothesis for why was presented.

The safety of the TCR was investigated. It was discovered that the battery could trigger the manual reset on the 100 A circuit breaker during sudden decelerations. It was later found that this circuit breaker was faulty and could close the circuit after being tripped. An auto-reset circuit breaker was used as a replacement and has worked consistently since. A BMS was then added to monitor the battery throughout operation. A BMS is standard on batteries of such size, and its inclusion effectively eliminates the possibility for cells to drop beneath their acceptable voltage as had occurred.

The modified systems were then evaluated in a final round of tests. Each test was designed to evaluate a given system in the real-world inspection environment. The tests involved traversing the track beneath a set of railcars. Images were taken throughout the tests, approximating the process for a typical undercarriage inspection. The image quality and lighting systems were found to be greatly improved. The images gathered were clear and well-lit, allowing components to be readily identified and tracked. The FOV was also shown to be sufficient for imaging each section of the undercarriage from at least one point of view. The PID control system was shown to be capable of controlling the system at 1 and 2 mph in the track bed. Data suggested that 2 mph travel was more advantageous for traversing the rough terrain and led to an almost 2-mile range, longer than over 90% of trains. The FPV system was used to provide control feedback throughout the tests. The video footage proved to be sufficient for control beneath the railcars even as the TCR was not directly in view. Testing on revenue service track demonstrated that the system could consistently complete all necessary maneuvers during an undercarriage inspection. However, the reliability of the track system remains a weak point within the system and should be investigated further.

1.41. Significant Findings and Conclusions

The following section will present the most significant findings from this research and explain their importance.

1.41.1. Demonstration of Ability to Image in Real-World Inspections

One of the foremost achievements of this work is the modification of the TCR system such that it can gather clear images of entire railcar undercarriages while conducting a mobile inspection. At the onset of this project, issues of motion blur, insufficient FOV, and insufficient lighting, among others, prevented the system from gathering images that would be useful for defect detection. The successful implementation of this capability is paramount to the success of the TCR. Without the ability to gather the necessary data, the TCR will never be considered for usage in industry.

This capability was implemented by the intentional modification of the imaging, lighting, frame, and track routing subsystems of the TCR. Shutter speed proved to be a crucial imaging parameter for reducing motion blur. By increasing the shutter speed sufficiently, the relative motion within a single frame was low enough not to be visually noticeable, providing the necessary image clarity for inspections. This alteration had the additional effect of reducing the amount of light gathered in a single frame. The decrease in light gathered served to degrade the image quality significantly. The lighting system was then improved by the addition of two high-powered light bars. The light bars were designed as floodlights; however, the beam did not spread out nearly as widely as was needed. At such close distances, the light bars were effectively working as spotlights. Diffusion was then introduced to widely spread the beam over the entire undercarriage.

At the start of the project, only 30% of the undercarriage could have been captured when components were located at the lowest height of 15 in. It was determined that a single GoPro® could not image the entire area at that distance. Additionally, frame and track components were located within the required FOV, directly prohibiting the imaging of a full undercarriage. The frame and track routing were first modified to make full undercarriage imagery possible. Two side-view cameras were then added to increase the FOV of the imaging system. In this configuration, the imaging system could capture an entire railcar undercarriage while using the Linear digital lens, which effectively eliminates image distortion.

When evaluated beneath a set of railcars in a test meant to simulate an undercarriage inspection, these modifications led to clear, well-lit images that spanned the entire width of the undercarriage, Figure 0-1. As noted earlier, neither the robot developed by Chiaradia et al. [44] nor the ATUVIS robot [45] possess this capability. Both systems are incapable of imaging the entire undercarriage in a single pass, greatly hindering their efficiency. The pre-departure inspections directly keep a fully loaded train from departing to its destination, and efficiency is of the highest priority. To the author's knowledge, the TCR is the only system capable of gathering the necessary defect detection data as efficiently as would be needed to be successful in this environment.

Figure 0-1: Aligned images of a railcar undercarriage taken from each camera

Components were clearly identifiable and could readily be tracked from frame to frame. With this level of data collection, it would be possible for a trained inspector to observe the footage from the TCR and identify defects beneath the train. As the current data is stored in 3 distinct videos, these videos could be stitched together in post-processing to provide an inspector with a single video spanning the entire width of the railcar. The imaging data that the system can now gather could also serve as the building blocks for an automated defect detection model. With the rapid advances in computer vision and AI technology, it can be imagined that an automated defect detection model could be designed to interface with the gathered images of the TCR. The model could be sufficiently trained given a large enough dataset from undercarriage inspections. Therefore, the imaging capabilities that have been developed in this study could lay the groundwork for systems that take responsibility for the pre-departure inspection of railcar undercarriages. The inspectors could be free to spend their time on more readily accessible points of inspection, and they would only need to inspect the undercarriage where the system identifies a potential defect. This capability would increase the effectiveness of the inspections while retaining the efficiency that is required by the railroads.

1.41.2. Significant Control System Improvements

The work conducted in this study has greatly increased the ability of the TCR to be controlled in the railcar inspection environment while reducing the amount of effort required by an operator to do so. At the onset of this project, the TCR was controlled via line-of-sight and with the need for a constantly varying throttle input from the operator. The operator would have been constantly responsible for adjusting the throttle input to the TCR to account for the varying terrain of the track bed. Simultaneously, the operator would have been tasked with constantly maintaining line-of-sight with the TCR as it passes beneath low-lying components and bogies, which completely obscure it. This method of control would have made it extremely difficult to maintain the TCR's position centered beneath the railcar. Additionally, it would require much effort and concentration from the operator throughout the inspection.

To improve this system, the ESCs were configured to regulate speed in a feedback loop, and the operator was provided with constant, low-latency video feedback using an FPV system. The ESCs

were originally mapping inputs from the operator to a motor current. This method of control was sufficient for operation on relatively smooth surfaces where the resistance to forward motion remained constant. However, on the track bed, a constant motor current resulted in drastic speed changes throughout a test and the potential for stalling. The ESCs could map control inputs to motor speeds using a PID controller structure and read the motor speed data from the Hall effect sensors within each motor for feedback. Once implemented, the ESCs had to be calibrated with one another, as they were operated completely independently. Additionally, the speeds recorded by the ESCs had to be calibrated with their corresponding land speeds. Once implemented, the operator could flip a switch to apply a constant throttle input of their choosing. The throttle curve was defined such that the operator could choose a certain throttle value to command a given land speed. The TCR would then regulate the control effort throughout the test, leading to a relatively constant speed. This improvement completely alleviated the burden of speed control from the operator. The only control inputs necessary throughout the inspection would be steering inputs to correct the TCR's course.

Hobby-grade FPV components were utilized to implement the system. A camera and transmitter combination transmitted video footage to a monitor connected to the radio remote at extremely low latency. The camera was shown to be resilient to vibrations and lighting changes, although a cooling fan was installed to prevent overheating. With the system installed, the operator always has access to low-latency video footage from the front of the TCR. The operator could now monitor this footage while applying any necessary steering inputs. These improvements served to equip the TCR with a control system that could feasibly be used in a commercial product. Minimizing the effort and potential frustration surrounding the operation of the TCR is critical to its success. An operator required to constantly adjust the throttle and strain to maintain line-of-sight with the device could quickly grow frustrated and abandon using the device altogether.

The remaining drawback in this area is the need for an operator to constantly monitor and control the TCR's progress. Although the effort required by the operator is minimal, it is unrealistic to expect any level of meaningful inspection to be conducted by this operator while also monitoring the TCR. This factor serves to degrade the efficiency of the TCR as it would require an additional carman to be assigned to the inspection. Ideally, once in place, the TCR would autonomously navigate the length of the train to conduct the inspection. The efficiency of the inspection would not be affected in this case, as both carmen could focus on the inspection as before, and efficiency would be improved as the carmen would only be responsible for inspecting the undercarriage in the case of a suspected defect, assuming an automated defect detection model had also been developed. The control system developed for this project could serve as the basis for a future autonomous system where FPV footage is used for feedback to an autonomous system that supplies control inputs to the ESCs that are utilizing PID controllers, or perhaps an entirely different system would be required. Regardless, for the purposes of this study, the control system has been sufficiently improved to be usable in a real-world inspection.

1.41.3. Development of Mobility to Conduct Unassisted Inspections

Another key accomplishment of this project is the improvement of the TCR's mobility so that it can complete all necessary maneuvers for an undercarriage inspection. At the onset of the project, most notably, the system was incapable of consistently climbing over the rail. Without being

capable of completing this maneuver, the TCR would have required manual assistance throughout the inspection. This would have taken valuable time and may have been very difficult if the TCR were unable to climb out of the track bed while located beneath a railcar. To supply the TCR with the necessary mobility requirements, an additional pair of undercarriage idler assemblies was included in the design. Along with increased track tension and ground clearance, these changes have allowed the TCR to reliably and quickly climb into and out of the track bed when traction is available. As ballast may slip, reducing traction and making rail climbing impossible, it was found that controlling the TCR such that its tracks laid on ties before attempting rail climbing was highly effective for ensuring that ample traction was available. The above-mentioned modifications were also hypothesized to have improved the system's dynamics during turning, and a test revealed a 40% decrease in time to complete the maneuver.

1.41.4. Advancements to System Durability and Safety

Throughout the project, various issues arose, threatening the durability and safety of the TCR during operation. The ballast was originally impacting the undercarriage idler assemblies, causing damage. These systems were modified to relocate all moving components from the direct path of the ballast during operation. The mounting assembly of the modified assembly failed during testing and was greatly strengthened as a response. Due to these modifications, the undercarriage idler assemblies remain undeformed, and the bearings continue to operate. Additionally, issues with a faulty circuit breaker and insufficient monitoring of the battery were corrected throughout the course of the projects. Each of these corrections helped reduce the chance of a runaway short circuit within the system, which could be catastrophic. The TCR could never gain traction in the industry if it operated unreliably or dangerously. This work has greatly improved the TCR's performance in both categories. The TCR now possesses an adequately safe electrical system, and it has been shown that it can operate reliably at 1 and 2 mph speeds within the track bed. Unfortunately, when mobility maneuvers were conducted trackside, track derailment and track failure were observed. These issues threaten to delay the operation of the TCR when needed for an inspection. Although much improved, the reliability of the TCR must be thoroughly investigated in terms of the track performance, and necessary improvements must be completed.

1.42. Recommendation for Future Studies

Several additional studies could be pursued to continue the development of the TCR system and further prepare it for the possibility of being adopted by the rail industry. The proposed steps will be grouped into the key subsystems.

Imaging System: Additional research could be conducted in the future to make use of the excellent imaging data being gathered by the TCR. As noted earlier, image processing methods could be investigated for improving the quality of the 1/1920 s. shutter speed images. This would allow for adequate images to be taken at an even higher shutter speed to help guarantee the elimination of motion blur even at higher speeds. However, the processing time of this method would need to be investigated, as the inspectors will need to know of defects within a few minutes of the inspection. If manual inspection of the video appears to be most viable, post-processing algorithms could be developed to automatically align and stitch the three video feeds together to create a single continuous scan of the undercarriage. Stereoscopic camera arrangements could also be

investigated. The resulting videos could be used to create 3D models of the undercarriages using photogrammetry. It could be investigated whether the construction of these 3D models aids in defect detection, whether manual or automated. Short-range LiDAR systems are now widely available to consumers with their inclusion on some newer iPhone® models. The systems could be investigated for their ability to gather direct 3D data from the railcar undercarriages when mounted onto the TCR. If the data becomes usable, one can also attempt to synthesize the 3D point cloud with the images captured by the onboard cameras to create a detailed 3D model of the railcar undercarriage.

Light System: Improvements to the lighting system could be investigated. At high shutter speeds, more lighting would allow the camera to lower its image sensitivity, reducing noise within the image. Additionally, the system struggled to adequately light laterally located objects such as the rail wheels. Modifying the lighting system to better light those areas and increase lighting across the entire undercarriage would improve the image quality if done correctly. Larger light bars could be added to the system to increase the lighting. Commercial diffusers could be used in place of the frosted plexiglass and wax paper used currently. These diffusers would provide more repeatability in the level of diffusions as well as increase the sophistication of the system.

Mobility: It was noted in the final mobility tests that the tracks remain a weak point in the system. Derailment of the tracks occurred while turning on rough ballast surfaces trackside. One of the track links then failed after the test was completed. Such issues reduce the reliability of the TCR as a commercial system, where reliable and consistent operation is required for success. Improvements to the track system should be investigated. Continuous rubber track systems could be designed at this scale. If it is determined that they would improve the reliability of the system, provisions must be made to retrofit the TCR to change the tracks. A rubber track system may provide superior engagement between the idler assemblies and the track, preventing derailments. The inclusion of suspension may also help in this area, among others. Suspension systems could be included between the idler sprocket assemblies and the frame of the TCR. With the inclusion of suspension, the idlers move along with the track rather than being rigidly located. Suspension may allow the undercarriage idler sprockets to engage more effectively with the chain links on the side of the track, making derailments less probable. Each idler sprocket would apply a force into the track during normal operation and could take up slack by moving through its travel. Additionally, suspension may allow the TCR to controllably and reliably travel at increased speeds within the railroad track beds. The limiting factor for increasing the operating speed of the TCR is the jarring experienced when impacting ties at higher speeds. The ability to better absorb these impacts is expected to increase the system's operating speed and overall efficiency. Suspension, however, would increase the TCR’s complexity and possibly weight.

An entirely different platform could be investigated as well. It is possible that scale-model RC trucks with integrated suspension could be used as an effective platform. A high-quality RC truck could be chosen with large wheels and integrated suspension. The truck may be capable of climbing the rail or could be modified to do so. Additionally, some designs feature front and rear steering, allowing for maneuverability between the rails. An RC truck may be capable of traveling at higher speeds than the TCR with the help of its suspension. However, concerns such as the RC truck’s range or ability to bear the weight of components would need to be investigated.

Autonomy or Semi-autonomy: The current TCR must be controlled manually, and defects must be investigated manually. Although substantial improvements have been made to the original system, there is much room for further improvement toward its full potential. Achieving a fully autonomous system that can operate in parallel with the inspector would propel the TCR to being a highly valuable system for railroad use in track yards, siding, and other locations where train inspections may be necessary. Autonomous defect detections would need to be investigated for their efficiency and efficacy. The inspectors must be notified of potential defects within several minutes. Image processing cannot take hours or days to complete. Methods for autonomously detecting defects in an efficient manner should be investigated.

References

[1] 2020, "Freight Rail Overview," FRA [Online]. Available: https://railroads.dot.gov/rail-network-development/freight-rail-overview. [Accessed: 22-Apr-2024].

[2] "Train Accidents and Rates," FRA [Online]. Available: https://safetydata.fra.dot.gov/OfficeofSafety/publicsite/Query/TrainAccidentsFYCYWithRates.aspx. [Accessed: 22-Apr-2024].

[3] Moscoso, B., "Safety in Motion: How Decades of Technological Progress Makes Railroads Safer," Association of American Railroads [Online]. Available: https://www.aar.org/article/safety-in-motion-how-decades-of-technological-progress-makes-railroads-safer/. [Accessed: 21-Jul-2024].

[4] Kasch, J., and Ahmadian, M., 2024, "Design and Operational Assessment of a Railroad Track Robot for Railcar Undercarriage Condition Inspection," Designs (Basel), **8**(4), p. 70 doi: 10.3390/designs8040070.

[5] Norfolk Southern Corporation, 2023, "Norfolk Southern Launches AI Train Inspection Technology," PR Newswire [Online]. Available: https://www.prnewswire.com/news-releases/norfolk-southern-launches-ai-train-inspection-technology-301968329.html. [Accessed: 22-Apr-2024].

[6] Gratas, S., 2024, "Jackson Rail Line Gets Latest Tech in Norfolk Southern's Efforts to Improve Safety," GPB [Online]. Available: https://www.gpb.org/news/2024/04/12/jackson-rail-line-gets-latest-tech-in-norfolk-southerns-efforts-improve-safety. [Accessed: 22-Apr-2024].

[7] US Federal Code of Regulations, 1980, "Pre-Departure Inspection," 49 CFR § 215.13.

[8] "Freight Rail & Train Length," Association of American Railroads [Online]. Available: https://www.aar.org/issue/freight-train-length/. [Accessed: 22-Apr-2024].

[9] Nayebi, K., 2012, "Vision System Tracks Trouble with Trains," Vision Systems [Online]. Available: https://www.vision-systems.com/non-factory/security-surveillance-transportation/article/16737816/vision-system-tracks-trouble-with-trains. [Accessed: 22-Apr-2024].

[10] Maratea, A., and Grissom, D., "The East Palestine Derailment & Overall Rail Industry Safety," Transportation Communications Union [Online]. Available: https://www.tcunion.org/tcu-union/the-east-palestine-derailment-overall-rail-industry-safety/. [Accessed: 22-Apr-2024].

[11] Austin, K. B., 1949, "Hotbox Signal for Railway Trains," U.S. Patent 2486546.

[12] Tarawneh, C., Aranda, J., Hernandez, V., Crown, S., and Montalvo, J., 2020, "An Investigation into Wayside Hot-Box Detector Efficacy and Optimization," International Journal of Rail Transportation, **8**(3), pp. 264–284 doi: 10.1080/23248378.2019.1636721.

[13] Post, W. M., 1937, "Protective System for Railways," U.S. Patent 2095616.

[14] Fu, W., He, Q., Feng, Q., Li, J., Zheng, F., and Zhang, B., 2023, "Recent Advances in Wayside Railway Wheel Flat Detection Techniques: A Review," Sensors, **23**(8) doi: 10.3390/s23083916.

[15] Stratman, B., Liu, Y., and Mahadevan, S., 2007, "Structural Health Monitoring of Railroad Wheels Using Wheel Impact Load Detectors," Journal of Failure Analysis and Prevention, **7**(3), pp. 218–225 doi: 10.1007/s11668-007-9043-3.

[16] Bi, L., Zhao, P., Teng, M., Zhao, L., Liu, X., and Xing, M., 2020, "Wayside Testing Methods for High-Frequency Vertical Wheel-Rail Impact Forces and Its Applicability," Measurement, **151** doi: 10.1016/j.measurement.2019.107197.

[17] Silva, R., Guedes, A., Ribeiro, D., Vale, C., Meixedo, A., Mosleh, A., and Montenegro, P., 2023, "Early Identification of Unbalanced Freight Traffic Loads Based on Wayside Monitoring and Artificial Intelligence," Sensors, **23**(3) doi: 10.3390/s23031544.

[18] Cortis, D., Bruner, M., and Malavasi, G., 2020, "Development of a Wayside Measurement System for the Evaluation of Wheel-Rail Lateral Contact Force," Measurement, **159** doi: 10.1016/j.measurement.2020.107786.

[19] Giannouli, E., Papaelias, M., Amini, A., Huang, Z., Jantara, V. L., Kerkyras, S., Krusuansombat, P., Garcia Marquez, F. P., and Vallely, P., 2021, "Detection and Evaluation of Rolling Stock Wheelset Defects Using Acoustic Emission," Insight: Non-Destructive Testing and Condition Monitoring, **63**(7), pp. 403–408 doi: 10.1784/insi.2021.63.7.403.

[20] Freid, B., Barkan, C. P. L., Ahuja, N., Hart, J. M., Todorvic, S., and Kocher, N., 2007, "Multispectral Machine Vision for Improved Undercarriage Inspection of Railroad Rolling Stock," *International Heavy Haul Conference*, pp. 737–744.

[21] Schlake, B. W., Edwards, J. R., Hart, J. M., Barkan, C. P. L., Todorovic, S., and Ahuja, N., 2009, "Automated Inspection of Railcar Underbody Structural Components Using Machine Vision Technology," *Transportation Research Board 09-2863*.

[22] Hart, J. M., Resendiz, E., Freid, B., Sawadisavi, S., Barkan, C. P. L., and Ahuja, N., 2008, "Machine Vision Using Multi-Spectral Imaging for Undercarriage Inspection of Railroad Equipment," *Proceedings of the 8th World Congress on Railway Research*.

[23] Thillaikkarasi, R., Yaseen, M. M., Rameshbabu, R., Prabhakaran, R., Kesavan, R., and Jose Anand, A., 2023, "Waysides Inspection Using Wayside Processing Imaging and Deep Learning," *Proceedings - 2023 3rd International Conference on Pervasive Computing and Social Networking, ICPCSN 2023*, Institute of Electrical and Electronics Engineers Inc., pp. 359–365 doi: 10.1109/ICPCSN58827.2023.00065.

[24] Raghava Prasad, C., and Kishore, P. V. V., 2017, "Performance of Active Contour Models in Train Rolling Stock Part Segmentation on High-Speed Video Data," Cogent Eng, **4**(1) doi: 10.1080/23311916.2017.1279367.

[25] "Intelligent Train Undercarriage Scanner (ITUS)®," Gatekeeper Intelligent Security [Online]. Available: https://www.gatekeepersecurity.com/products/intelligent-train-undercarriage-scanner/. [Accessed: 21-Jul-2024].

[26] "Vehicle Undercarriage Diagnostics," railvision [Online]. Available: https://rail-vision.com/rolling-stock/wayside-diagnostics/undercarriage/. [Accessed: 21-Jul-2024].

[27] "Under Train Carriage Inspection System," Westminster Group PLC [Online]. Available: https://www.wg-plc.com/product/under-train-carriage-inspection-system. [Accessed: 21-Jul-2024].

[28] "Wagon Inspector of Freight Trains," Railway Training [Online]. Available: https://www.railwaytraining.be/en/schouwer. [Accessed: 22-Jul-2024].

[29] Edwards, R., Barkan, C. P. L., Hart, J. M., Todorovic, S., and Ahuja, N., "Improving the Efficiency and Effectiveness of Railcar Safety Appliance Inspection Using Machine Vision Technology," *JRC2006-94052*, pp. 81–89.

[30] Schlake, B. W., Barkan, C. P. L., Edwards, J. R., and Riley Edwards, J., 2010, "Impact of Automated Condition Monitoring Technologies on Railroad Terminal Performance," *Proceedings of the 2010 Annual AREMA Conference*.

[31] "3.3. Underframe," TPUB [Online]. Available: https://armytransportation.tpub.com/TR06756/TR067560052.htm. [Accessed: 22-Jul-2024].

[32] Tuzik, J., 2023, “Managing Slack in Trains with Cars Equipped with Hydraulic End-of-Car-Cushioning Devices,” Interface.
[33] “US Army Field Manual FM 55-20, Figure 8-8,” Department of the Army.
[34] Schoenherr, E., and Smuda, B., 2005, “Under-Vehicle Autonomous Inspection through Undercarriage Signatures,” *Unmanned Ground Vehicle Technology VII*, SPIE, p. 645 doi: 10.1117/12.603794.
[35] “Our Products,” Techmatics NZ [Online]. Available: https://techmatics.co.nz/our-products/. [Accessed: 22-Apr-2024].
[36] Jing, G., Qin, X., Wang, H., and Deng, C., 2022, “Developments, Challenges, and Perspectives of Railway Inspection Robots,” Autom Constr, **138** doi: 10.1016/j.autcon.2022.104242.
[37] “Railway Inspection Robot,” Shenhao Robotics [Online]. Available: https://www.shenhaorobotics.com/railway-inspection-robot/. [Accessed: 21-Apr-2024].
[38] “Railway,” Loccioni [Online]. Available: https://www.loccioni.com/en/railway/. [Accessed: 21-Apr-2024].
[39] Daniyan, I., Mpofu, K., and Nwankwo, S., 2023, “Design of a Robot for Inspection and Diagnostic Operations of Rail Track Facilities,” International Journal of Quality & Reliability Management, pp. 653–673 doi: 10.1108/IJQRM-03-2020-0083.
[40] 2021, “ANYbotics and Stadler Service AG Explore the Future of Train Maintenance,” ANYbiotics [Online]. Available: https://www.anybotics.com/news/robotic-inspection-in-train-maintenance/. [Accessed: 22-Apr-2024].
[41] Kiselev, G. G., and Korkina, S. V, 2023, “Automation of Inspection of Rolling Stock at a Maintenance Point Using a Robotic Complex,” *AIP Conference Proceedings*, AIP Publishing, USA, p. 020023 (8 pp.) doi: 10.1063/5.0132796.
[42] Yue, S., Haishan, Z., Hao, Y., Zhen, J., and ShenTao, J., 2022, “Research and Design of a Multi Track Daily Inspection Robot for Urban Rail Transit,” *14th International Conference on Measuring Technology and Mechatronics Automation*, Institute of Electrical and Electronics Engineers Inc., Changsha, China, pp. 528–531 doi: 10.1109/ICMTMA54903.2022.00112.
[43] Zhang, M., Ma, L., Shen, K., and Sun, Y., 2023, “Autonomous Localization and Motion Control of Under-Vehicle Inspection Robot,” *IFAC-PapersOnLine*, Elsevier B.V., pp. 3060–3065 doi: 10.1016/j.ifacol.2023.10.1435.
[44] Chiaradia, D., Leonardis, D., Manno, V., Solazzi, M., Masini, P., and Frisoli, A., “A Mobile Robot for Undercarriage Inspection on Standard Railway Tracks,” *Advances in Italian Mechanism Science (IFToMM Italy 2020)*, pp. 362–369.
[45] “ATUVIS Robot” [Online]. Available: https://atuvis.rs/#about-atuvis. [Accessed: 22-Jul-2024].
[46] Duchesneau, D., and Jensen, V., “What Is Dynamic Range?” Adobe [Online]. Available: https://www.adobe.com/creativecloud/video/discover/dynamic-range.html. [Accessed: 22-Jul-2024].
[47] “Camera Histograms: Tones and Contrast,” Cambridge in Colour [Online]. Available: https://www.cambridgeincolour.com/tutorials/histograms1.htm. [Accessed: 22-Jul-2024].
[48] Mansurov, N., 2023, “Understanding Aperture in Photography,” Photography Life [Online]. Available: https://photographylife.com/what-is-aperture-in-photography. [Accessed: 22-Jul-2024].

[49] “What Is Fisheye Lens?” BYJU’s [Online]. Available: https://byjus.com/physics/fisheye-lens/. [Accessed: 22-Jul-2024].
[50] Davidson, C., Long, B., Carlson, J., Goellner, A., and Ingersoll, S., “Understanding Shutter Speed, Both Slow and Fast,” Adobe [Online]. Available: https://www.adobe.com/creativecloud/photography/discover/shutter-speed.html. [Accessed: 22-Jul-2024].
[51] “What Is ISO Sensitivity?” Ricoh [Online]. Available: https://www.ricoh-imaging.co.jp/english/r_dc/photostyle/knowledge/preparation/iso.html. [Accessed: 22-Jul-2024].
[52] “4750 CU. FT. COVERED HOPPER,” BNSF Railway [Online]. Available: https://www.bnsf.com/ship-with-bnsf/ways-of-shipping/equipment/pdf/Large.pdf. [Accessed: 22-Apr-2024].
[53] 2010, “136-Lb/Yd AREMA Rail,” Harmer Steel [Online]. Available: https://www.harmersteel.com/tee-rails/136-lb-yd-arema-rail/. [Accessed: 22-Apr-2024].
[54] “Electric Skateboard Motor 6355 190KV,” Torque Boards [Online]. Available: https://diyelectricskateboard.com/products/electric-skateboard-motor-6355-190kv. [Accessed: 15-Jun-2024].
[55] “What Is Gear Ratio & How Do You Calculate It?” Accu [Online]. Available: https://accu-components.com/us/p/442-what-is-gear-ratio. [Accessed: 15-Jun-2024].
[56] “ANSI Standard Rolling Chain,” Renold Jeffrey [Online]. Available: https://www.renoldjeffrey.com/media/2395574/ansi-standard-roller-chain-renold-jeffrey.pdf. [Accessed: 15-Jun-2024].
[57] “Sprocket Size Chart,” Peer Chain and Sprockets [Online]. Available: https://www.peerchain.com/resources/sprocket-size-chart/. [Accessed: 22-Jul-2024].
[58] “Headway 38120HP 8Ah LiFePO4 Battery Cell,” EV Lithium [Online]. Available: https://www.evlithium.com/Headway_Battery/898.html. [Accessed: 22-Jul-2024].
[59] “FSESC 4.12 50A Based on VESC 4.12,” FLIPSKY [Online]. Available: https://flipsky.net/collections/v4-series/products/torque-esc-vesc-%C2%AE-bldc-electronic-speed-controller. [Accessed: 22-Jul-2024].
[60] Molzon, M., and Ahmadian, M., 2022, “Development of a Mobile Robot System for the Visual Inspection of Railcar Undercarriage Equipment,” *2022 Joint Rail Conference*.
[61] “DEWE-43A Technical Specifications,” Dewesoft [Online]. Available: https://dewesoft.com/products/dewe-43/tech-specs. [Accessed: 22-Jul-2024].
[62] “6105 Aluminum Extrusions,” Tri-State Aluminum [Online]. Available: https://tri-stateal.com/aluminum-alloy-6105/. [Accessed: 15-Jun-2024].
[63] “Von Mises Criterion (Maximum Distortion Energy Criterion),” Engineers Edge [Online]. Available: https://www.engineersedge.com/material_science/von_mises.htm. [Accessed: 15-Jun-2024].
[64] Paschotta, R., “Lambertian Emitters and Scatterers,” RP Photonics Encyclopedia [Online]. Available: https://www.rp-photonics.com/lambertian_emitters_and_scatterers.html. [Accessed: 22-Jul-2024].
[65] Paschotta, R., “Diffusers,” RP Photonics Encyclopedia [Online]. Available: https://www.rp-photonics.com/diffusers.html. [Accessed: 22-Jul-2024].
[66] Liang, O., 2021, “FPV Camera Latency Testing,” Oscar Liang [Online]. Available: https://oscarliang.com/fpv-camera-latency/. [Accessed: 22-Apr-2024].

[67] Somers, S., “Thermal Management Part 1: How Hot Is Too Hot?” Extron [Online]. Available: https://www.extron.com/article/thermalmgt1_ts. [Accessed: 22-Apr-2024].
[68] “At What Temperature Do Conventional Electronics Packages Fail?” TWI [Online]. Available: https://www.twi-global.com/technical-knowledge/faqs/faq-at-what-temperature-do-conventional-electronics-packages-fail. [Accessed: 22-Apr-2024].
[69] “Understanding LiFePO4 Low Voltage Cutoff for Extended Battery Lifespan,” EV Lithium [Online]. Available: https://www.evlithium.com/Blog/lifepo4-low-voltage-cutoff-battery-lifespan.html. [Accessed: 23-Jul-2024].
[70] Kong, L., and Pecht, M., 2020, “A Look Inside Your Battery: Watching the Dendrites Grow,” Battery Power [Online]. Available: https://www.batterypoweronline.com/news/a-look-inside-your-battery-watching-the-dendrites-grow/. [Accessed: 23-Jul-2024].
[71] 2024, “Freight Train Length,” Association of American Railroads [Online]. Available: https://www.aar.org/wp-content/uploads/2023/03/AAR-Train-Length-Fact-Sheet.pdf. [Accessed: 23-Jul-2024].

ACKNOWLEDGEMENTS

The authors wish to thank and acknowledge the US Department of Transportation, University Transportation Center Program (RailTEAM UTC) for funding support for this research.

ABOUT THE AUTHORS

Mehdi Ahmadian, J. Bernard Jones Chair and Director

Dr. Mehdi Ahmadian is a Dan Pletta Professor of Mechanical Engineering at Virginia Tech, where he also holds the position of Director of Center for Vehicle Systems and Safety (CVeSS), and the Railway Technologies Laboratory (RLT). Dr. Ahmadian has authored more than 130 archival journal publications and more than 250 conference publications, including a number of keynote lectures. He has served as Editor or Editor-in-Chief for four journals on Vehicle System Dynamics, Vibration and Control, Shock and Vibration and Automobile Engineering. Dr. Ahmadian is Fellow of American Society of Mechanical Engineers of the American Institute for Aeronautics and Astronautics (AIAA). He has received many distinguished scholar awards.

James M. Kasch

James M. Kasch was a graduate research assistant when he worked on this project. He is from Harrisonburg, Virginia. He graduated from Virginia Tech in the Spring of 2023 with a Bachelor's degree in Mechanical Engineering and is now working towards his Master's degree in Mechanical Engineering. In his free time, he enjoys mountain biking and fishing.